Production of amorphous silicon thin films using Chemical Vapour Deposition

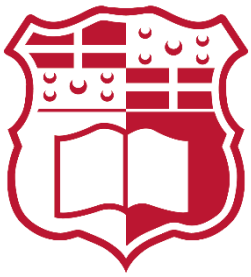

A dissertation presented at the

Institute for Sustainable Energy of the University of Malta, Malta

In partial fulfilment of the requirements for the degree of

Bachelor of Chemical Engineering

At the

Universidad de Valladolid, Spain

Under the Erasmus Student Exchange Programme 2017/2018

Lidia Amo Iglesias

June 2018

DECLARATION BY UNDERGRADUATED STUDENTS

FACULTY/INSTITUTE/CENTRE/SCHOOL Institute for Sustainable Energy of the University of Malta

Student's I.D. /Code 12419302-S

Student's Name & Surname Lidia Amo Iglesias

Course Fourth

Title of Long Essay/Dissertation Production of amorphous silicon thin films using Chemical Vapour Deposition

Word Count 18938

(a) Authenticity of Long Essay/Dissertation

I hereby declare that I am the legitimate author of this Long Essay/Dissertation and that it is my original work.

No portion of this work has been submitted in support of an application for another degree or qualification of this or any other university or institution of higher education.

I hold the University of Malta harmless against any third-party claims with regard to copyright violation, breach of confidentiality, defamation and any other third-party right infringement.

(b) Research Code of Practice and Ethics Review Procedures

I declare that I have abided by the University's Research Ethics Review Procedures.

Signature of Student

LIDIA AMO IGLESIAS
Name of Student

2/07/2018
Date

COPYRIGHT NOTICE

1) Copyright in text of this dissertation rests with the Author. Copies (by any process) either in full, or of extracts may be made only in accordance with regulations held by the Library of the University of Malta. Details may be obtained from the Librarian. This page must form part of any such copies made. Further copies (by any process) made in accordance with such instructions may not be made without the permission (in writing) of the Author.

2) Ownership of the right over any original intellectual property which may be contained in or derived from this dissertation is vested in the University of Malta and may not be made available for use by third parties without the written permission of the University, which will prescribe the terms and conditions of any such agreement.

ABSTRACT

The demand for renewable energy is ever increasing, mostly due to the fact that sources of energy used traditionally in everyday life such as fossil fuels are limited. Some of the most important and implemented renewable energy solutions include hydroelectric, wind, geothermal and solar technologies. Each technology has its limitations and most often the biggest bottle neck in renewable energy solutions is the relatively low efficiency achieved. Efforts to increase the efficiency are crucial in order to make alternative energy technologies more competitive in the future and this is especially so in solar photovoltaics. This project is focused on the development of solar photovoltaic materials, more specifically on thin film solar cells which are considered to be second generation solar cells.

Different film coatings have been made over fifteen samples using the Plasma Enhanced Chemical Vapor Deposition (13.56 MHz PECVD) technique. The coatings produced were hydrogenated amorphous silicon thin films which were deposited over two kinds of substrate, boro-silicate glass and double-sided polished silicon wafers. The films were grown from a gas mixture of silane (SiH_4) gas and hydrogen (H_2). The content of hydrogen is a critical factor in hydrogenated amorphous silicon films due to the necessity to control the Staebler Wronski effect, which implies the reduction of the photoconductivity and the dark conductivity due to prolonged illumination.

Besides the deposition campaign, the effect of deposition temperature and time over the film thickness and the content of bonding configurations of hydrogen in the film has been investigated using Ellipsometry, Atomic Force Microscopy and Fourier Transformed Infrared Spectroscopy.

It was concluded that the thin films produced at higher temperatures have a larger concentration of bonded hydrogen, but this does not affect the topographical structure. It has also been proved that the thickness of the film increases with the deposition time and temperature.

ACKNOWLEDGMENTS

First of all, I would like to thank the Erasmus Student Exchange Programme, Prof. Francisco Javier Rey Martinez from the University of Valladolid and Eur. Ing. Charles Yousif from the University of Malta, for giving me the opportunity of doing my final bachelor project in the University of Malta.

I would like to thank Dr. Ing. Maurizio Fenech for the help provided while learning how to use the different machines, the guidance and all the help provided.

Special gratitude goes also to the team at the Institute of Sustainable Energy in Marsaxlokk for the support given and for giving me the opportunity of doing this project.

Index

DECLARATION BY UNDERGRADUATED STUDENTS i
COPYRIGHT NOTICE ii
ABSTRACT iii
ACKNOWLEDGMENTS iv
Index v
List of Figures vii
List of Tables ix
Abbreviations x
Nomenclature xii

CHAPTER 1. OVERVIEW 1
1. Introduction 1

CHAPTER 2. LITERATURE REVIEW 3
1. Photoelectron generation and Photoelectron excitation 3
1.2 2 Electron diffusivity and lifetime 5
2. P-N junction 8
2.1. The current state of the art 11
2.1.1 Crystalline and polycrystalline solar cells 12
2.1.2 2.Thin films 14
2.1.3 The emerging PV 15
2.1.4 Tandem/Multijunction cells 21
3. Thin films technology for silicon 23
2.1 Hydrogenation 24
2.2 Microcrystalline Si 26
3.3 Staebler-Wronski effect 29
3.4 Applications of thin films 32
4 Potential application in the future 33

CHAPTER 2. EQUIPMENT 35
1. PECVD (Plasma Enhanced Chemical Vapor Deposition) 35
2. Spectrometric Ellipsometry 42

3. FTIR (Fourier Transformed Infrared Spectroscopy) 46
4. Contact angle 50
5. Atomic Force Microscopy (AFM) 51

CHAPTER 3. EXPERIMENTAL PROCEDURE 53
1. Cleaning procedure 53
2. PECVD (Plasma Enhanced Chemical Vapor Deposition) 54
3. Spectrometric Ellipsometry 58
4. FTIR 60
5. Contact angle 61

CHAPTER 4. RESULTS AND DISCUSSION 63
1. Measurement of the film thickness and the band gap 63
2. Measurement of the hydrogen concentration 73

CHAPTER 5. CONCLUSIONS AND FURTHER WORK 80

References 82

Appendix A 86

List of Figures

Figure 1. Energy diagram of a semiconductor. [3] 4
Figure 2. The (a) Indirect and (b) Direct band gap 5
Figure 3. Carrier recombination mechanisms in semiconductors (a) Trap-assisted recombination (b) Band to Band recombination (c) Auger recombination. [8] 7
Figure 4. N-Type and P-Type 9
Figure 5. The abrupt P-N junction under equilibrium bias. [10] 9
Figure 6. Representation of the photogeneration of charge carriers. [11] 10
Figure 7. Parts and functioning of a solar cell 11
Figure 8. Czochralski method [13] 12
Figure 9. (a) Monocrystalline silicon wafer (b) Polycrystalline silicon wafer. [14] 14
Figure 10. (a) Thin film solar cell (b) Structure of a thin film solar cell 15
Figure 11. Band diagram of the hot carrier cell. [17] 16
Figure 12. Perovskite solar cell. [19] 18
Figure 13. Comparison of cost and efficiency of the generations of solar cells. [17] 19
Figure 14. Efficiencies of the different kinds of solar cells 20
Figure 15. (a) Structure of a tandem solar cell (b) Graph of Spectral irradiance vs Wavelength over air mass 1.5 solar spectrum. [23] 21
Figure 16. Two-dimensional schematic representation of the structure of (a) Silicon crystal (b) Amorphous silicon (c) Hydrogenated amorphous silicon. [28] 25
Figure 17. (a) dependability of silane concentration in plasma from (b) Dependence on SH. [32] 27
Figure 18. (a) Microcrystalline solar cell structure. [34] 29
Figure 19. Example of the Staebler-Wronski effect – Reduction of sheet conductivity following light soaking. 30
Figure 20. Metastable defects in amorphous silicon 31
Figure 21. Structure of a HIT solar cell 34
Figure 22. Gas handling system in the ISE. 36
Figure 23. Plasma set up. [44] 37
Figure 24. Graph of deposition rate vs (a) Total pressure (Pa) (b) RF-Frequency (MHz) (c) Plasma Power (W). [45] 39
Figure 25. Surface-diffusion model for the surface-growth process of a-Si:H. [51] 41
Figure 26. Variation of the state of polarization with a phase difference (δx −δy and δy −δx). [52] 44
Figure 27. The measurement principle of ellipsometry 45
Figure 28. Set up of the ellipsometry 46
Figure 29. Vibrational molecular modes. [56] 48
Figure 30. Interferometer diagram. [57] 49
Figure 31. Different cases of contact angle 51
Figure 32 Sketch of the operational principle of AFM. [62] 52
Figure 33. Set up of the PECVD 55
Figure 34. Samples coated over boro-silicate glass. In the first line are samples 1 (a), 2 (b), 4 (c) and in the second 5 (d), 7 (e), 8 (f). 58
Figure 35. Set up of the Ellipsometry 59
Figure 36. Set up of the AFM 60

Figure 37. FTIR set up 61
Figure 38. Contact angle set up 62
Figure 39. Effect of time over the film thickness in the samples coated over silicon.... 64
Figure 40. Band Gap vs Time of the samples coated over silicon substrate. 66
Figure 41. Effect of temperature over the band gap of the samples coated over silicon 67
Figure 42. Broadening parameter vs time of the samples coated over silicon. 67
Figure 43. Index refraction vs Wavelength of sample 1. a-Si:H 68
Figure 44. Index refraction vs Wavelength of sample 2. a-Si:H 68
Figure 45. 3D image of the surface roughness sample 1. a-Si:H (T=100ºC and t=10 min) 69
Figure 46. 3D image of the surface roughness sample 2. a-Si:H (T=100ºC and t=15 min) 69
Figure 47. 3D image of the surface roughness sample 3. a-Si:H (T=150ºC and t=10 min) 70
Figure 48. 3D image of the surface roughness sample 4. a-Si:H (T=150ºC and t=15 min) 70
Figure 49. 3D image of the surface roughness sample 5. a-Si:H (T=100ºC and t=5 min) 71
Figure 50. 3D image of the surface roughness sample 6. a-Si:H (T=150ºC and t=5 min) 71
Figure 51. Microstructure of the amorphous silicon samples coated over silicon at 100ºC (a) 10 mins (b) 15 mins..... 72
Figure 52. Microstructure of the amorphous silicon samples coated over silicon at 150ºC (a) 10 mins (b) 15 mins..... 72
Figure 53. Microstructure of the amorphous silicon coated over silicon of sample 4. a-Si:H..... 73
Figure 54. Wavelength vs Transmission 74
Figure 55. Infrared absorption spectra of a-Si:H films deposited at 100 and 150 ºC and 10 minutes in the wagging–rocking mode region. 75
Figure 56. Infrared absorption spectra of a-Si:H films deposited at 100 and 150 ºC in the wagging–rocking mode region at 15 mins..... 76
Figure 57. Infrared absorption spectra of a-Si:H films deposited at 100 and 150 ºC in the wagging–rocking mode region at 5 mins..... 76
Figure 58. Contact angle for the samples made a 100 ºC (a) 1. a-Si:H (b) 2. a-Si:H (c) 3. a-Si:H (d) 4. a-Si:H..... 78
Figure 59. Contact angle of the double polished silicon 79

List of Tables

Table 1. Minority carrier lifetime for different material [5] 6
Table 2. Chemical reactions carried out inside the plasma. [44] 40
Table 3. Operational conditions of the different samples..... 58
Table 4. Results obtained from the ellipsometry measurement (Film thickness and band gap) 63
Table 5. Contact angles measured for different samples..... 77

Abbreviations

a-Si	Amorphous Silicon
a-Si:H	Hydrogenated amorphous silicon
AC	Alternating current
CVD	Chemical Vapor Deposition
DC	Direct current
Ec	Conductive energy band
EMA	Effective Medium Approximation
Ev	Valence energy band
F	Force on the cantilever
FTIR	Fourier Transformed Infrared Spectroscopy
G	Illumination density
HIT	Silicon Heterojunction solar cell
HOMO	Highest occupied molecular orbit
HWCVD	Hot Wire Chemical Vapor Deposition
ISE	Institute of Sustainable Energy
k	Spring constant
k_{ne}	Dissociation frequency
LUMO	Lowest unoccupied molecular orbit
LPE	Liquid Phase Epitaxy
n	Refraction index
Nd	Defect density
PECVD	Plasma Enhanced Chemical Vapor Deposition
PV	Photovoltaics
SAM	Semilab's Spectrometric Ellipsometry Analyzer
SC	Solar Cell
sccm	Standard cubic centimeters per minute

SH or $SiH_4:H_2$	Silane to hydrogen ratio
SHR	Shockley-Read-Hall
TCO	Transparent Conductive Oxide
VHF-PECVD	Very High Frequency Plasma Enhanced Chemical Vapor Deposition
p0	Equilibrium density of the majority carriers
x	Deflection of the cantilever
Δ	Phase difference
Ψ	Amplitude ratio
δn	Minority carrier density excess
µc-Si:H	Microcrystalline silicon

Nomenclature

a	Pumping speed (s)
c	Silane concentration (%)
c_p	Silane concentration in the plasma (%)
D	Silane depletion fraction (%)
d	layer thickness (cm)
de	Distance between electrodes (mm)
Eg	Band gap (eV)
P	Pressure (mbar)
$P_ρ$	Power density (W/cm^2)
R	Empirically determined interference multiple reflection loss
RF	Frequency discharge (MHz)
t	Time (mins)
To	Theorical transmission of the silane substrate (cm^{-1})
T_D	Deposition temperature (ºC)
T_R	Chamber temperature (ºC)
T_{film}	Transmission of the film (cm^{-1})
A	Absorption coefficient (cm^{-1})

CHAPTER 1. OVERVIEW

1. Introduction

The sources of energy most used nowadays are produced by fossil resources resulting in a complex atmospheric disruption that is causing a net global warming. The use of fossil fuels generates gases such as CO_2, SO_X or NO_X, which besides polluting the atmosphere also pollute the environment in the form of particulate matter and acid rain. This phenomenon exuberates the urgent need for sustainable energy. Solar cells are considered as a possible solution against the global warming or climate change since solar cells do not produce CO_2 or any other kind or greenhouse gases during operation, thus solar cells can possibly be the main energy source of the future.

In the last past few years, the production of solar cells has grown dramatically, mostly due to the favorable economic conditions. The most used and sold in the market nowadays are the crystalline silicon solar cells, this kind of SC corresponds to the first generation. The second-generation cells are also widely available, these are considered to be the thin films solar cells, which can have a significantly smaller thickness and can be made flexible. The material used as a substrate can be of any kind, including glass, plastic or metal; the most used thin film is amorphous silicon. When comparing first generation and second generation solar cells, thin films present some advantages over crystalline solar cells. The production costs are lower, larger areas of solar cell can be achieved through vacuum or room temperature liquid processing and there are a large variety of substrates that can be used including transparent ones [1].

More recently the need for higher efficiencies has made amorphous silicon thin films evolve into microcrystalline silicon (µc-Si:H). These coatings have better qualities and are a more stable absorber material than fully amorphous silicon. In order to obtain microcrystalline silicon, the hydrogen flow rate has to be increased considerably. This allows for a large amount of hydrogen to be incorporated during deposition.

The goal of the ISE (Institute for Sustainable Energy) is to create new photovoltaic cells and improve the efficiency of these. For that, the Institute invested in different machines

to create their own photovoltaic cells to be able to improve them by changing parameters and find the best parameters combination possible.

The aim of this project, an investigation has been conducted to determine the optimal operating parameters to produce hydrogenated amorphous silicon cells by plasma enhanced chemical vapor deposition through a set of exploratory experiments. Following this, deposition on pure crystalline silicon was conducted in order to find how the deposition time and temperature affect the amorphous silicon coatings properties, including thickness, content of hydrogen, band gap, spectral response and surface morphology.

CHAPTER 2. LITERATURE REVIEW

1. Photoelectron generation and Photoelectron excitation

The photoelectric effect consists in the emission of electrons or other free carriers when light shines on a material. Electrons emitted can be called photoelectrons. While the electron is moving an electric current is created.

Electrons are dislodged from their orbits only when photons reach or exceed a threshold frequency. Below that frequency, electrons will not be either released from atomic orbit or emitted from the material regardless of the length of time of exposure to the light or the intensity of the incoming light. If the electron absorbs the energy of the photon and the energy absorbed is lower than the work function of the material (minimum thermodynamic work needed to remove an electron), then the electron is not able to escape the material. The changes in the intensity of light does not modify the energy of the photons, they only modify the number of photons that can be dislodged from the surface of the material. So, the energy of the electrons emitted from the surface depends on the frequency of the incoming light and not on the intensity.

Electrons absorb energy from the photons when irradiated, but they follow an "all or nothing" principle. If all the energy of the photon is not absorbed, the energy is re-emitted; so, for the liberation of one electron from atomic binding all the energy must be absorbed. When the photon energy is absorbed, some of the energy is used to liberate the electron from the atom, and the rest goes to the electron's kinetic energy as a free particle [2].

The term "band gap" (Eg) refers to the energy difference between the valence band and the conduction band. Electrons can jump from one band to another. But, in order for the electrons to jump from the valence band to the conduction band, energy is required. The required energy is different for different materials. Electrons can gain the energy to jump to the conduction band by absorbing a photon. The term lowest unoccupied molecular orbit (LUMO) corresponds to the conduction band, and the highest occupied

molecular orbit (HOMO) corresponds to the valence band. This band is close to the Fermi level which is the highest level occupied at 0ºK temperature [3].

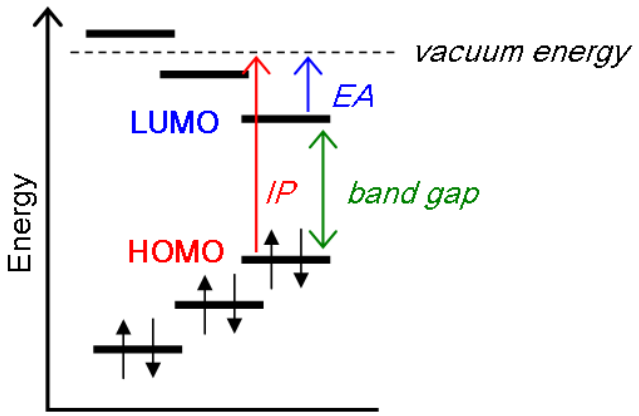

Figure 1. Energy diagram of a semiconductor. [3]

When materials have a large exciton binding energy (energy required to take apart an atom into free electrons), it is possible for a photon to have enough energy to create an exciton, but not enough energy to separate the electron and hole. Under this situation, there is a distinction between "electrical band gap" (or "transport gap") and "optical bandgap". The optical bandgap is the threshold for photons to be absorbed, while the electrical gap is the threshold for creating an electron-hole pair that is not bound together. The optical bandgap is thus always at a lower energy than the electrical band gap.

The band gap of a semiconductor can be of two types, an indirect band gap or a direct band gap. The maximal-energy state in the valence band and the minimal-energy state in the conduction band are characterized by a certain crystal momentum (k-vector). If the crystal momentums are different, the material is termed to have an "indirect band gap". If they are the same, it is called a "direct band gap", so if the crystal momentum of electrons and holes is the same in both (in the valence band and the conduction band); an electron can emit a photon. In the "indirect band gap", the electron has to pass through an intermediate state and transfer momentum to the crystal lattice, so the electron cannot be emitted [4].

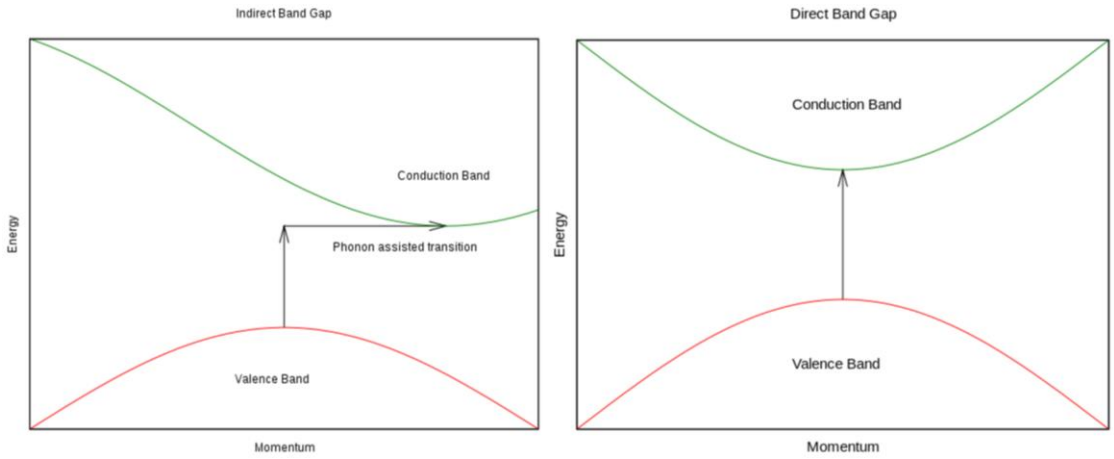

(a) (b)

Figure 2. The (a) Indirect and (b) Direct band gap

Three things can happen when a photon hits a semiconductor like silicon:

- The photon can be reflected from the surface
- The photon can pass through the silicon (when the photon energy is low)
- If the photon energy is higher than the silicon band gap value, the photon is absorbed by the silicon. This will generate an electron-hole pair.

When a photon is absorbed by the silicon, its energy is given to an electron from the crystal lattice. Normally this electron is in the valence band. The energy given by the photon to the electron "excites" it into the conduction band where it is free to move around. The network of covalent bonds where the electron used to be, now has one fewer electron (hole). The presence of a missing covalent bond allows the bonded electrons of neighboring atoms to move into that "hole", leaving one more hole behind, propagating holes throughout the lattice.

1.22 Electron diffusivity and lifetime

Diffusion current is caused by the diffusion of charge carriers (electrons or/and holes), the phenomenon is caused due to the non-uniform concentration of charged particles in a semiconductor material, they move from the region of higher concentration of electrons to the region of lower electrons concentration.

For electron diffusion to occur three things are needed:

- A gradient of particles (electrons and holes) inside the medium
- A medium (silicon)
- Collisions between particles in random directions (overall, particle movement)

The carrier lifetime is defined as the average time it takes an excess minority carrier (the less abundant charge carrier either if it is an electron or a hole) to recombine with one of its counterparts [5]. So, stating that a silicon wafer has a ''long'' lifetime, means that the minority carriers generated in the silicon wafer by sunlight will persist a long time before they recombine. Solar cells made of wafers with long minority carrier life usually have higher efficiencies. In Table 1 the carrier life time for different materials is shown.

Material	Carrier life time (s)
Si	$10x10^{-6}$
Ge	$10x10^{-7}$
GaAs	$10x10^{-10}$
ZnSe	$10x10^{-10}$

Table 1. Minority carrier lifetime for different material [5]

The carrier lifetime is extremely sensitive to small impurities or intrinsic defects. Besides the defect properties, the minority carrier lifetime is dependent on the injection level (injection level can be defined as $\delta n/p0$ where δn is the minority carrier density excess at non-equilibrium and $p0$ is the equilibrium density of the majority carriers) and the doping concentration [6].

There are three recombination mechanisms [7]:

- Band to Band recombination:

  Band-to-band recombination occurs when one electron moves from the conduction band into the empty valence band associated with the hole. This

recombination is typically referred to also as radiative recombination and is relatively unimportant in silicon, because its radiative lifetime is extremely high.

- Auger recombination:

  Auger recombination is a process in which a hole and an electron recombine in a band-to-band transition, and resulting energy is given to another hole or electron. As a third particle is evolved in this recombination, it must be treated as a different recombination that band to band.

- Trap-assisted recombination:

  Trap-assisted recombination happens when an electron falls into a "trap" (Et), this is an energy level within the bandgap caused by the presence of a structural defect or a foreign atom, such as the dangling bond in the amorphous silicon. When the trap is filled it cannot accept another electron. So, the electron occupying the trap, moves into an empty valence band state, completing the recombination process. This process can be seen as a two-step transition of an electron from the conduction band to the valence band. This recombination can also be referred as Shockley-Read-Hall (SRH) recombination.

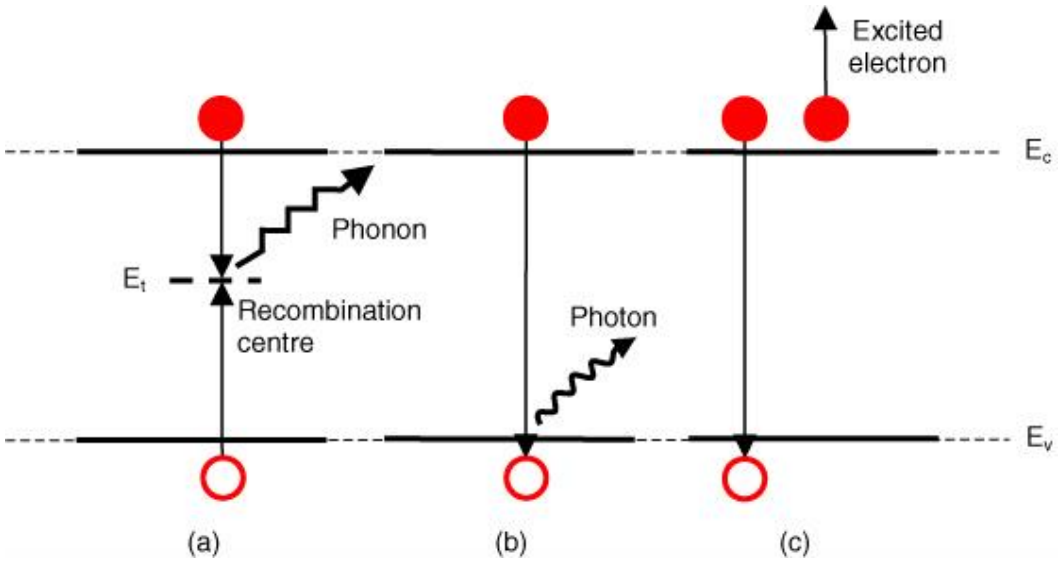

Figure 3. Carrier recombination mechanisms in semiconductors (a) Trap-assisted recombination (b) Band to Band recombination (c) Auger recombination. [8]

The conductive (Ec) and the valence (Ev) energy band are the bands close to the Fermi level. The conductive band is located above the Fermi level and is the lowest range of vacant electrons sites. The valence band is below the Fermi level and is the highest range of electrons energy in which the electrons are present at absolute zero temperature [9].

Therefore, at high carrier densities, the recombination lifetime in silicon is controlled by Auger recombination and at low carrier densities by SRH recombination. So, for silicon, the dominant recombination is the SRH.

In silicon solar cells the lifetime can be as high as one millisecond, but in a direct semiconductor as GaAs, where the auger recombination is dominant, the lifetime is only in the range of nanoseconds or microseconds.

2. P-N junction

In the field of photovoltaics, the P-N junction is a semiconductor device with a large surface area that converts the photons originating from the sunlight into available power, using the electronic properties of the semiconductor material. Solar cells depend on the phenomenon known as 'photovoltaic effect' (creation of an electric current and voltage in a material when is exposed to light) for their operation.

Solar cells usually are made of silicon which is a semiconductor material, the silicon in solar cells can be found as monocrystalline, polycrystalline form and has an indirect energy bandgap of 1.1 eV, as amorphous silicon with an energy bandgap of 1.7eV or other variances like microcrystalline silicon. Solar cells can also be produced by using III–V compounds such as gallium arsenide (GaAs) and indium phosphide (InP). These materials have direct energy bandgaps of 1.4 eV.

Crystalline silicon atoms are arranged together in a particular structure. Within the cell there are two different layers; the N-type, which has spare electrons, and the P-type, which is missing electrons, leaving 'holes' in their place from the acceptor impurities, this structure is called P-N junction. In figure 4 a N-type and a P-type silicon material is shown.

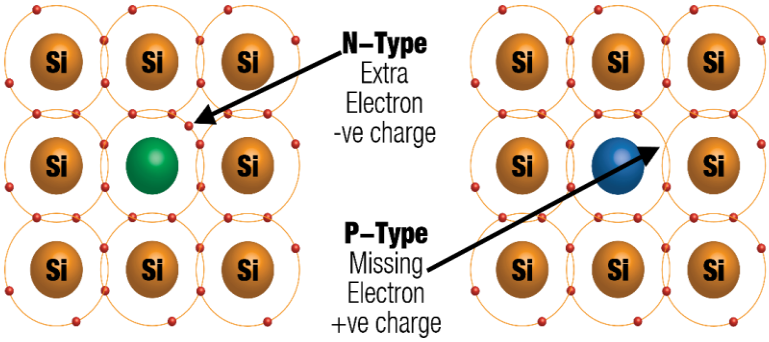

Figure 4. N-Type and P-Type

When a piece of P-type silicon is placed in contact with a piece of N-type silicon, a diffusion of electrons start to flow from the region of high electron concentration (the N-type side of the P-N junction) into the region of low electron concentration (P-type side of the P-N junction).

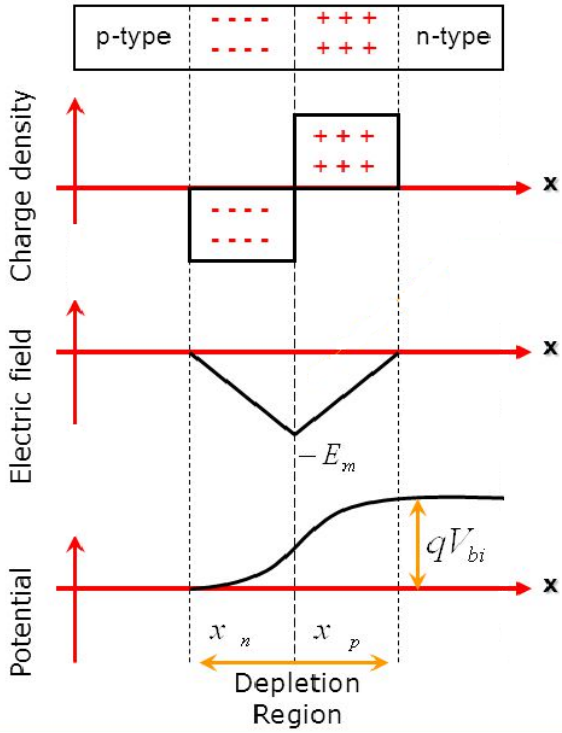

Figure 5. The abrupt P-N junction under equilibrium bias. [10]

When the electrons diffuse through the P-N junction, they recombine with holes on the P-type side of the silicon. However (in the absence of an external circuit) this diffusion of carriers does not go on indefinitely because charges build up on both sides of the junction and create an electric field. This electric field promotes charge flow, known

as drift current, which opposes the movement and eventually balances out the diffusion of electrons and holes. The region where electrons and holes have diffused across the junction is called the depletion region because it contains practically no mobile charge carriers. In Figure 5 it can be seen that the charge density in the depletion zone is constant in each region. The total potential must equal to the difference between the built-in potential and the applied voltage [7].

Ultimately, a solar cell is an electrical device that converts sunlight into electricity. So basically, is a P-N junction where the photons resulting from the sunlight strikes the surface of the cell creating an excess of carriers produced by the photoelectric, these excess of carriers are pushed by the electric field towards the N-type side of the cell. This can be seen in Figure 6. The cells have electric connections arranged in series and parallel to set the exit voltage.

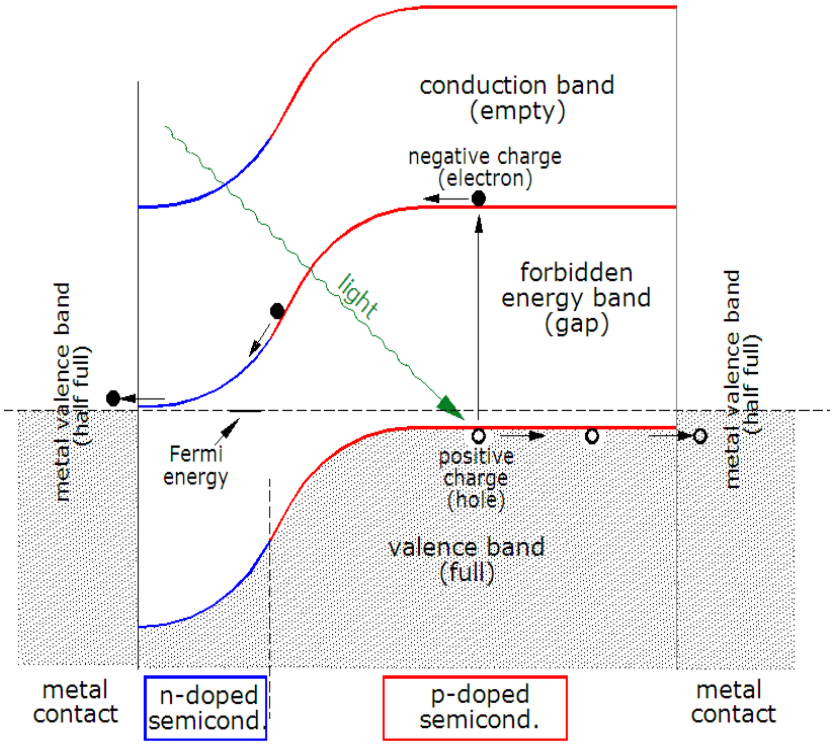

Figure 6. Representation of the photogeneration of charge carriers. [11]

The N-type material is usually thinner, in order to allow light to pass through to the P-N junction. P-N junctions of silicon solar cells are made by diffusing an N-type dopant into one side of a P-type wafer (or vice versa).

Solar cells are normally stacked together to form a solar panel, which in turn is made of different parts [12]:

- External cover facing the sun: made of glass, it's function is to facilitate the maximum transmission of sun radiation. It should be highly resistant and with a low content of iron.
- Capsule layer: closes the radiation so it does not lose its intensity.
- Photovoltaic cell: this is the electrical device that converts the energy of sunlight into electricity. The electrical contacts (the larger silver colored strips) in the solar cell are made of busbars and are placed at both sides of the solar cell, the glue used must be thermally conductive, because the cells get heated while absorbing the sun energy. The fingers (the small lines which are perpendicular to the electric contact) are painted on the silicon.
- The base: usually made of aluminum, over this layer, the photovoltaic cells are placed.
- Wiring.

Figure 7 shows the parts of a functioning solar cell.

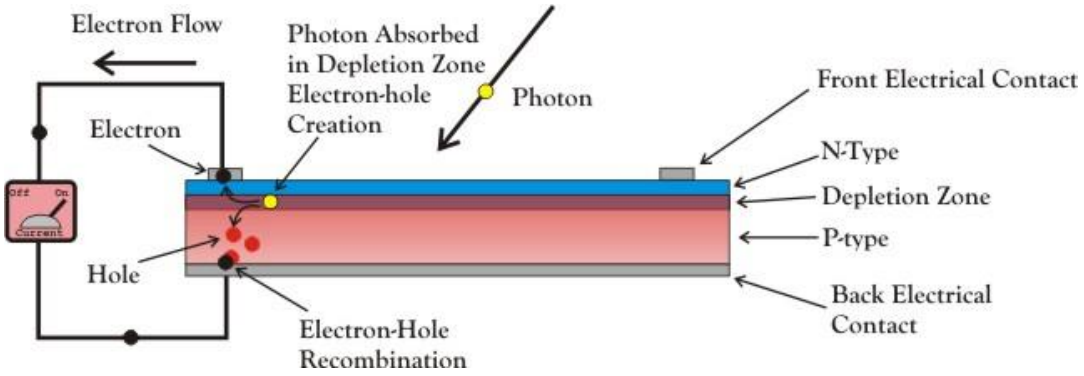

Figure 7. Parts and functioning of a solar cell

2.1. The current state of the art

Nowadays there are 3 different generations of solar cells:

2.1.1 Crystalline and polycrystalline solar cells

These kind of solar cells are known as the first generation and are the most common types.

- Crystalline or monocrystalline silicon:

The monocrystalline wafers of silicon are cut from a large single crystal or boule. The monocrystals are normally grown using the Czochralski method which is an industry accepted method used to produce a uniform and cylindrical crystal with a specific crystal orientation. As described in Figure 8, the process involves melting of the silicon in a crucible usually made of quartz at the temperature of 1425 ºC. Then a seed of crystal in a rod is dipped into the molten silicon. The rod is slowly rotated and pulled upwards simultaneously. By controlling the temperature gradients, the rate of speed and pulling of rotation, it is possible to extract a large, single-crystal, cylindrical ingot from the melt. The process is usually carried out in inert atmospheres, such as argon. Once the ingot is obtained it is cut in layers [13], [14].

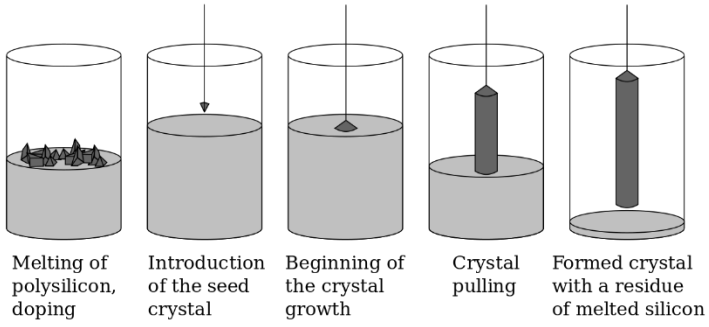

Figure 8. Czochralski method [13]

The wafer is then doped p-type using boron in the form of either gas precursors or molten salts. The wafers are subsequently mechanically polished to remove damage from the cutting tool process and then chemically polished to remove damage from the mechanical polishing process [15].

A P-N junction is created in the wafers by diffusing phosphorus into the surface of the wafer to convert the surface to an N-type region. Electrical contact is made to the N-

type diffused region via a grid contact that allows light to pass through it to reach the depletion region of the P-N junction. The wafer is stacked to a substrate, which can be a rigid panel or a soft blanket.

Commercially available modules made using crystalline silicon typically have solar conversion efficiencies upwards of 20%, the most sophisticated cell designs having efficiencies up to 25% [15].

Monocrystalline solar cells are the most space-efficient. Another advantage of monocrystalline cells is that they also have the longest usable life of all types. Many manufacturers offer warranties of up to 25 years on these types of PV systems.

On the other hand, monocrystalline solar cells have a disadvantage, since the wafers are made from cylindrical silicon ingots, the resulting solar cell is circular. In order to increase packaging efficiency within a module, the sides are cut so to make a square. This side trimming results in wastage of viable silicon and typical monocrystalline photovoltaic modules incorporate cells which are not perfectly square in a compromise between wastage loss and packaging efficiency, Figure 9 (a).

- Polycrystalline silicon:

Over 60% of module production is now based on the use of polycrystalline silicon wafers rather than those produced using the Czochralski method [15]. The silicon is poured into a container and heated until it melts at a temperature of 1425 ºC, then it is cooled resulting in silicon ingots. The silicon crystal orientation is not uniform in such a process and typically, grain growth follows the temperature gradient resulting in growth from the bottom of the container upwards.

Some advantages of using polycrystalline growth over the Czochralski method include lower capital costs, less sensitivity to the quality of the silicon feedstock used and higher packing density of cells to make a module. This is because, as said before, the monocrystalline is not a perfect square, so, in this case, they are perfectly square or rectangular. The best modules made using polycrystalline silicon generally have

efficiencies 2–3% less than those of crystalline silicon and cost approximately 80% of that of single crystal silicon cells to produce.

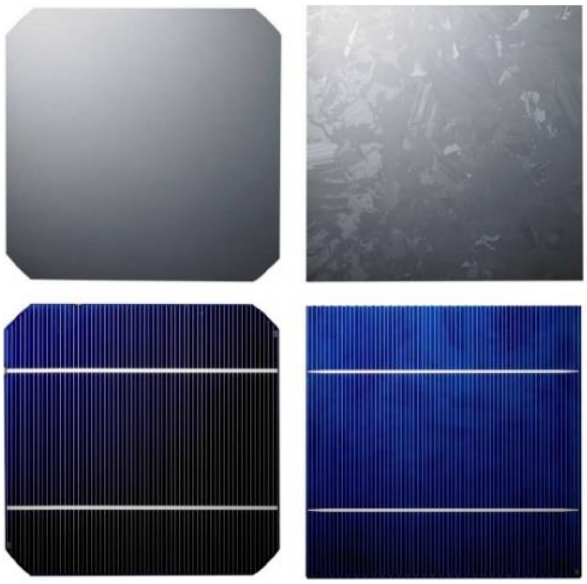

(a) (b)

Figure 9. (a) Monocrystalline silicon wafer (b) Polycrystalline silicon wafer. [14]

2.1.2 2.Thin films

Thin films are the second generation of solar cells, they are made by depositing one or more thin layers of photovoltaic material over a substrate, which could be a glass, plastic or metal, the thickness of the film could be from micrometers to nanometes. They can be made with different materials such as cadmium telluride (CdTe), copper indium gallium diselenide (CIGS), but the most common is amorphous silicon (a-Si). This is the non-crystalline form of silicon with a mobility band gap of approximately Eg = 1.7 eV at room temperature [16]. This kind of solar cells is explained in more detail in Section 4.

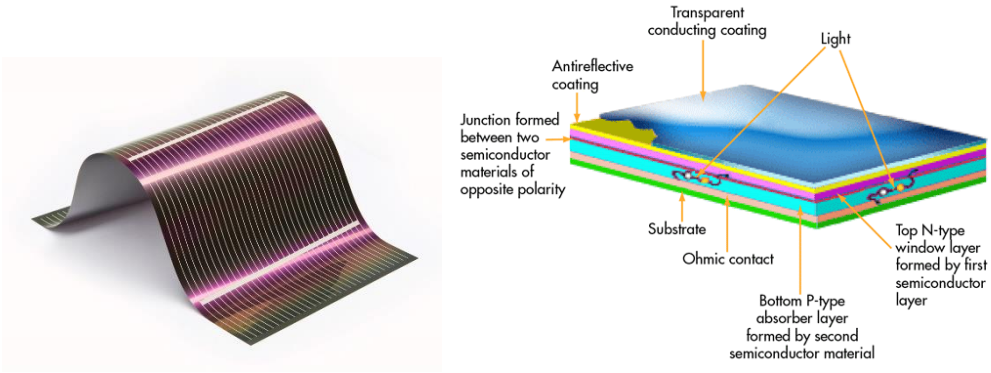

(a) (b)

Figure 10. (a) Thin film solar cell (b) Structure of a thin film solar cell

2.1.3 The emerging PV

In the past few years, new kinds of solar cells have been developed, these solar cells are denominated as the third generation. According to the number of patents filed, solar cells research stands at the second place, just behind that of fuel cells [17].

Other materials are used instead of silicon in third generation cells, and these include organic dyes, hot carriers, nanotubes, conductive plastics, silicon wires, perovskites and more. The target of this generation is to build solar cells less expensively but more efficient. Most of them are being developed in laboratories by new companies, and the majority, while promising a great return on investment, are not commercially available yet.

Some of the new solar cells are:

- Hot carrier cells:

A hot-carrier solar cell is a device that offers the possibility of very high efficiencies (the maximum efficiency is 65% for unconcentrated illumination) but with a structure that could be simpler than other very high-efficiency PV devices (like multijunction tandem cells) [17].

Electron-hole pairs generated in conventional solar cells (monocrystalline silicon) lose energy by cooling down from their initial energetic 'hot' position to the band edges by optical phonon emission. The hot carrier tries to minimize this loss by extracting carriers at elevated energies in a narrow range, requiring a substantial delay in carrier cooling in the hot carrier absorber and energy selective carrier extraction by an energy selective contact [18].

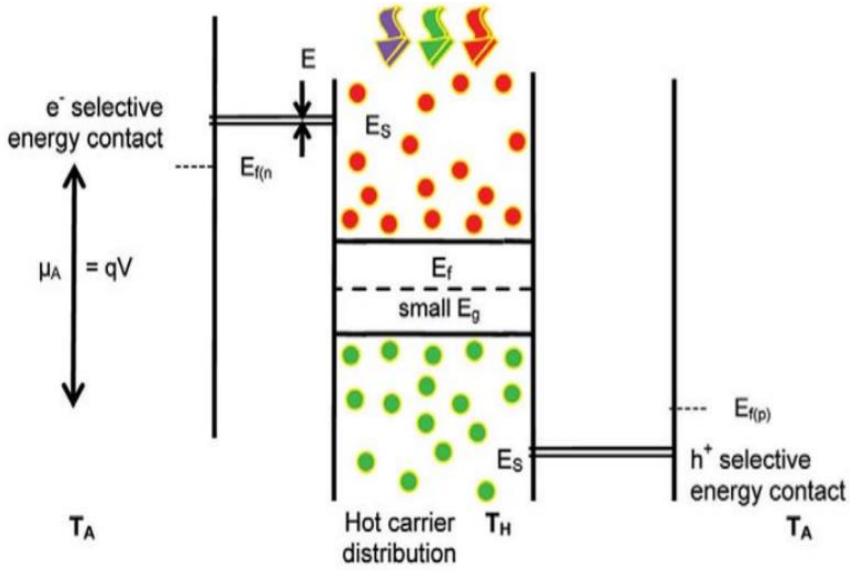

Figure 11. Band diagram of the hot carrier cell. [17]

- Organic solar cells:

The organics solar cells can be made either of conductive organic polymers or small organic molecules. These molecules are a solution of high throughput, which means that the production cost is low, but the efficiency and stability are also low compared to inorganic PV solar cells such as silicon.

With molecular engineering, it is possible to change the band gap. The optical absorption coefficient of organic molecules is usually high, which means that a large amount of light can be absorbed with a small number of material, usually on the order of hundreds of nanometers, resulting in the requirement of very little material to produce a viable cell.

- Dye-Sensitized solar cells:

The dye-sensitized solar cells are based on a semiconductor formed between an electrolyte and a photosensitized anode, this is called a photoelectrochemical system. This cell is known as the Grätzel cell [19].

These solar cells are made of a transparent conductive substrate, with a high surface area of N-type semiconductor (normally TiO_2), a dye (sensitizer: this one absorbs the light), an electrolyte containing a redox mediator and a counter electrode that it is usually bound to the surface of the N-type semiconductor [19].

- Polymer-based solar cells:

Polymer solar cells are one example of an organic solar cell, they are flexible, lightweight, large-area devices. They can be fabricated by deposition of organics by screen printing, inkjet printing, doctor blading, or spray deposition at room-temperature [20]. High power conversion efficiencies of ∼10% have already been reported in tandem polymer solar cells [21].

To improve the efficiency of the polymer solar cells toward 10%, one strategy could be to use a narrow-bandgap polymer that can deliver both a relatively high open-circuit voltage and a high current density, as the donor material [21].

- Quantum dot solar cells:

Quantum dots are narrow-gap semiconductor micro-crystal particles of a few nanometers size form in a semiconductor matrix with a wide bandgap [22]. The dots can be grown with different sizes so that they will have a variety of bandgaps without changing the material or construction techniques. Because of this property quantum dots are very attractive for multijunction solar cells.

- Perovskite solar cells:

The perovskite solar cells are the successor of the dye-sensitized solar cells and an evolution of organic and polymer solar cells. The first that perovskite was used as a solid-

state solar cell was in a dye-sensitized cell using $CsSnI_3$ as a P-type hole transport layer and absorber.

Perovskites have the general formula of ABX_3 where A and B are monovalent and divalent ions, respectively. X is either O, C, N or a halogen, they have a cubic structure. The earliest perovskite is formed with calcium, titanium, and oxygen ($CaTiO_3$). The most common perovskites used for solar cells nowadays are $CH_3NH_3PbI_3$ and $CH_3NH_3PbBr_3$ [19].

Perovskites have the ability to form crystals with a very high quality in a short time using solution processing methods and moderate temperatures (between room temperature and 150 ºC).

This kind of solar cells is believed to be a key future technology since it has shown the fastest advances in solar technology, the efficiency has increased from 3.8% in 2009 to 22.7% in late 2017 [17]. The production cost is lower than others with the same efficiency.

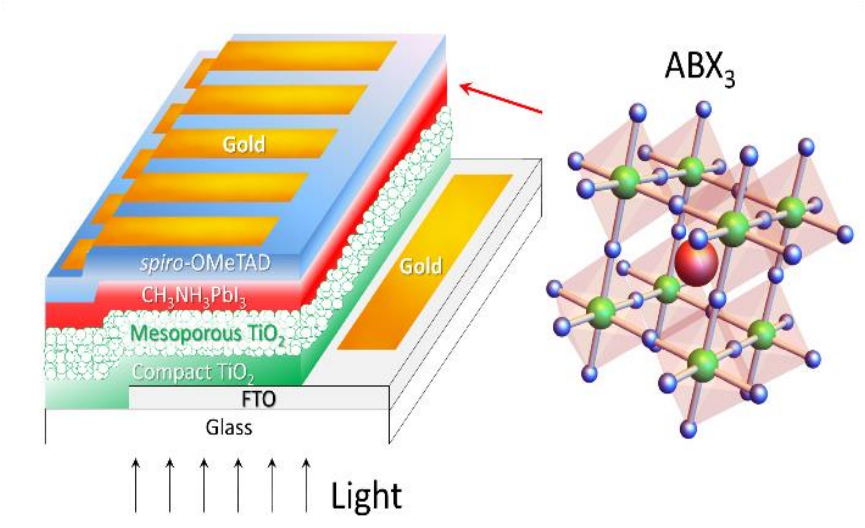

Figure 12. Perovskite solar cell. [19]

Key issues are still present in Perovskite solar cells as although they yield a very high efficiency, the long-term stability of these cells remains a problem, with water infiltration and UV degradation hindering this technology from going into the market [19].

In Figure 13 can be seen a comparison between the efficiency and the cost of the three generation of solar cells.

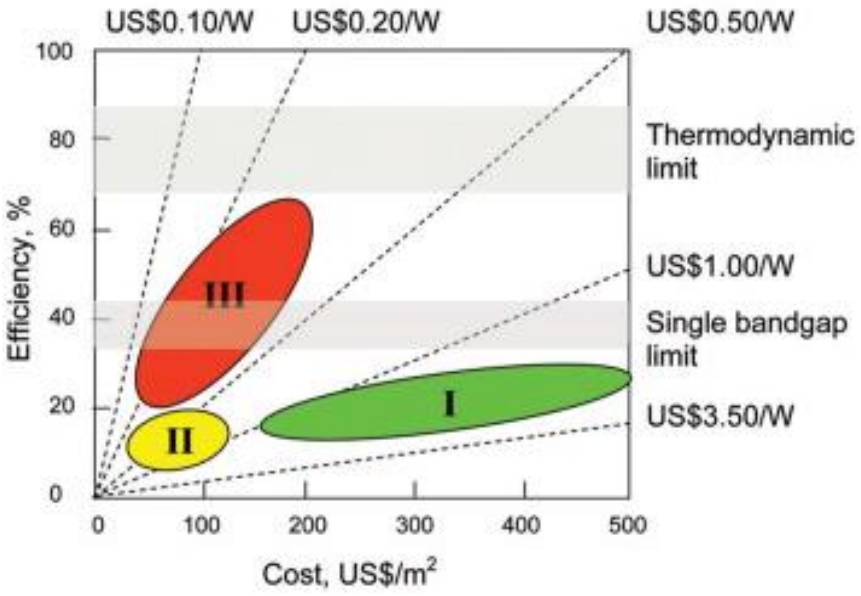

Figure 13. Comparison of cost and efficiency of the generations of solar cells. [17]

In Figure 14, it is shown the evolution of the efficiency of the different types of solar cells throughout the years. As said before, perovskite solar cells are the ones that their development has been faster (in terms of efficiency).

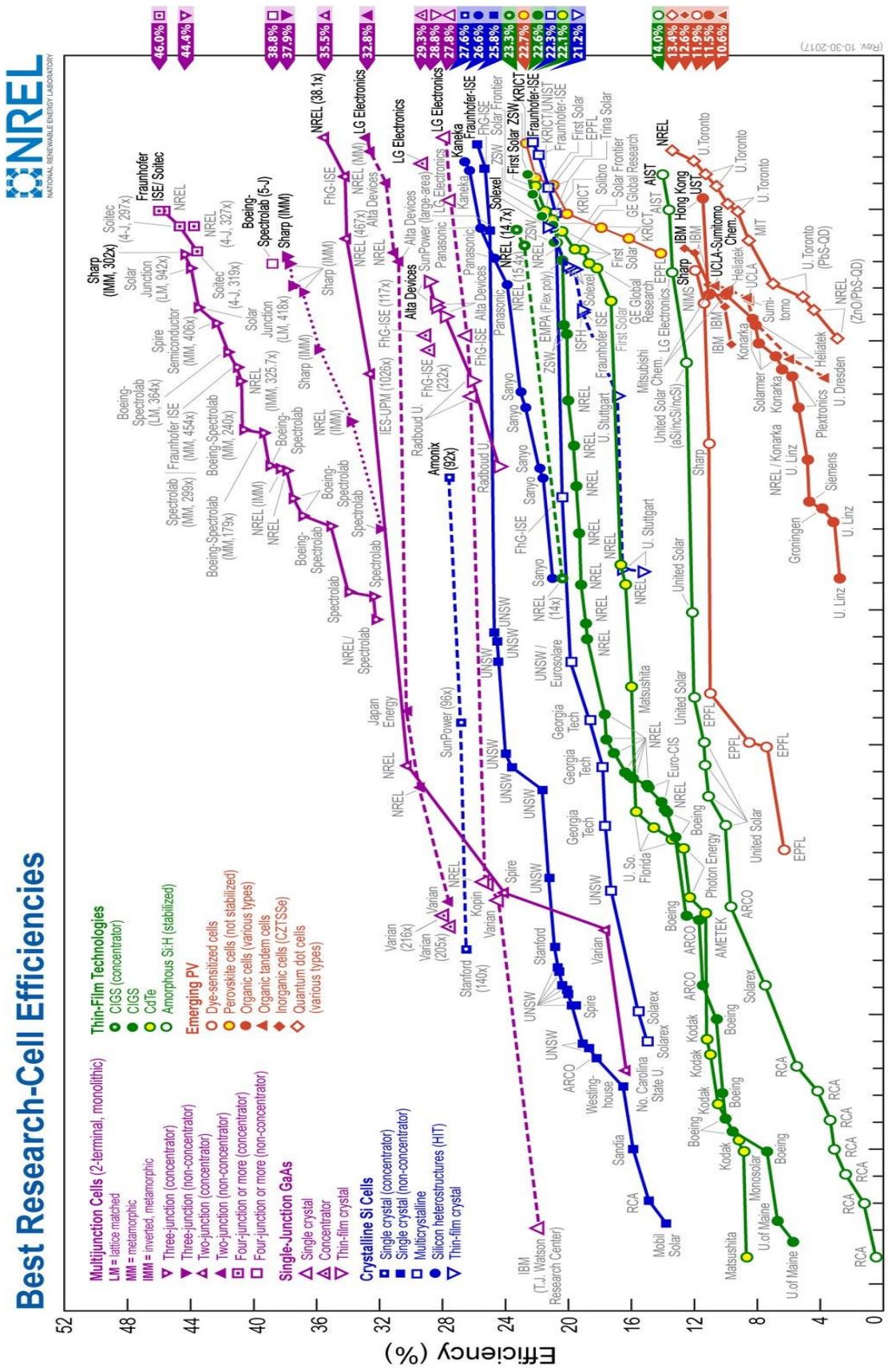

Figure 14. Efficiencies of the different kinds of solar cells

2.1.4 Tandem/Multijunction cells

The tandem or multijunction solar cells are formed by multiple P-N junctions from different semiconductors materials of increasing the bandgap, they are a mixture between crystalline and thin films solar cells. The different layers are placed on top of each other, such that the highest bandgap intercepts the sunlight first. As the number of bandgaps increases, the higher spectrally sensitive it will be. The strategy of this is to increase the number of excitable energy levels [17].

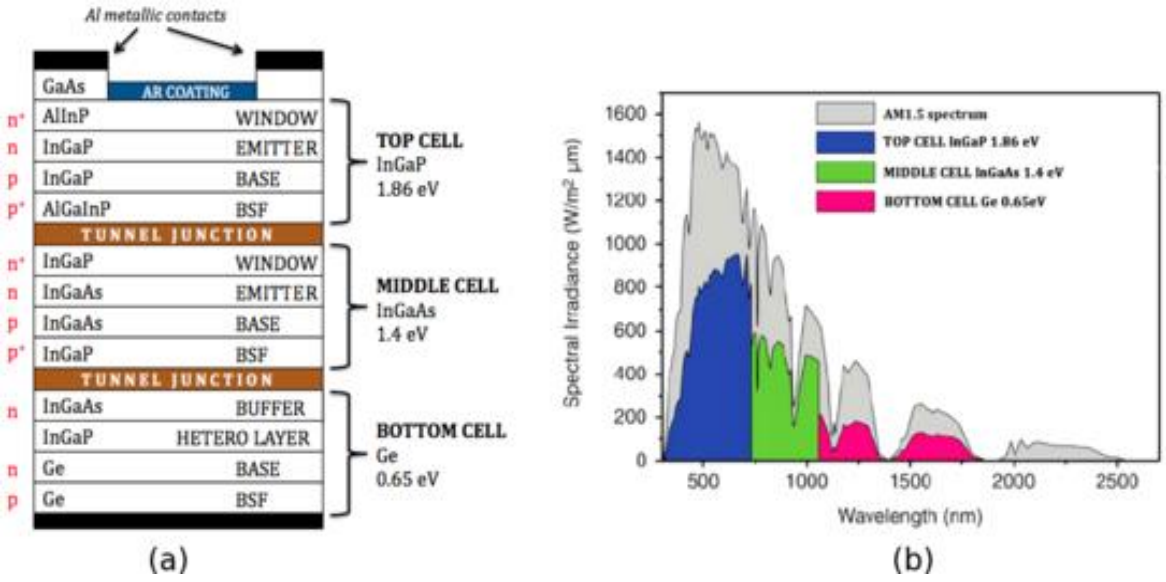

Figure 15. (a) Structure of a tandem solar cell (b) Graph of Spectral irradiance vs Wavelength over air mass 1.5 solar spectrum. [23]

Tandem Solar cells can be made using single-crystal III-V materials support structures such as Germanium. These can yield very high efficiencies, up to 46% under concentrated sunlight [17] and find use in critical applications such as satellite systems and concentrated PV systems.

The multijunction solar cells are formed by multiple P-N junctions from different semiconductors materials, each material from the P-N junction will produce an electric current in response to different wavelengths of the sunlight due to the increasing bandgaps of the different material that compound the cell. This way the solar cells capture and convert some energy that otherwise would be lost. The top cell must be as

thin as possible so that enough light is transmitted to the bottom of the cell in order to generate more current there [24].

Materials with different band gaps are essential in the processing of tandem solar cells. Compound semiconductors like II-VI or III-V have already been used in tandem solar cells. The use of III-V semiconductors offers higher efficiencies [22].

P-N junctions built using different semiconductors material are grown by epitaxial methods. A multijunction solar cell that only uses one substrate is called a monolithic multijunction solar cell. The different P-N junction is internally connected by tunnel diodes, so the total output current of a multijunction solar cell is determined by the minimum current generated in the sub-cell [22].

When the multijunction solar cell is made up of different substrate materials there is another technology used called mechanically stacked approach. The advantage of this approach is that the solar cell is simpler compared to the monolithic multijunction solar cell [22]. There are other technologies like Zn-vapor diffusion or liquid phase epitaxy (LPE) technology.

Tandem cells which include thin films of amorphous silicon that is deposited on crystalline silicon also exist. These are known as silicon heterojunction cells (HIT) and are explained in more detail in section 5.

A single-junction solar cell has a maximum theoretical efficiency of 33,16%. A multijunction solar cell with an infinite number of junctions would have an efficiency of 86,8% under highly concentrated sunlight [25]. Nowadays the best laboratory crystalline solar cells have efficiencies from 20% to 25%, while III-V multijunction solar cells have achieved efficiencies of 46% under concentrated sunlight [26]. There are some commercial ones that have efficiencies of 30% under normal sun illumination.

To date, the high price of III-V solar cells and high price-to-performance ratio have limited their use to special roles like space applications, where their high power-to-weight ratio is more attractive and offsets the risk of using rare or toxic elements such

as indium and arsenic. These reasons makes tandem solar cells not suitable for generic use.

3. Thin films technology for silicon.

Thin films can be made with different materials as it has been said before such as cadmium telluride (CdTe), copper indium gallium diselenide (CIGS); but the cadmium used is highly toxic and the indium required is rare. Because of these reasons silicon is considered to be more adequate for the production of commercial thin film Photovoltaics.

The first time amorphous-silicon (a-Si) was deposited onto a substrate using a silane glow discharge was in 1955 by Sterling [1]. In 1969, Chittick obtained the first intrinsic amorphous silicon of acceptable quality by PECVD [1]. Many others kept trying to develop the deposition of amorphous silicon over a glass substrate. All along this time, this material has been evolving into a whole family of semiconductors based on different forms of silicon made by different techniques [1].

Many different techniques have been tested to produce a-Si. In the beginning, the two most used were evaporation and sputtering, but the material had a lot of defects. Some other techniques are being used in the industry such as plasma spray, reactive chemical vapor deposition, ion-beam-assisted evaporation, electron cyclotron resonance or expanding thermal plasma deposition [9]. The preparation of amorphous silicon by PECVD (Plasma Enhanced Chemical Vapor Deposition) of silane (SiH_4) and mixtures of silane and other components allowed to obtain a higher quality. One of the components used is hydrogen which yields hydrogenated amorphous silicon (a-Si:H). These features have made PECVD the most used preparation technique for thin-film silicon.

Lately, other techniques have appeared such as very-high-frequency PECVD (VHF-PECVD) and hot-wire CVD (HWCVD), offering the possibility to make a higher-quality material (amorphous, nanocrystalline or microcrystalline).

Film thickness can vary from a few nanometers (nm) to tens of micrometers (µm). Compared to the first generation (crystalline silicon solar cells), thin films are much

thinner which allows them to be flexible and have a lower weight, these properties permit them to have applications in devices where monolithic silicon is too rigid or bulky.

Silicon is a fourfold coordinated atom, crystalline silicon is tetrahedrally bonded to four neighboring silicon atoms, which forms a well-ordered crystal lattice. Amorphous silicon does not present this structure, all the atoms form a random network. Because of the random structure, some atoms have a dangling bond (broken bonds), and this represents defects in the network and they cause anomalous electrical behavior. To reduce the number of dangling bonds hydrogen is introduced as gas precursor with the silane in the PECVD. Hydrogen molecules dissociate together with the Silane and the resulting free hydrogen is allowed to make bonds with the dangling bonds in silicon thus terminating the bond. High quality (low defect density) intrinsic layers (i-layers) are preferred over doped amorphous silicon when they act as absorber layers, because amorphous silicon doped layers carry a high defect density [16].

Unlike in crystalline silicon, the main charge transport mechanism in amorphous silicon is drift by the electrical field instead of diffusion [16].

The conversion efficiency of the thin film solar cells is very limited, at the beginning it was practically zero (1975), but with the years it has evolved, by 2009 the efficiency was of 9,5% [9] nowadays efficiency of 13.5% can be reached.

2.1 Hydrogenation

Amorphous silicon presents very high defect density, so this causes some undesirable semiconductor properties such as poor photoconductivity and prevents doping [27]. Hydrogen plays a very important role while producing amorphous silicon solar cells and when it is introduced together with the amorphous silicon it passivates a large part of the dangling bonds resulting in a lesser chance for trap assisted recombination. Photoconductivity is improved and doping is made possible.

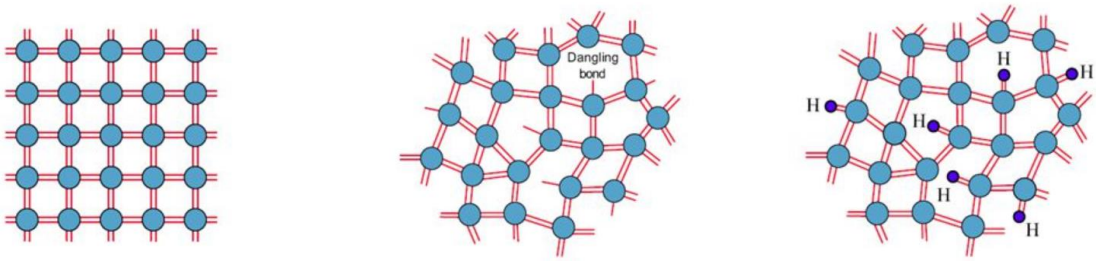

(a) (b) (c)

Figure 16. Two-dimensional schematic representation of the structure of (a) Silicon crystal (b) Amorphous silicon (c) Hydrogenated amorphous silicon. [28]

For the preparation of the layers, most of the industry and research laboratories only use silane and hydrogen as gas precursors for the deposition in the PECVD. However, other deposition regimens have been studied, like adding an inert gas such as argon or helium. Depending on the conditions of the deposition they play different roles: they can help nucleation, densify layers or create defects, etch already deposited material, or dilute the silane (which is auto-flammable in high concentrations), or enhancing the safety of the process [24].

The microstructure of the thin film silicon layer is modified by changing the hydrogen and silane ratio SH:

$$SH = \frac{SiH_4}{SiH_4 : H_2}$$

Equation 1

If SH decreases, the bandgap increases slightly and light-induced degradation decreases. For a value of SH of 5-10%, there is a transition from amorphous silicon to microcrystalline [29].

Hydrogenation might create some metastable defects. One of them is created when there is a collision between two hydrogen atoms when a charge carrier or an incoming photon heats the surface of the layer, one hydrogen atom is detached from a Si-H bond. This atom diffuses through the network. If one diffusing atoms break/open a Si-Si weak bond and form one Si-H bond, there will be left one dangling bonds in the network, which was not there before. Another one is the H-flip defect, the flip changes the

structure around the hydrogen atom, this defect does not create necessarily a dangling bond [30]. The most important defect caused by the hydrogen is the Staebler-Wronski effect which is detailed further in section 4.3.

2.2 Microcrystalline Si

Microcrystalline silicon (µc-Si:H) is a thin film semiconductor material composed of crystalline silicon and amorphous silicon phases, plus grain boundaries. Microcrystalline silicon is obtained by PECVD, same as amorphous silicon, and the best efficiencies reported have been achieved by using this technique. This is a very promising material for the application as an intrinsic absorber layer in solar cells.

The microstructure depends on the substrate roughness and the hydrogen concentration during the deposition (to obtain microcrystalline silicon a larger amount of hydrogen is needed than to obtain amorphous silicon). Eberle et al [29] had noted that the regime around 6% of silane concentration is called the "transition region" it gives the best µc-Si:H solar cells. Strahm et al [29] furthered on this and concluded that besides the concentration of silane, another factor that affects the material crystallinity is the silane depletion fraction, which depends on gas exchange flowrates, plasma power, reaction rates and the sticking probability of the radicals [27].

The silane depletion fraction can be calculated through the next equation:

$$c_p = c * (1 - D)$$

Equation 2 [27]

Where:

- Cp is the silane concentration in the plasma
- C is the silane input concentration
- D is the silane depletion fraction

The depletion fraction also depends on the dissociation frequency (k_{ne}), this one depends on radio frequency and the pumping speed (a) which depends on the pressure inside the chamber, the flow rate and the inter-electrode distance. So, the depletion fraction can also be calculated as:

$$D = \left(1 + \frac{\frac{a}{k_{ne}}}{(1+c)}\right)^{-1}$$

Equation 3 [27]

The transition zone can be separated into two different regimes:

- Regime 1: at low depletion (D < 0.5) and low input of silane (c < 2.5%), the film microstructure is governed by the silane input concentration [31]. Here the reaction rates and the ticking probability of the radicals is smaller, the layers obtained in this region have better quality [27].

- Regime 2: at high depletion (D > 0.8) and high silane input concentration (c > 5%) and, the film microstructure is governed by the high depletion fraction [31]. In this region more radicals are generated, it results in a reduction in the film density and increased structural disorder [27].

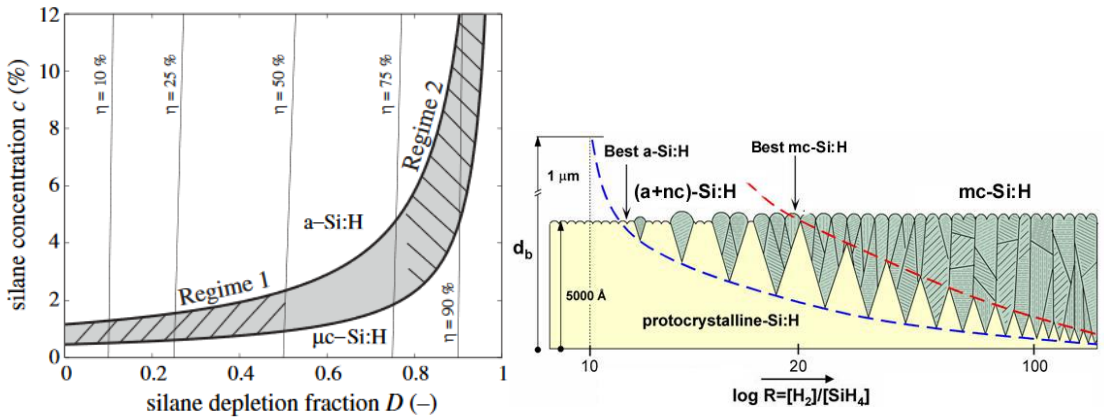

Figure 17. (a) dependability of silane concentration in plasma from (b) Dependence on SH. [32]

This means that there is not only one silane input concentration which defines the transition from amorphous silicon to microcrystalline silicon, because the effective

concentration of silane in the plasma, depends on the level of silane depletion and the input concentration.

A large amount of hydrogen incorporated while deposition, passivates most of the dangling bonds, but it still has some defects, they are the grain boundaries located between large conglomerates of nanocrystals or nanocrystals in the surface.

The solar cells with the highest efficiencies have been reported for thin films which have a medium average crystallinity, half of the volume of the cell is amorphous silicon and the other half microcrystalline [33]. Sculati et al [33] have reported that microcrystalline silicon can be also obtained both with low-frequency plasma (100-460 KHz) as well as with higher frequencies (13.56 MHz).

The first step in the layer growth is the incubation phase of the amorphous silicon, then crystalline formation starts with the nucleation centers near the film/substrate interface. In the next layer deposition, groups of crystallites grow (crystallization phase) until a saturated crystalline fraction is reached. This process depends on the deposition conditions.

The band gap in μc-Si:H is reported to have a value of 1.1 eV, it is lower than the one amorphous silicon 1.7 eV has due to the small fraction of crystalline silicon that it contains, so it absorbs light within a wider spectral range [16].

Apart from the intrinsic microcrystals, microcrystalline silicon doped layers show a distinct behavior from amorphous silicon and the electrical properties are more favorable compared to amorphous silicon doped layers. This is primarily because microcrystalline silicon can be more efficiently doped, and the activation energies of dark conductivity are smaller. When the microcrystalline layer is doped, it acts as a seed layer for the crystallites in a μc-Si:H i-layer grows on top of it, with this, the growth of the amorphous layer is prevented.

The advantage of microcrystalline silicon intrinsic layers for i-layer application in thin-film silicon solar cells is that the apparent band gap is lower compared to amorphous silicon, this makes the combination of μc-Si:H and a-Si:H in a tandem solar cell possible.

As shown in Figure 18, microcrystalline Si:H can be positioned in tandem with amorphous silicon and sandwiched between ZnO:Al transparent conductive oxide layers. Such a cell is called a "micromorph" tandem solar cell. Because of the large difference in the bandgap values (1.1 eV and 1.7 eV), a much better utilization of the solar spectrum and efficiency is achieved.

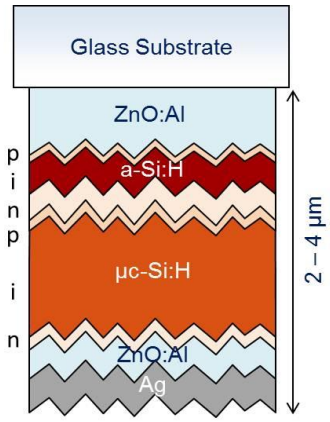

Figure 18. (a) Microcrystalline solar cell structure. [34]

The costs of producing this kind of solar cell is much lower than crystalline solar cells due to the low temperature used in the production process and because the required thickness is two orders of magnitude thinner [16].

3.3 Staebler-Wronski effect

Staebler and Wronski observed in 1977 some metastable changes in amorphous silicon [35]. They found that photoconductivity and the dark conductivity of glow-discharge deposited over amorphous silicon can be reduced by prolonged illumination with intense light, leading to a decrease in cell performance. The authors also found that these changes are reversible by annealing of the amorphous silicon samples at elevated temperatures (150ºC). The fact that reannealing of the material recovered the efficiency suggested that this loss of efficiency is due to a reversible increase in density of gap states acting as recombination centers for photoexcited carriers [35].

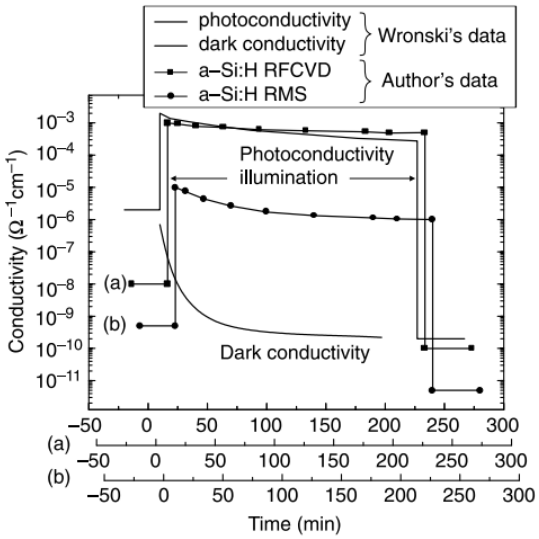

Figure 19. Example of the Staebler-Wronski effect – Reduction of sheet conductivity following light soaking.

The most favored model to describe the Staebler Wronski effect is the one described in section 3.1; the hydrogen atoms collapse when a charge carrier or an incoming photon heats the surface of the layer, these ones recombine with a weak bond of Si-Si breaking it and leaving two dangling bonds in the network, this recombination releases about 1.5 eV. Another model known as the charge transfer model says that pre-existing spineless centers (negatively and positively charged dangling bonds) are transformed into neutral dangling bonds by the capture of excess carriers [36].

Branz [35] proposed a new model for metastability, it postulates the formation of a metastable complex containing two Si-H bonds. Light exposure generates the electron-hole pairs, these ones recombine through multi-phonon excitation of Si-H vibrations. The recombination breaks the Si-H bonds and promotes the hydrogen to a transport state. When the hydrogen in the form of Si-H and dangling bond pair meets another pair of the same kind, the two dangling bonds recognizes each other leaving behind a metastable complex of two Si-H bonds [35].

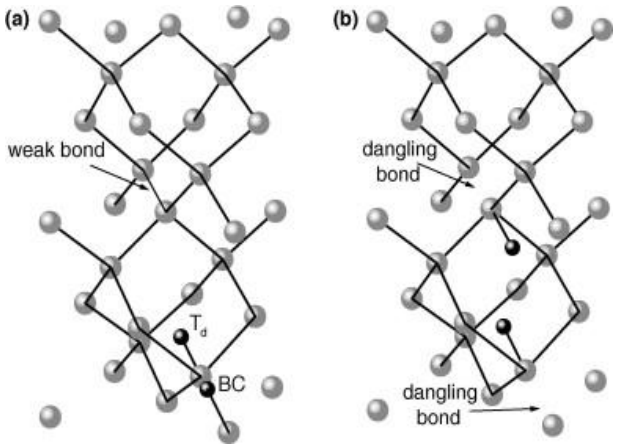

Figure 20. Metastable defects in amorphous silicon

The properties that could play a role in the Staebler-Wronski effect are:

- Disorder in the silicon network;
- Concentration of impurities;
- Hydrogen concentration and its bonding structure

Metastable defects can be created by charge accumulation, rapid quenching, short voltage pulses and extended light exposure, double-injection currents or by keV electron bombardment. Metastability requires an energy barrier between alternative states and creation of defects by external excitation. To reverse the effect thermal excitation is required [35].

The defect-creation kinetics has been studied by Stutzmann, he showed that the defect density depends on the illumination intensity and the time t [35]:

$$Nd\ (t) = const * G^{\frac{2}{3}} * t^{\frac{1}{3}}$$

Equation 4

Where:

- Nd(t) is the defect density
- G the illumination intensity
- t the time

Some solutions proposed to reduce the Staebler-Wronski effect can be:

- Make the intrinsic absorber material as thin as possible, to maintain a high electric field after degradation,

- Using more hydrogen during the deposition, this way microcrystalline silicon will be formed, and the number of dangling bonds will be reduced,

- Using silicon-germanium films (a-SiGe), it's band gap can be adjusted between 1.4 eV and 1.7 eV by only varying the germanium supplied fraction, this makes it suitable for multijunction solar cells and it acts as an intrinsic layer. As it has been said before this kind of solar cell has higher efficiencies [35], [37].

3.4 Applications of thin films

Thin films are being used a lot nowadays, they have the 9% of the global PV market. Some of the most important applications are:

- Portable lamps
- Power supply units for stand-alone systems
- Traffic signals, or on the road SOS points
- Public or garden lighting
- Weather-analysis systems
- Consumer electronics: calculators, watches, battery chargers, ventilation systems, car sunroofs.
- Pumping systems
- Facades and roofs: solar tiles, semi-transparent PV windows [1].

Apart from the uses that they have as solar cells, they can also be used in chemistry, mechanical, optic or magnetic applications.

4 Potential application in the future

Amorphous silicon thin film solar cells have been studied for years and high efficiencies have not been achieved due the Staebler Wronski effect, but in the last few years some other solar cells have been developed and amorphous silicon might be useful for those. This kind of solar cell correspond to the third generation and are the tandem or multijunction solar cells. One of the most efficient solar cells in the market nowadays is the HIT solar cells (Heterojunction with Intrinsic Thin-layer). It has been demonstrated that the perfect bandgaps for a two-gap device are at 1.1 eV and 1.8 eV. Amorphous silicon has a bandgap of 1.7 eV, so it makes it a quasi-perfect material for the construction of this kind of solar cells. Amorphous silicon is used in tandem cells as a top cell with one or two lower cells of an alloy with Ge (a-Si:Ge), which lowers the bandgap. This kind of solar cell is made with many different techniques but the most important would be the chemical vapor deposition or other vacuum deposition techniques. The lack of a need for crystallization and the vapor-phase deposition means that much less energy is required for the production process [17].

The HIT solar cell uses a very-thin and high-quality amorphous silicon layer to form the Hetero-Junction. The structure is composed by an intrinsic amorphous silicon layer, a doped amorphous silicon layer, and a TCO (transparent conductive oxide) layer. The layers are deposited on both sides of a crystalline silicon substrate. Grid electrodes are also placed on both sides of the doped amorphous silicon layer, for the fabrication of the electrodes, high-hardness alloy metals are used. Therefore, the HIT solar cell has a symmetrical structure [38]. The symmetrical structure of the HIT solar cells is also suitable for a bifacial module solar cell that can lead to higher harvestings of solar power over the system life span [39]. The output power of the HIT double solar cell is higher than that of the single-sided HIT module. The HIT double produces 10.9% more output power than the single-sided HIT module [38].

A high-quality intrinsic amorphous silicon layer can passivate the surface dangling bonds of the crystalline silicon substrate. Further, all of the temperatures in the fabrication process for HIT solar cells are below 200 ºC, which allows it to preserve the initial high-

level quality of the crystalline silicon substrate [38]. This kind of solar cell has a less stressed structure, than crystalline solar cells, which is very important for thinner wafer processing [40].

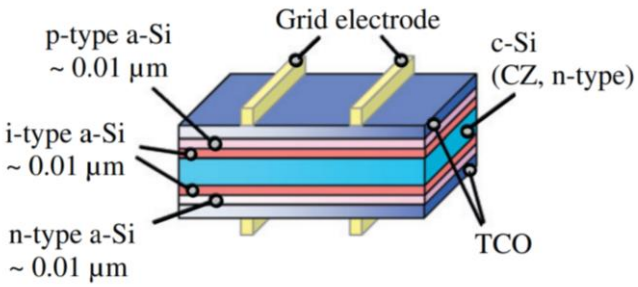

Figure 21. Structure of a HIT solar cell

The use of a-Si:H - Si HIT tandem cells provides an interesting research opportunity where the added benefits of the high performance gained by two junction cells are merged with the low cost and environment friendliness of readily available silicon stock.

From this literature review it can be concluded that the wide availability and non-toxicity of thin film silicon, together with its thickness and band gap tenability, makes it a good material for the production of thin films and it has a potentially large future in HIT solar cells. Experimentations conducted in this study were done in order to find the adequate deposition parameters for thin film hydrogenated crystalline/ amorphous silicon and identify potentials applications.

CHAPTER 2. EQUIPMENT

1. PECVD (Plasma Enhanced Chemical Vapor Deposition)

Chemical vapor deposition (CVD) is a chemical process used to produce high performance, high quality solid materials over a substrate by a chemical reaction in the vapor phase. The substrate is exposed to one or more volatile precursors (for the production of amorphous silicon two volatile precursors are normally used: silane and hydrogen), they will react and/or decompose over the substrate surface to produce the desired deposit. Plasma-Enhanced Chemical Vapor Deposition (PECVD) is a type of CVD that uses plasma to enhance the chemical reaction rates of the precursors, there are others like thermal CVD, higher frequency radiation named as photo assisted CVD, metal organic CVD or metal organic vapor phase CVD [41].

The first patent describing a CVD process was by Jonh Howart et al [41], for black carbon production used as a pigment, but it was not successful. Then it was used with the electric lamp, Sawyer and Mann et al [41] improved this process, but it was too fragile. The first deposition of silane by CVD dates in 1909 [42] and 1927 [43]. The change came into this technology when the micro electrics industry was developed in the mid 1970`s [41]. This lead to a very high quality thin films with a precise uniformity, control, composition, and doping of the layers.

The equipment used for the preparation of the samples at the laboratory is a Plasma Enhanced Chemical Vapor Deposition. A plasma can be defined as a partially ionized, quasi neutral gas, consisting of an equal number of positive and negative charges, and a different number of non-ionized neutral molecules. To maintain the plasma for a long time an external energy source is required, it can be either an electrical discharge, radio frequency discharge (RF), alternating current (AC) or a direct current (DC) discharge [44]. The plasma is normally produced at low-pressure discharges in a vacuum chamber, the wall of which is separated into two parts. One part is electrically grounded, and the other is used as an antenna or RF electrode [45].

A plasma deposition system consists of several subsystems, each of them will provide a different function:

- Gas handling system; it includes the process gas storage, mass flow controllers to measure and control the different gases used to feed the reactor, and piping.
- Vacuum system; it includes pumps and pressure controllers. Two different types of pumps are used: high vacuum rotation pumps and turbomolecular pumps.
- Cooling water supply for the turbomolecular pump.
- Computer; used to control the system.

Most of the gases used for the deposition are hazardous, they can be corrosive, flammable, explosive, and/or highly toxic. So extreme care must be taken while dealing with these gases. In general, a.o. flow limiters are installed between the valve from the supply cylinder and the pressure regulator, this is used to prevent excessive gas flow in case of breakdown of the regulator, cross-purge assemblies (to purge the regulators and prevent the release of the gas when exchanging gas cylinders when they are empty) [44]. The ISE laboratory has a specially designed silane gas handling panel which allows to purge the manifolds with nitrogen and vacuum the gas system prior to the introduction of silane.

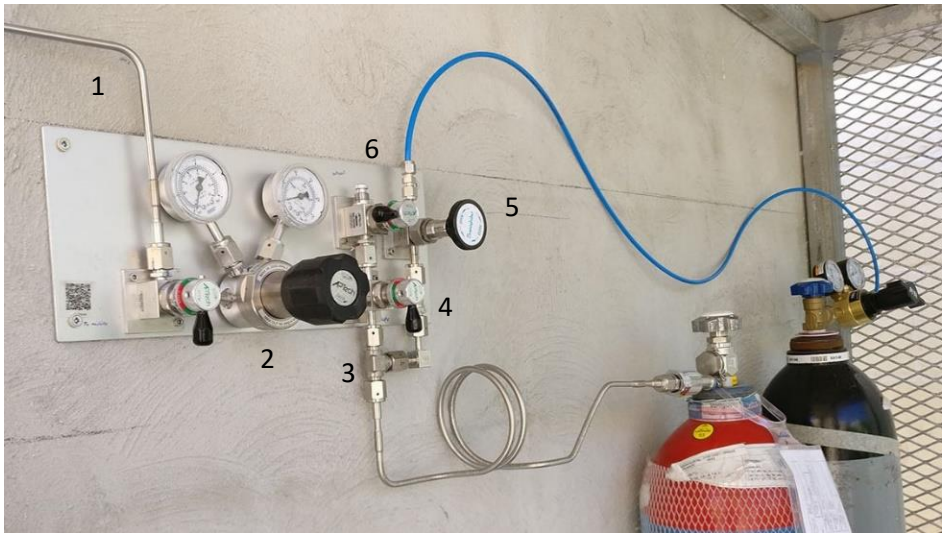

Figure 22. Gas handling system in the ISE.

In Figure 22 the gas handling system in the ISE is shown. It is composed by different valves, gas exits and entries:

1. Gases exit to PECVD
2. Regulator
3. Silane entry
4. Two-way valve
5. Nitrogen purge valve
6. Ejection valve

The first cylinder corresponds to the silane and the second one to the hydrogen.

The generation of the plasma set-up is shown in Figure 23, this is the central part of the most commonly used deposition systems. The power to the reactor system is delivered by a power supply connected to the chamber via RF circuitry. Power supplies consist of a generator and an amplifier combined in one apparatus, with a fixed frequency. The radio frequent power is capacitively coupled to the discharge between the two electrodes. The mixing of silane and hydrogen is then introduced between the two electrodes, and the reaction products and unreacted gas are pumped away from the chamber/reactor [44].

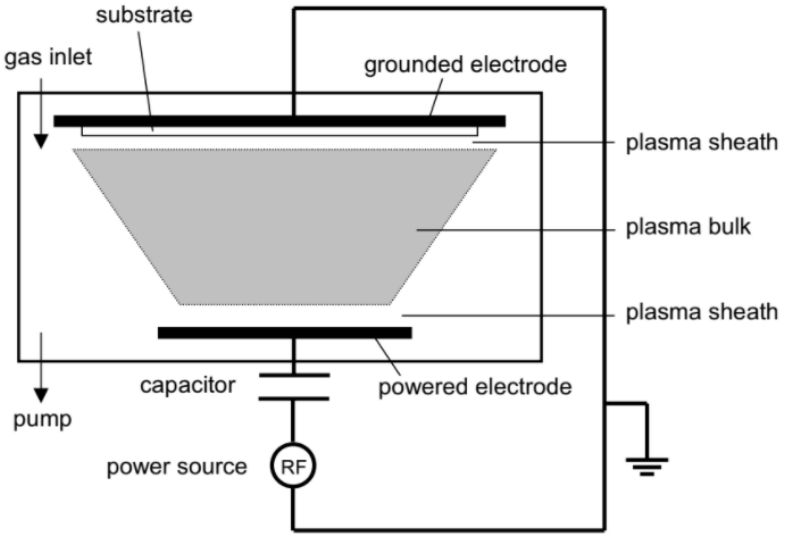

Figure 23. Plasma set up. [44]

Using the planar diode geometry, p-i-n devices have been made in single-chamber reaction systems, in this kind of systems, cross-contamination can occur. After deposition, small amounts of (dopant) gases might remain in the chamber due to adsorption on the walls. These residual gases will desorb during following depositions and may enter as impurities in the amorphous layer, or in contaminated interfaces. High impurities levels combined with contaminated interfaces in the layers have a negative influence on the electrical properties of the layers, it results in a lower efficiency on the solar cells [41].

The properties of the coating depend on the operating conditions such as pressure, temperature, radio frequency, RF power, silane, and hydrogen flow rate, geometry. The effect of the different conditions has been studied [44].

- Pressure variation:

While working with the plasma the relative pressure of hydrogen slowly increases, and the relative pressure of silane slowly decreases. This is caused by an increase in silane depletion at higher total pressures, which results from a higher power dissipation by the electrons. In Figure 24 it can be observed that for higher total pressures the deposition rate is higher, which means that the coating will be thicker. While coating the pressure cannot be too high, otherwise this gas-phase will polymerize.

- RF frequency variation:

At high RF-frequencies, more power is used for the heating of electrons, which leads to a higher dissociation of silane. As a result, more hydrogen and silane radicals are produced, so as molecular hydrogen. A saturation is observed when all power is consumed by the electrons. In Figure 24 it can be observed that for higher RF frequencies the deposition rate is higher (same as for higher total pressure).

- Plasma power variation:

Andujar et al. [44] found that the relation between the deposition rate and electrical power depends on the pressure. When the plasma power density is increased, the deposition rate is also increased up to the point where the gas flow rate (silane and

hydrogen) becomes the limiting factor. At low power levels, a large part of the silane remains undissociated, and the films contain only silicon monohydrides. At high power levels, the silane is strongly dissociated, and the films contain a large amount of silylene. The electrical properties (photo and dark conductivity) first decrease and then increase upon increasing power, and the optical band gap increases with increasing power [41].

In Figure 24 it can be seen that the deposition increases as a function of plasma power. When the deposition rate increases a lot, some disadvantages appear such as poor film quality and powder formation.

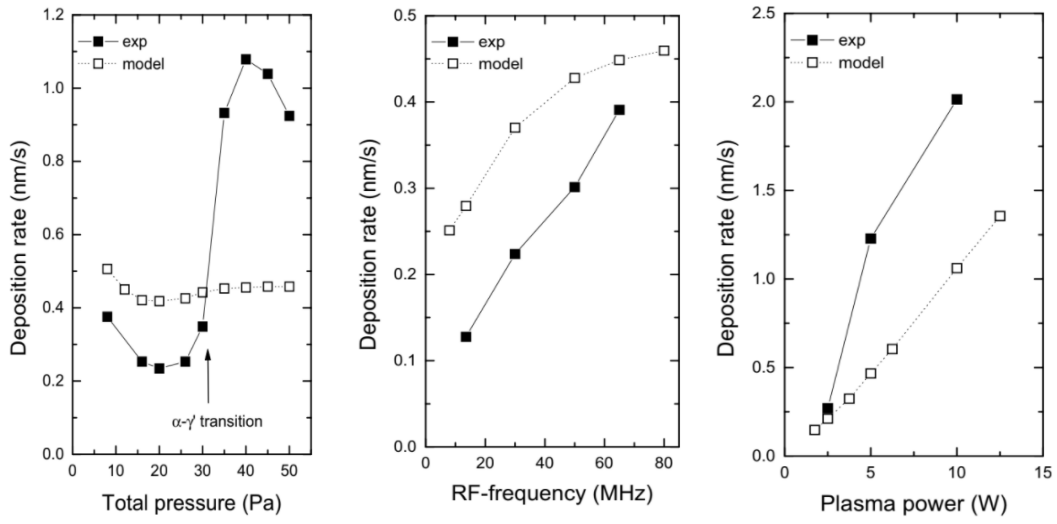

Figure 24. Graph of deposition rate vs (a) Total pressure (Pa) (b) RF-Frequency (MHz) (c) Plasma Power (W). [45]

- Gas flow:

At high gas flow rates, low residence time and low depletion, the deposition rate increases, and better film quality is obtained.

- Substrate temperature:

This substrate temperature is very important, it affects directly the kinetics of adsorption and desorption, surface diffusion, growth precursors, and incorporation. The deposition rate is practically independent of the surface temperature, while the disorder, the hydrogen content and the optical band gap decreases with increasing

temperature. An optimum temperature for deposition is 250 ºC [44]. At this temperature the material contains only Si:H bonds. When higher temperatures are used a lower content of hydrogen is found in the films and it leads to higher defect densities.

- Flow rate:

As it has been said before, the flow rate influences the structure of the coating. When the amount of hydrogen is increased the microcrytallinity of the sample is increased and its band gap is reduced.

The chemical reactions that have been identified during the deposition are summarized in Table 2 [44]:

Chemical reaction	Reference
$H + SiH_4 \rightarrow SiH_3 + H_2$	[46], [47]
$H + Si_2H_6 \rightarrow Si_2H_5 + H_2$	[46], [47]
$H + Si_2H_6 \rightarrow SiH_3 + SiH_4$	[46]-[48]
$H + Si_nH_{2n+2} \rightarrow Si_nH_{2n+5} + H_2$	[46]-[48]
$H_2 + SiH_2 \rightarrow SiH_4$	[46]-[48]
$SiH_4 + SiH_2 \rightarrow Si_2H_6$	[46]-[48]
$Si_2H_6 + SiH_2 \rightarrow Si_3H_8$	[46]
$SiH_2 + Si_nH_{2n+2} \rightarrow Si_{n+1}H_{2n+4}$	[46]
$2\,SiH_3 \rightarrow SiH_2 + SiH_4$	[46], [49]
$SiH_3^- + SiH_2^+ \rightarrow SiH_4 + SiH_2$	[50]
$SiH_3^- + Si_2H_4^+ \rightarrow SiH_3 + SiH_2$	[50]
$SiH_3^- + H_2^+ \rightarrow SiH_3 + H_2$	[50]
$2\,Si_2H_5 \rightarrow Si_4H_{10}$	[46]

Table 2. Chemical reactions carried out inside the plasma. [44]

During the growth process of amorphous silicon, the SiH_3 radical is the dominant chemical species. When the SiH_3 radical reaches the film surface, it starts to diffuse over it. While the surface diffuses, the SiH_3 abstracts the bonded hydrogen over the surface-covering, forming SiH_4 and then covering a the dangling bond on the surface (growth-site formation). When another SiH_3 diffuses toward the surface, the dangling-bond site will find the bonding site and form a Si-Si bond, this is how the film grows [51]. This process is shown schematically in Figure 25.

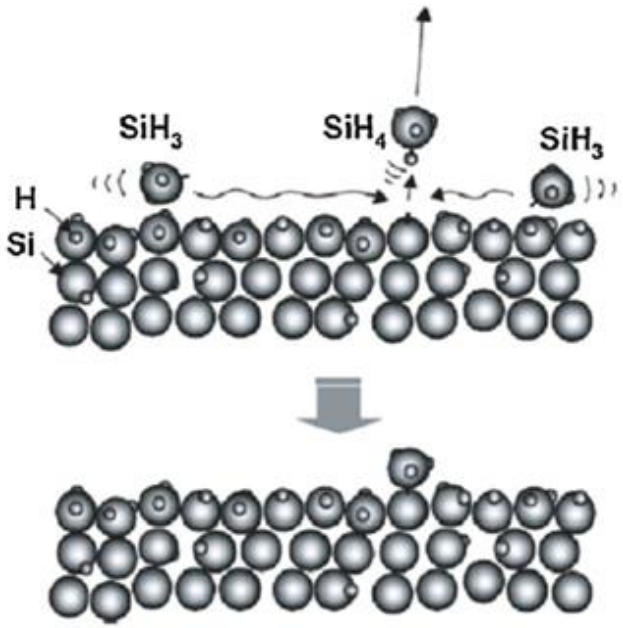

Figure 25. Surface-diffusion model for the surface-growth process of a-Si:H. [51]

Usually the remaining part of the total SiH_3 flux is reflected by the surface. The adsorbed SiH_3 is form as follows:

- The SiH_3 abstracts the bonded hydrogen over the surface-covering forming SiH_4. It is also possible that two SiH_3 radicals combine over the surface forming Si_2H_6
- Once the SiH_3 diffuses over the surface, it sticks on the dangling-bond site forming the Si–Si bond. When the SiH_3 building unit sticks to the dangling-bond site, it forms the Si–Si network, the following incorporation is controlled by the nano- and micro-scale self-organization processes.

2. Spectrometric Ellipsometry

Spectrometric ellipsometry was developed by Drude in 1887 [52]. He derived equations for ellipsometry which are still used today.

Ellipsometry is a non-destructive optical measurement technique that characterizes light transmission or reflection, absorbed or scattered from any transparent or semitransparent medium. The signal depends on the properties and the thickness of the material. The key of ellipsometry is that it measures the change in polarized light upon light transmitted by a sample or reflected on a sample and then is compared with a model. The name of 'ellipsometry' comes from the fact that polarized light upon light reflection often becomes 'elliptical' [52]. This technique can be used for the characterization of substrates, single layers and multilayers of optically interactive materials, including solar cells. It measures layer thickness from mono-atomic layers to micrometers.

Two values are measured by using elipsometry; (Δ and ψ). These represent the phase difference and the amplitude ratio between light waves known as s- and p- polarized light waves.

In ellipsometry, the spectra are measured by changing the wavelength of light. Usually, the spectroscopic ellipsometry measurement is carried out in the visible or ultraviolet region, but measurement in the infrared region has also been performed widely.

There are two dominant restrictions while using ellipsometry measurements [52]:

- The surface roughness of samples: it has to be small. When the reflected light intensity is reduced severely because of the surface roughness, the ellipsometry measurement becomes more difficult, as ellipsometry determines a polarization state from its light intensity. If the size of surface roughness exceeds 30 % of a measurement wavelength, generally measurement errors increase, but this effect depends on the type of instrument used.

- The measurement must be performed at oblique incidence, the incidence angle is chosen in order to maximize the sensitivity of the measurement. The choice of the incidence angle varies according to the optical constants of the different samples. For semiconductors, the typical angle incidence is 70–80 degrees. At normal incidence, the measurement becomes impossible, since s- and p-polarizations cannot be distinguished at this angle.

Light is polarized when electric fields of light waves are orientated in a specific direction. When the oscillation direction of light waves is random, the light is called natural or unpolarized light. If the light waves propagate in the exact same direction, the polarization is expressed by superposing the two electric fields, in order to describe the polarization, the phase difference between the light waves has to be taken into account. Because of this phase difference, the state of polarization will change into various states from circular polarization to linear polarization [52].

When light is transmitted or reflected by samples at oblique incidence, the light is classified into s- and p-polarized light waves, it depends on the oscillatory direction of its electric field. In p-polarization, the electric fields reflected and the incident light waves oscillate within the same plane, they oscillate in parallel planes. This plane is called the plane of incidence. In s-polarization, the electric field of the incident and reflected light waves oscillate in perpendicular planes.

There are three types of polarization [52]:

- Linear polarization, it has a phase difference between the electric fields parallel to the x and y-axes of 0.
- Right-circular polarization, it has a phase difference between the electric fields parallel to the x and y-axes of $\pi/2$.
- Elliptical polarization, it has a phase difference between the electric fields parallel to the x and y-axes of $\pi/4$.

In Figure 26, the difference between the states of polarization with a different phase, it changes from 0 to 2π, can be seen.

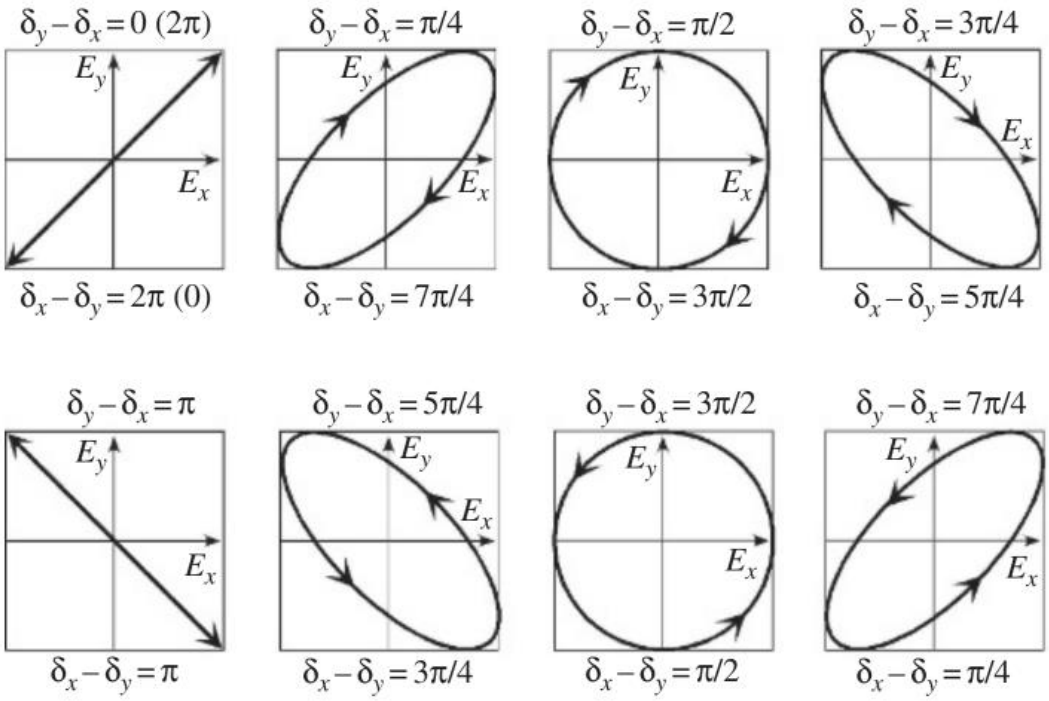

*Figure 26. Variation of the state of polarization with a phase difference (*δx −δy and δy −δx). [52]

When s- and p-polarized light waves are irradiated onto a sample at an oblique angle, the film thickness and the optical constants of the sample are measured, from the change in the polarization state. Because of light reflection on the sample, p- and s-polarizations show different changes in amplitude and phase. When the sample structure is simple, the amplitude ratio ψ is characterized by the refractive index n, while the phase difference Δ represents light absorption described by the extinction coefficient k (or optical anisotropy for light absorption, it is a dichroism, which represents optical anisotropy for refractive index). In this case, the two values n and k can be determined directly from the two ellipsometry parameters obtained from a measurement by applying the Fresnel equations. This is the basic principle of ellipsometry measurement [52].

The amplitude ratio represents the angle determined by the amplitude ratio between reflected s- and p-polarizations, and can be defined as:

$$\tan(\psi) = \frac{r_p}{r_s} = \left(\frac{E_{rp}}{E_{ip}}\right) \Big/ \left(\frac{E_{rs}}{E_{is}}\right)$$

Equation 5

The phase difference can be defined as:

$$\Delta = \delta_{rp} - \delta_{rs}$$

Equation 6

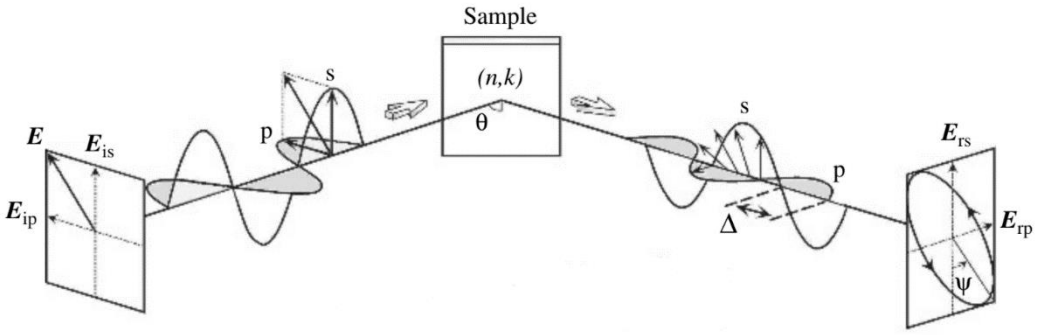

Figure 27. The measurement principle of ellipsometry

The ellipsometer is composed of the following parts [53]:

- A light source: usually uses a high-pressure xenon lamp, a gas discharge is carried out between two electrodes that are inside of the lamp.
- Linear polarizer: this device transforms the unpolarized incident light into a linearly polarized light, with the correct angle of rotation of the axis of the polarizer. It works by suppressing one component of the incident light, allowing only the other component to pass [52].
- Compensator: there are many kinds of compensators such as a retarder or a quarter wave plate, this last one is a phase-modulator, it is located in the path of the incident light beam. They are used to displace the phase of one component of the incident light.
- The sample to be analyzed, in this case, it would be the amorphous silicon coated over a glass or pure silicon.
- The analyzer: this device is another polarizer, it determines the state of polarization of a beam after it has been altered.
- Detector: receives the polarized light.

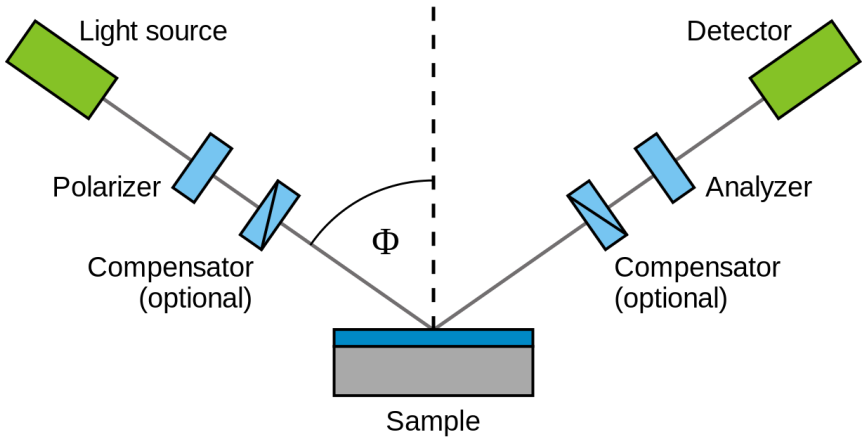

Figure 28. Set up of the ellipsometry

In order to fit the samples after the measurements two dispersion laws have been used, Tauc-Lorentz and Gauss.

Gauss dispersion laws are typically used for amorphous materials or glasses.

Tauc-Lorentz has been used to model the dielectric function of the amorphous material or transparent conductive oxide, in general, is used for insulators. It describes the behavior of a transparent or weakly absorbent material such as an insulator or a semiconductor. Tauc-Lorentz allowed us to gain insight on the band gap energy of the material.

3. FTIR (Fourier Transformed Infrared Spectroscopy)

The Fourier Transformed Infrared Spectroscopy is a method used to determinate the structure of molecules, based on the absorption of infrared radiation of the molecules [54]. When the sample is exposed to infrared radiation, the molecules selectively absorb radiation of a specific wavelength, this will cause a change in the dipole moment of the molecules contained in the sample. Following, the vibrational energy levels of the molecules pass from ground state to excited state. With the vibrational energy gap, the frequency of the absorption peak is determinate. The number of absorption peaks in the sample is related to the number of vibrational freedom of the molecule. The

intensity of absorption peaks in the sample is related to the change of dipole moment and the possibility of the transition of energy levels. So, by analyzing the infrared spectrum, a lot of information about the molecule structure can be obtained [54].

Before FTIR was used, there were others infrared spectrometers, in fact, there have been three generations of spectrometers [54]:

The first generation of infrared spectrometer dates from the late 1950s [55]. It is based on a prism optical splitting system. The prisms usually were made of NaCl. This technique has some limitations or problems. The sample particle size is extremely strict so is the content of water in the sample. The scan range is narrow-minded and the repeatability is poor. So, for all these problems, the first generation of infrared spectrometer is no longer in use.

The second generation of infrared spectrometer was developed in the 1960s. It uses gratings as the monochromator. Compared to the optical prims the grating is much better. But still, it has a few weaknesses like low sensitivity, poor wavelength accuracy and low scan speed which lead to the invention of the third generation of infrared spectrometer.

The invention of the third generation of infrared spectrometer, Fourier Transform Infrared Spectrometer, this spectrometer replaced both generations. With this replacement, infrared spectrometers became powerful.

The range of Infrared region is divided in three ranges:

- Near infrared (0,78-2,5 μm), this is the most energetic level and is used for quantitative analysis.
- Mid infrared (2,5-50 μm), this range is useful for organic sample analysis. This region can also be known as the thermal region.
- Far infrared (50-1000 μm), this region is used for vibrations of molecules containing heavy atoms, bonding energies, molecular skeleton vibrations and crystal lattice vibrations.

The infrared spectrum is a molecular vibrational spectrum. The molecules have translational and rotational motion, and each atom has their own motion. In order to see the vibration under the infrared spectra, the changes must occur in the permanent dipole. There are different modes of vibrations when they have a change in the length of a bond asymmetric, symmetric; or when they have a change in angle between a group of atoms twisting, scissoring, wagging and rocking. In the twisting, wagging and rocking mode there is no change involved in the length, the only change is the angle. The only thing that distinguished the rocking and the wagging is the plane that the atoms are moving.

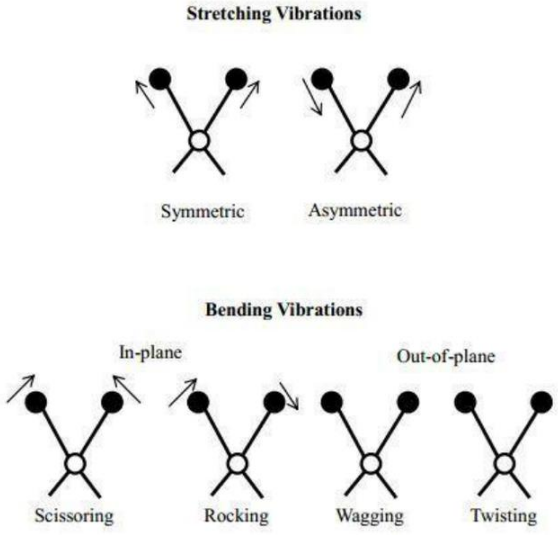

Figure 29. Vibrational molecular modes. [56]

This technique is used for most molecules because they are infrared active, there is only one small amount that cannot use infrared spectrometry because they have zero dipole change in the rotation and vibration of the molecules. These are the homo-nuclear diatomic molecules, like O_2, N_2 or Cl_2, so FTIR is used for polyatomic molecules.

FTIR has many advantages, it is capable to analyze samples in different states like gas, liquid or solid. The signal-to-noise ratio is higher than the other generations. The error is very low, in the range of 0,01 cm^{-1}. Short scan time at any frequency (approximately 1 s). Very high resolution (0,1 ~ 0,005 cm^{-1}). The three regions of the infrared spectra provide a wide range of scan [54].

The FTIR is composed of different parts:

- A source generates light, usually, a tungsten-halogen lamp is used, but also a silicon carbide lamp or a mercury discharge lamp can be used.

- Interferometer: inside of it there is a beam splitter. The beam splitter is the most important part of the interferometer. Basically, it is a half-silvered mirror, the beam splitter reflects more or less half of the incident light beam and simultaneously transmits the other half. One of this half split light beam goes to the interferometer stationary mirror while the other travels to the moving mirror. The two beams are reflected by the mirror and they travel back to the beam splitter, they are again half reflected and half transmitted. The result is that one travels to the source and the other goes to the detector. When the two half beams travel back to the beam splitter they recombine, and the difference in the path length creates an interference pattern or an interferogram. The interference pattern changes with the displacement of the moving mirror [57].

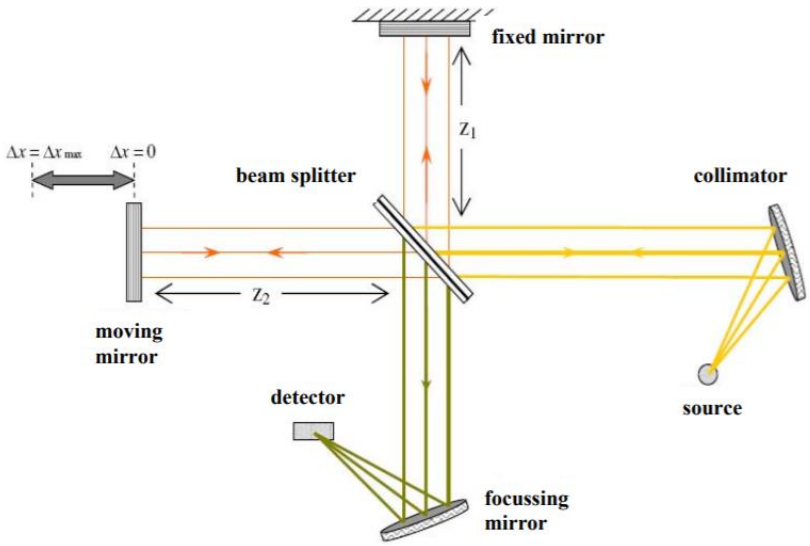

Figure 30. Interferometer diagram. [57]

- The sample, will absorb the light according to its chemical properties.

- Amplifier and Analogical/Digital converter for the signal.

- A detector, usually pyroelectric detectors are used, they react to changes in temperature as the intensity of the infrared radiation goes over it. This kind of detectors operates at ambient pressure.

Finally, the signal is sent into a computer, it uses a mathematical function called the Fourier transform, it allows us to convert an intensity-vs-time spectrum into an intensity-vs-frequency spectrum.

4. Contact angle

The contact angle is where a liquid-vapor interface meets a solid surface. With this technique the wettability of the solid surface can be quantified through the Young-Laplace equation (is not linear, is an elliptical partial differential equation). Every vapor, liquid and solid system at a given pressure and temperature has a unique equilibrium contact angle. In practice some hysteresis is observed, it varies from the receding contact angle (minimal) to the advanced contact angle (maximal). The equilibrium contact is between those values, and it can be calculated from them. The equilibrium contact angle reflects the relative strength of the vapor, liquid and solid molecular interaction [58].

The surface roughness affects the contact angle and the wettability of the surface. The effect of roughness depends on where the drop falls, because once it hits the surface the liquid can either wet the groove or leave an air pocket.

If the liquid drop spreads completely over the solid surface it means that the liquid and the solid molecules are strongly attracted to each other, this will correspond to a contact angle of 0°. In general, if the contact angle is less than 90°, the solid surface is called hydrophilic [59] and if the contact angle is larger than 90°, the solid surface is called hydrophobic. If the surface is highly hydrophobic the contact angle can be as high as 120° [60]. There are some materials with very high rough surface, this kind of material

can have a contact angle even greater than 150°, due to the presence of air pockets under the liquid drop. This kind of surfaces are called superhydrophobic.

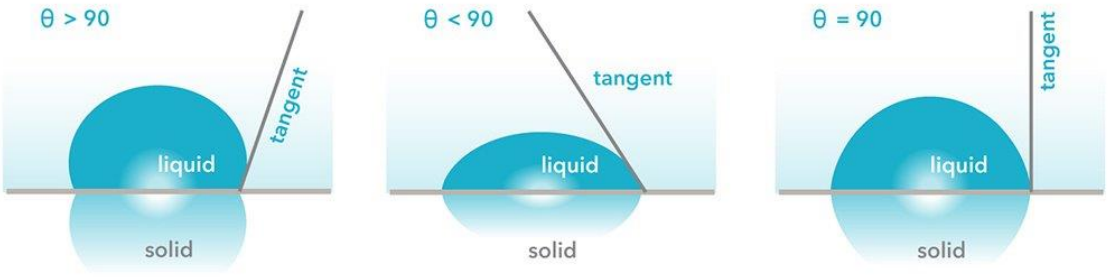

Figure 31. Different cases of contact angle

When the water drop is formed in the surface of the sample, the balance between the three phases interphase can be expressed by the Young's equation.

$$\gamma_s = \gamma_{sl} + \gamma_l * cos(\theta)$$

Equation 7 [59]

Where:

- γ_s is the surface free energy of the solid
- γ_{sl} is the interfacial tension
- γ_l is the surface tension of the liquid
- θ is the value of the contact angle measured.

It is known from Fox and Zisman (1950) [61] that cos(θ) is a linear function with the surface tension liquid.

5. Atomic Force Microscopy (AFM)

The atomic force microscopy is an optic-mechanical instrument able to detect nano-newton order forces. It drags the sample and register its topography with a sounding line or with a cantilever.

The heart of the AFM lies with the cantilever/tip it can also be referred as the probe typically it has a radius of curvature at the end of 5-10 nm, they are usually made of silicon or silicon nitride, the last one is harder. The tip interacts with the sample through a raster scanning motion. The cantilever obeys the Hooke's law:

$$F = k * x$$

Equation 8

Where:

- F is the force on the cantilever
- k its spring constant
- x its deflection

The side to side and up/down motion of the cantilever scans the surface and monitores it through the "beam deflection method". The beam deflection method consists of a laser that is reflected off the back end of the cantilever and directed towards a detector that tracks the vertical and lateral motion of the probe. The cantilever can also be mounted in a holder. The dynamic modes of operation can be performed either in resonant modes (where the operation is at or near the resonance frequency of the cantilever) or non-resonant modes (the operation is at a frequency that usually is far below of the cantilever's resonance frequency).

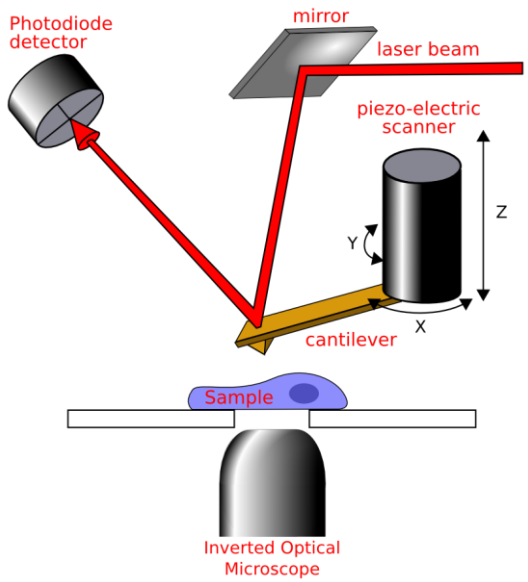

Figure 32 Sketch of the operational principle of AFM. [62]

CHAPTER 3. EXPERIMENTAL PROCEDURE

1. Cleaning procedure

The amorphous silicon was produced over two different substrates, boro-silicate glass and silicon. The thickness of the substrates were 200 µm and 297 µm respectively. The area of the boro-silicate glass samples has an area of 4 cm^2. For the silicon samples, at the beginning unpolished silicon samples were cut in squares and polished in the laboratory, but the wafer was extremely thin and either it broke during the polishing process or while removing it from the holder. So double-side polished wafer was bought, they were circular wafers of 50 mm diameter which were cleaved using a diamond tip along the atomic plane into 4 quadrants.

The silicon wafers were bought to Siegert wafer, and had the following characteristics:

Diameter:	50.8 ±0.3 mm
Material:	Silicon
Growth:	FZ
Grade:	Prime
Type/Dopant:	Intrinsic
Orientation:	<100> ±0.5°
Resistivity:	>10,000 Ohm-cm
Thickness:	279 ±25 µm
Surface Finish:	Double Side Polished
Flats:	1 primary Flat, SEMI-Std.
TTV:	<10 µm
Bow:	<30 µm
Warp:	<30 µm
Particles:	No particle guarantee
Packaging:	Cassettes

Before the silane deposition, a cleaning procedure was carried out on both substrates. Different processes were tried in the boro-silicate glass until the best procedure was found, it consists on two steps, the first one is a wet procedure and then a plasma cleaning procedure.

The wet process was composed by five different steps. First, individual substrates were cleaned with nitrogen is case some dust was stick on it, then they were introduced in a

glass beaker with distilled water and soap for five minutes in a ultrasonicator, following washing with distilled water. After this, they were introduced in another glass beaker with distilled water for another five minutes, past the five minutes they were washed with isopropanol, and then introduced in a beaker filled with 99.9% isopropanol for another five minutes. Once this dipping procedure was finished the samples were dried with a lateral jet of nitrogen gas, as soon as possible so dust would not get attached to them again. One of the other methods was to dry it with a heater, but this procedure was not successful. This process was based on a cleaning procedure carried out by a previous student at the laboratory.

The final step in the cleaning procedure was to immerse the substrates in a hydrogen plasma, so for this step, the samples were introduced in the chamber of the PECVD and immersed for 60 s at the pressure of 0.4 mbar, a power density of 0.146 W/cm^2 and a flow of hydrogen of 10 sccm [63].

The silicon substrates were delivered with clean room handling certification and they did not require wet cleaning steps. Such substrates were handled in a spacially constructed glovebox and only pre-cleaned with the hydrogen plasma step just before deposition. In this case the hydrogen plasma was created with a flow of hydrogen of 20 sccm.

2. PECVD (Plasma Enhanced Chemical Vapor Deposition)

The first step in the process was to clean manually the chamber from any dust, clustered silane or hydrogenated compounds from previous depositions. The chamber was vented with nitrogen till it reaches atmospheric pressure and it could be opened, then the electrodes surfaces and the plate where the samples were placed are wiped with isopropanol to remove all the dirt. Finally, following re-pumping, an argon plasma was made at high power density, about 0.146 W/cm^2 in order to ablate any residuals.

Figure 33. Set up of the PECVD

After this the chamber must be vented again in order to introduce the substrate in it. The initial hydrogenated amorphous silicon layers were deposited over the boro-silicate glass as a means for familiarization with the operation of the highly complex plasma enhanced chemical vapor deposition (PECVD) machine. Two metallic holders were manufactured in order to hold the samples on the chamber's supporting base. This ensured that the samples did not change position during the deposition process and were not displaced during the venting of the chamber to atmospheric pressure.

Once the substrate was placed in the chamber, the vacuuming sequence was done, the pressure difference between the chamber and the rest of the system is high, so the pumping cycle cannot be started right away. Two valves that isolate the vacuum system from the chamber were required to be opened for the pressure to start going down. The rough valve, this one is an all or nothing valve, and the throttle valve, this one can be open by setting a set point, either in pressure (to control the pressure inside the chamber) or by position (to control the percent of open valve). In this case the position

is selected, at the beginning it is only set a 5% so to avoid a large gas inrush in the vacuum pumps. When the pressure in the chamber and in the system stabilizes and starts to be similar (at around 1 mbar) the position of the throttle valve was slowly increased until 100%. After this, the high vacuum pumping cycle was initiated, where the roughing valve is isolated and a turbo-molecular pump is used to continue pumping. The pumping cycle must be kept working until the pressure reaches $1x10^{-6}$ mbar or less. At this moment the temperature is also set because it takes some time to reach the desired temperature. While setting the temperature, it must be taken into account that the temperature in the chamber is not the same than the deposition temperature due to thermal losses within the chamber. The chamber temperature must be calculated as a function of the deposition temperature required, and it follows the next equation:

$$T_R = 0.6349 * T_D - 32{,}2$$

Equation 9

Where:

- T_R is the chamber temperature
- T_D is the deposition temperature

Once the adequate pressure was reached the ion gate is closed, and the turbomolecular pump goes down to a set low speed. Then the foreline valve was closed. A nitrogen purging cycle was also required; this makes sure that the evacuated silane is diluted enough to avoid any explosive mixtures forming in the system. In case that there is an alarm of the nitrogen purge, the primary purge was turned on manually prior to further pumping. Flushing the exhaust system with nitrogen takes some time, five or more minutes, so while waiting for the flow rates are set (first the hydrogen for the cleaning plasma). Then, the gas in chamber was turned on.

Before starting the plasma, the pressure was set with the throttle valve and when the baratron pressure transducer reached that pressure the power density of the plasma was set, in this case 0.05 W/cm^2. In the computer the value selected was the power in Watts, so before the first coating was done, the size of the deposition area was

measured with a ruler so to determine the deposition area (185x185 mm). The tuning capacitors were set to 50% engagement and the deposition time was also set. Finally, the plasma was turned on, in case it does not starts, it has to be ignited with a high voltage discharge.

For all the samples produced, the silane ratio, the distance between electrodes and the radio frequency were kept the same. From previous experiments in the laboratory, it was known that the optimal silane to hydrogen flow rate was either 1:10 or 1:5, depending on other process conditions. In this case, the ratio used was 1:10, because when the silane is less diluted the amorphous silicon particles are bigger. Table 3 shows all the post-training parameters used for the deposition of the different layers.

Substrate	Nº	P (mbar)	T_D (ºC)	t (mins)	SiH_4:H_2	Pρ (W/cm^2)	de (mm)	RF (MHz)
Boro-Silicate Glass Samples	1	1	95	10	1:10	0,1	15	13,56
	2	1	200	10	1:10	0,05	15	13,56
	3	1	100	10	1:10	0,05	15	13,56
	4	1	100	10	1:10	0,05	15	13,56
	5	1	100	15	1:10	0,05	15	13,56
	6	1	100	15	1:10	0,05	15	13,56
	7	1	150	10	1:10	0,05	15	13,56
	8	1	150	15	1:10	0,05	15	13,56
Silicon Samples	1. a-Si:H	1	100	10	1:10	0,05	15	13,56
	2. a-Si:H	1	100	15	1:10	0,05	15	13,56
	3. a-Si:H	1	150	10	1:10	0,05	15	13,56
	4. a-Si:H	1	150	15	1:10	0,05	15	13,56
	5. a-Si:H	1	100	5	1:10	0,05	15	13,56
	6. a-Si:H	1	150	5	1:10	0,05	15	13,56
	7. a-Si:H	0,4	150	5	1:10	0,05	15	13,56

Table 3. Operational conditions of the different samples

Figure 34 shows the samples coated over boro-silicate glass; samples 3 and 6 were sent to a partnering laboratory in Romania before the photos were taken.

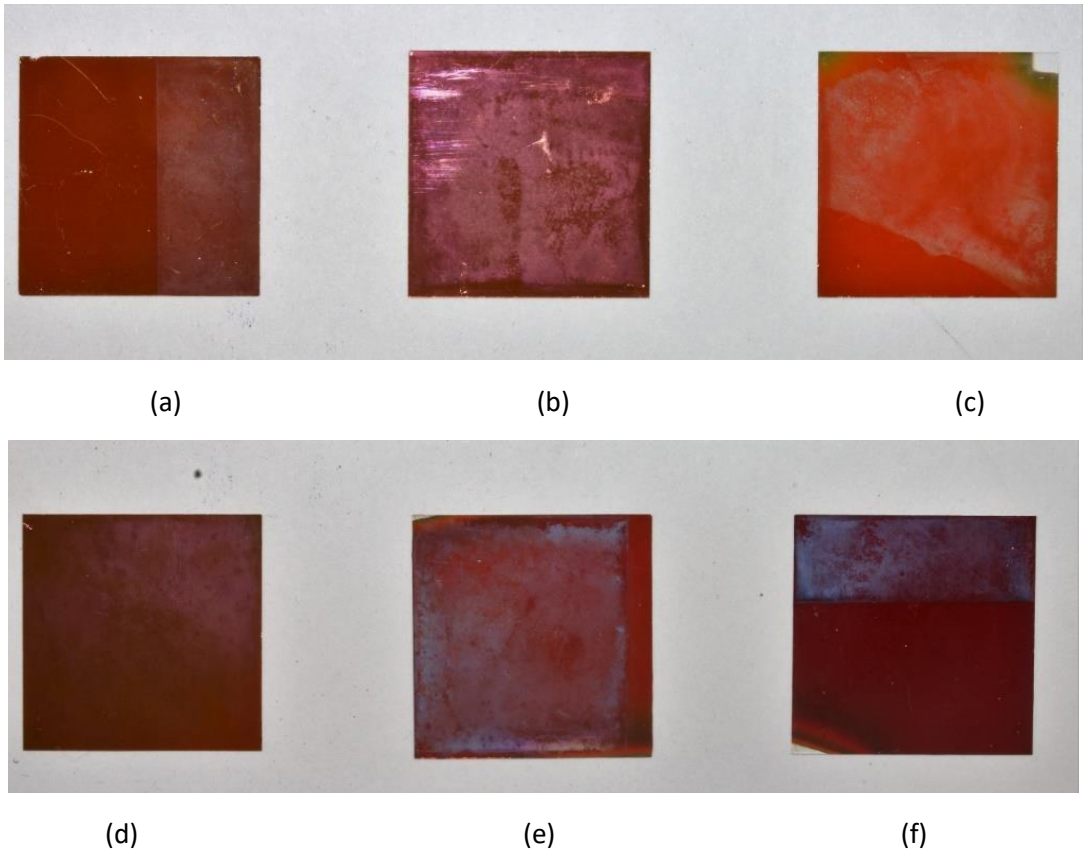

Figure 34. Samples coated over boro-silicate glass. In the first line are samples 1 (a), 2 (b), 4 (c) and in the second 5 (d), 7 (e), 8 (f).

3. Spectrometric Ellipsometry

The measurements were carried out at room temperature and atmospheric pressure. Over the boro-solicate samples three different measurements were carried out, to prove that the coatings were uniform and the film thickness was the same in the whole sample. Through the manual measurement function all the focusing and measurements were done.

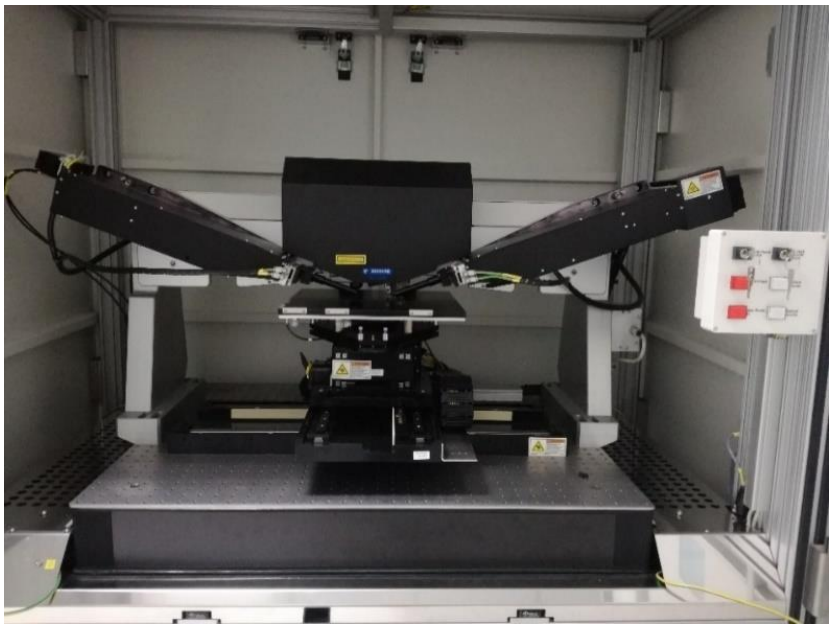

Figure 35. Set up of the Ellipsometry

First the thickness of the substrate was introduced and the stage was moved into the prefocus position. The next step is to move the stage to center, where the measurements will be done, and turn on the xenon-arc lamp. Once the sample is in the right position for the measurement, the appropriate parameters are given for the automatic focus, such as the integration time (167 ms), incident angle of 70 degrees, which with this machine, is the only angle that can be used measurement. The attenuator level selected is one, it reduces the signal intensity by a low percentage. After this the automatic focusing starts and then the ellipsometry measurement may commence.

To fit the samples after the measurements, the software SAM (Semilab's Spectroscopic Ellipsometry Analyzer) was used. Two simulation layers were used, the first one was EMA (Effective medium approximation), this film is considered as a mixture between amorphous silicon and voids, which means the surface roughness. The second layer used was dispersion laws. The two dispersion laws used were based on Tauc-Lorentz and Gauss formulae.

For the surface roughness values of the amorphous silicon were necessary to generate a dependable EMA layer model. These were measured through the use of atomic force

microscopy (AFM) on an area of 0,25 μm^2 of all samples coated over silicon. This measurement was carried out with the assistance of technicians at the ISE laboratory.

Figure 36. Set up of the AFM

4. FTIR

Fourier transformed infrared spectrometry (FTIR) was used to determinate the amount of bonding configurations of hydrogen contained in the double side polished silicon samples, at a wavelength range of 400-5000 cm^{-1}.

Before starting the measurements, some parameters must be set, such as the wavelength range, the resolution (8 cm^{-1}) or the number of scans (32).

The measurements were carried out at room temperature and atmospheric pressure. The first step was to make a background spectrum or a reference spectrum, it was made over a pure silicon substrate. This spectrum reflects the effects that the spectrometer itself has on measured spectra.

The spectrometer measures an interferogram and by using Fourier Transformation this interferogram is transferred into a single-channel spectrum. Comparing the sample measured and the background spectrum the transmission spectrum is calculated.

It was noted that due to matching absorption lines, the presence of carbon dioxide and water caused many interferences while conducting the measurements. In order to reduce the concentration of carbon dioxide and keep the amount of water vapour stable, the chamber was purged with nitrogen for one minute between every measurement. Through a literature review the exact frequencies were the dioxide carbon absorbs infrared were found [64]. Due to very strong absorption of SiO_2 at the wavelengths of interest, only the samples that had pure silicon as a substrate were measured successfully.

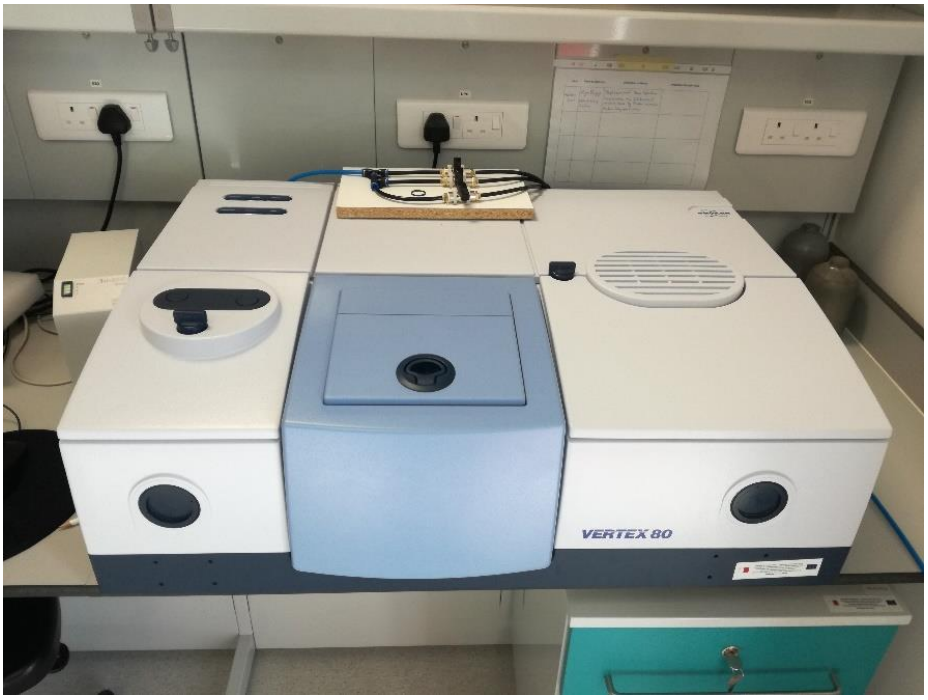

Figure 37. FTIR set up

5. Contact angle

Contact angle measurements were made in order to get an idea of the content of hydrogen in the different silicon samples. Theoretically, the dangling bonds of the unpassivated pure silicon will attract more de-ioinised water than the hydrogenated amorphous silicon, so the contact angles on the water drop should be larger in the double side polished silicon than in the amorphous silicon. This procedure was only carried out in the four first coated silicon samples, and one uncoated silicon sample.

The drop was produced with a syringe and 3 µl of distillate water, this one was dropped carefully. The pictures of the drop over the substrate were taken 30 seconds after every drop touched each sample. The angles were measured with the open source program ImageJ - Snake.

The set-up of the contact angle is shown in Figure 38, it is composed by a camera a syringe and a light.

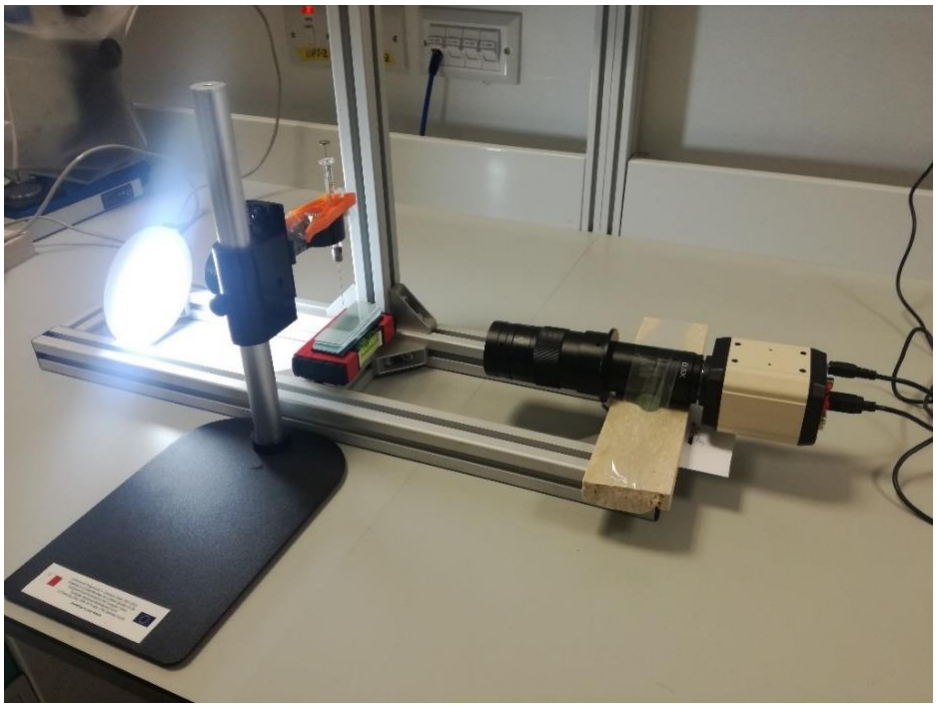

Figure 38. Contact angle set up

CHAPTER 4. RESULTS AND DISCUSSION

1. Measurement of the film thickness and the band gap

In Table 4 the results of the measurements that were fitted with the Tauc-Lorentz and Gauss models and yielded the best R^2 values are shown. The first two boron glass samples showed several inconsistencies and ellipsometric results were not fitted successfully, that's why they are not shown in the Table.

Sample	T_D (ºC)	Time (min)	Thickness (nm)	Eg (eV)	EMA (nm)	R^2
3	100	10	81,0	1,64	4,14	98,0
4	100	10	78,9	1,60	2,16	98,0
5	100	15	134,3	1,68	5,17	94,7
6	100	15	132,5	1,68	4,26	96,2
7	150	10	139,8	1,63	7,19	97,6
8	150	15	226,2	1,66	2,16	98,6
1. a-Si:H	100	10	89,2	1,66	1,13	97,1
2. a-Si:H	100	15	189,5	1,63	2,75	98,6
3. a-Si:H	150	10	106,6	1,78	0,36	98,7
4. a-Si:H	150	15	211,0	1,67	2,94	99,3
5. a-Si:H	100	5	37,4	1,70	1,29	99,7
6. a-Si:H	150	5	94,9	1,65	4,9	98,2
7. a-Si:H	100	5	19,7	1,78	7,07	98,9

Table 4. Results obtained from the ellipsometry measurement (Film thickness and band gap)

The samples were fitted in order to get the higher value of reflection phase difference (Δ) and amplitude reduction ratio (ψ), they were measured over the wavelength range 0–1600 nm. These two values are very sensitive to several parameters such as optical

constants uncertainties, native oxide thickness and also to the incidence angle, which in our case we could only use 70º. They do not have a direct physical interpretation, but they are related to the normal and parallel components of the reflected light from the film surface. The images of all the samples and fitted graphs of every silicon sample are shown in Appendix A.

Confirming an exploratory study by a preceding team working in the laboratories it was found that the thickness of the coatings increases quasi-linearly with the deposition time independent of the processing conditions. The same thing was corroborated in the experiments coated over the silicon samples. It can be seen in Figure 39 the evolution of the thickness when increasing the time at two different temperatures, 100ºC and 150ºC.

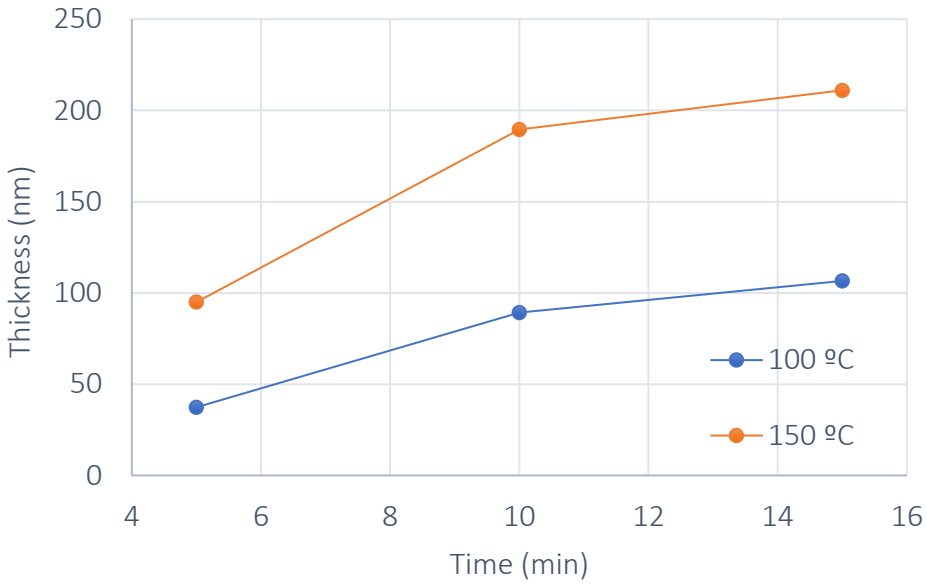

Figure 39. Effect of time over the film thickness in the samples coated over silicon.

In Figure 39 it can also be appreciated that for the same deposition time, the thickness of the coating is larger at higher deposition temperatures.

As a means to validate the approach taken, two of the boro-silicate glass samples (3 and 6, representing a 10 mins and 15 mins depositions times) were sent to the National Institute for Research and Development in Electrochemistry and Condensed Matter, which is a collaborating laboratory in Romania. The obtained thickness measurements showed good agreement with what was determined at the Marsaxlokk laboratories. The

said collaborating laboratory was equipped with a goniometer- type ellipsometer which could do measurements at different analyzing angles. The thickness obtained by them for the two samples were 82 nm and 125 nm respectively, which at 81.05 nm and 132 nm, are equivalent to the ones obtained in house.

Comparing the samples made at the same deposition conditions but different substrates it can be concluded that the growth mechanism of a-Si:H films by chemical vapor deposition, is influenced by the structural nature of the substrate. Considering that, the crystallinity of the substrate might influence in the structural ordering during the film growth.

Sample 7. a-Si:H was produced at a lower pressure of 0.4 mbar; from literature, a thinner coating is expected. This is because while energized the plasma is unstable at these pressure conditions resulting in the relative pressure of hydrogen to slowly increase while the relative pressure of silane to slowly decrease. This is caused by an increase in silane depletion at higher total pressures, which results from a higher power dissipation by the electrons. This phenomenon was confirmed and a thickness of only 19.7 nm was obtained for otherwise equivalent process conditions.

From literature review it was found that the band gap is strongly correlated to the total amount of SiH_4, and is less correlated with the total concentration of hydrogen, SiH and the SiH_4 / SiH ratio [9]. As it will be seen later form the FTIR measurements, in our samples there are no evidence of a high amount of dihydrides since there was no response in the frequency of 2100 cm^{-1}.

It was also found that the band gap is directly correlated with the film thickness and the deposition time [65]. The band gap decreases when the deposition time increases which means that the layer coating is thicker as it's been said before. In Figure 40 is represented the band gap vs the deposition time at two different temperatures.

In this case, not all the results obtained in the laboratory agree with the information found in the papers. In the case when the depositions were made at 100 ºC, effectively the band gap decreases when then deposition time increases (or the film thickness). In the case that the deposition temperature is 150 ºC the results are not conclusive; the

band gaps results seem to be random. This is indicative that the values of reflection phase difference (Δ) and amplitude reduction ratio (ψ) were not fitted properly with the models of Tauc-Lorentz and Gauss.

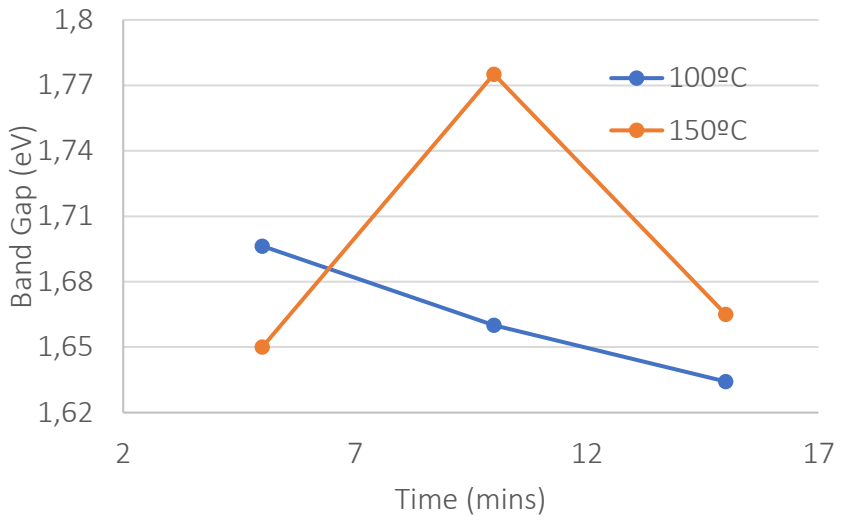

Figure 40. Band Gap vs Time of the samples coated over silicon substrate.

The values obtained for the band gap in the laboratory in Romania for the samples 3 and 6 confirms that the models generated at Marsaxlokk were not well fitted correctly. This samples were made at 100ºC and deposition time of 10 and 15 mins and the value of the band gaps obtained in Romania were 1.755 eV and 1.72 eV respectively, these values corroborate with what is normally found in literature. The values obtain in the laboratory at Marsaxlokk, which are 1.63 eV and 1.67 eV respectively, do not corroborate the papers and more effort is required to understand the factors that affect the fitting constants. The error in the measurements were 6.7% for the first sample and 2.6% for the second.

Xiao et al reported that when the deposition temperature increases the bang gap decreases [51]. In the cases studied no conclusions can be done because as it can be seen in Figure 41 in one case this theory is corroborated. The samples made at 5 and 15 mins present the opposite behavior.

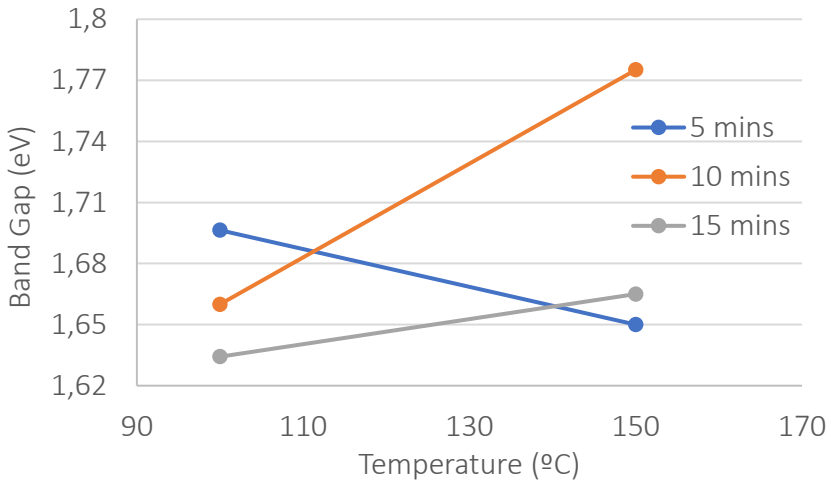

Figure 41. Effect of temperature over the band gap of the samples coated over silicon

Another parameter from the Tauc-Lorentz model that has been studied is the Lorentz oscillator broadening term. This latter term it is influenced by local potential fluctuations resulting from structural disorder [65]. In the cases studied at different temperatures in the laboratory the results are not conclusive. In Figure 42 is shown how the Lorentz broadening term changes with the deposition time.

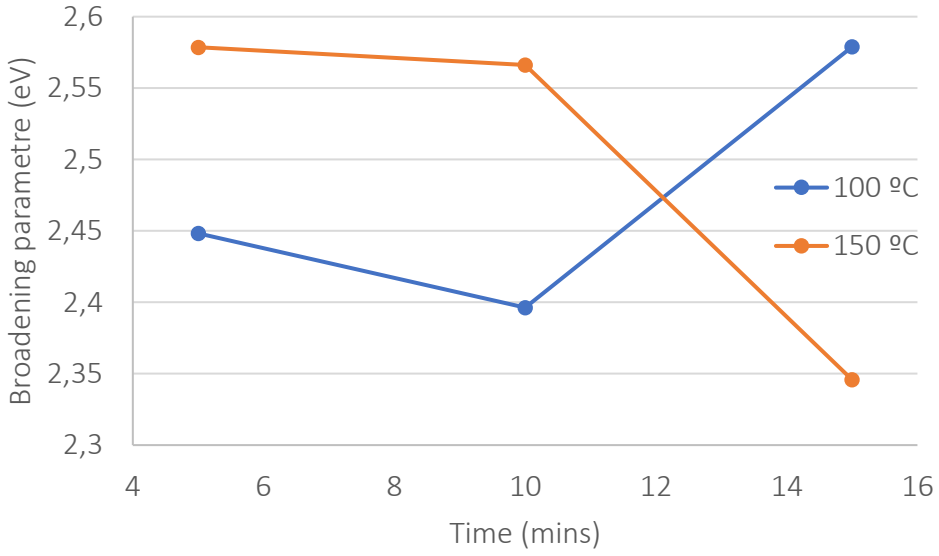

Figure 42. Broadening parameter vs time of the samples coated over silicon.

The broadening parameter decreases when the deposition time is increased. This parameter indicates that the degree of structural order is increasing as the film thickness is increased [65]. For the case of the coatings made at 150 ºC this is true, but for the

coatings made at 100 ºC the results are not conclusive. This can be again because of an inappropriate degree of fitting of the models.

From ellipsometric measurements, it was determined that the refracture index presents a maximum at a wavelength of 450 nm for all the samples. Samples made with lower deposition time have a general index of refraction which is lower than the ones made in longer times. This conclusion is in agreement with Abdulraheem *et al* [65]. In Figure 43 it can be seen the evolution of the index refraction with the wavelength of samples 1. a-Si:H and in Figure 44 sample 2. a-Si:H,, the rest of the graphs are in Appendix A.

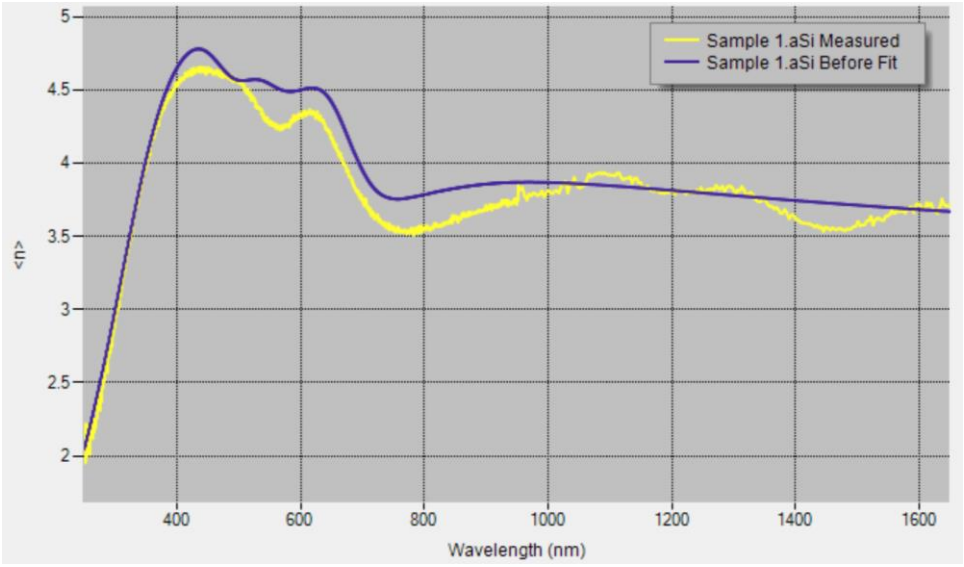

Figure 43. Index refraction vs Wavelength of sample 1. a-Si:H

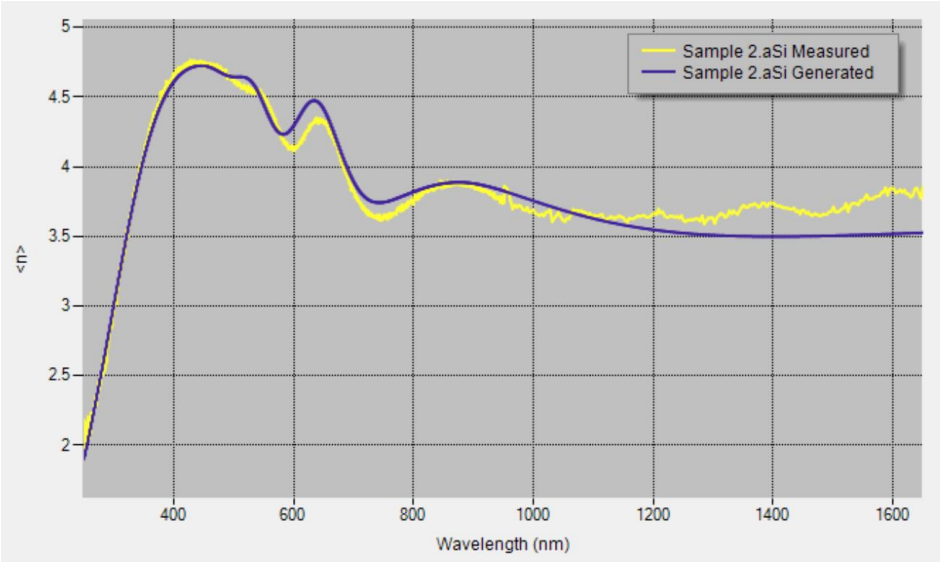

Figure 44. Index refraction vs Wavelength of sample 2. a-Si:H

The measurement of the surface roughness with the AFM demonstrates that the EMA (Effective Medium Approximation) layer is approximately of 3 nm, this value differs between the different samples. As it can be seen in Table 4, in all the silicon cases the EMA layer increases when increasing the deposition temperature. The following fifures represent the 3D surface roughness profile of the samples coated over silicon.

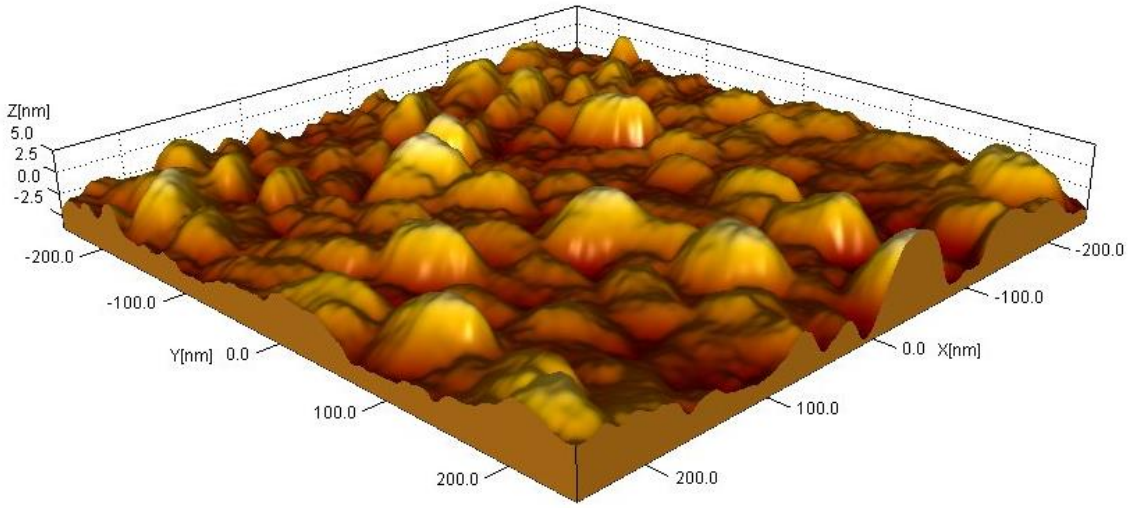

Figure 45. 3D image of the surface roughness sample 1. a-Si:H (T=100ºC and t=10 min)

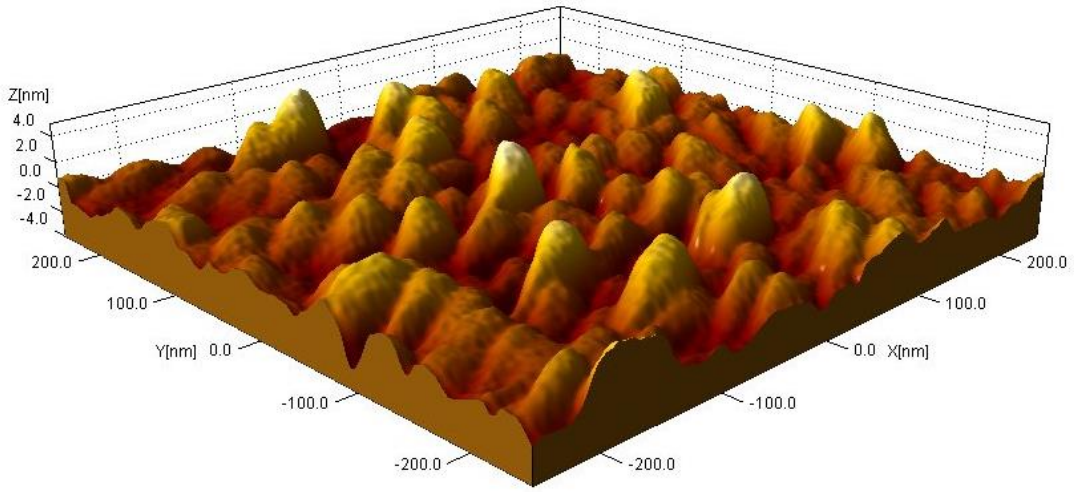

Figure 46. 3D image of the surface roughness sample 2. a-Si:H (T=100ºC and t=15 min)

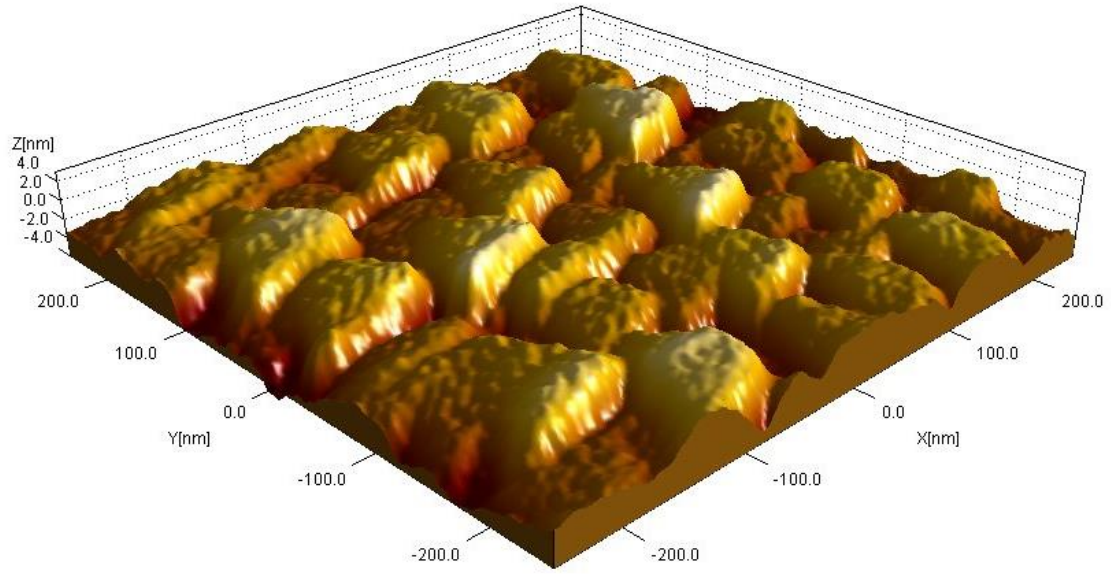

Figure 47. 3D image of the surface roughness sample 3. a-Si:H (T=150ºC and t=10 min)

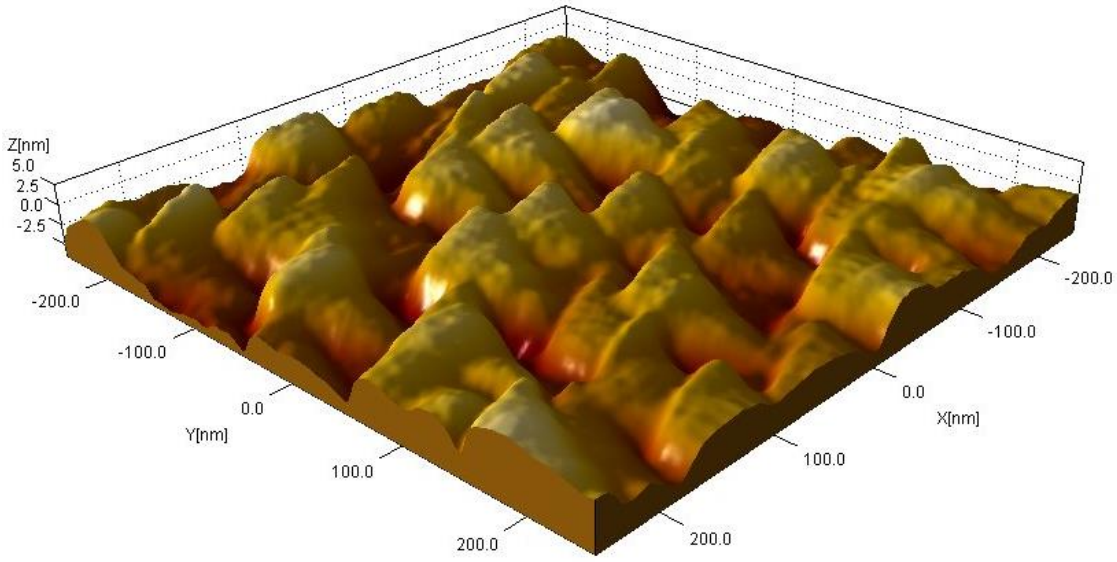

Figure 48. 3D image of the surface roughness sample 4. a-Si:H (T=150ºC and t=15 min)

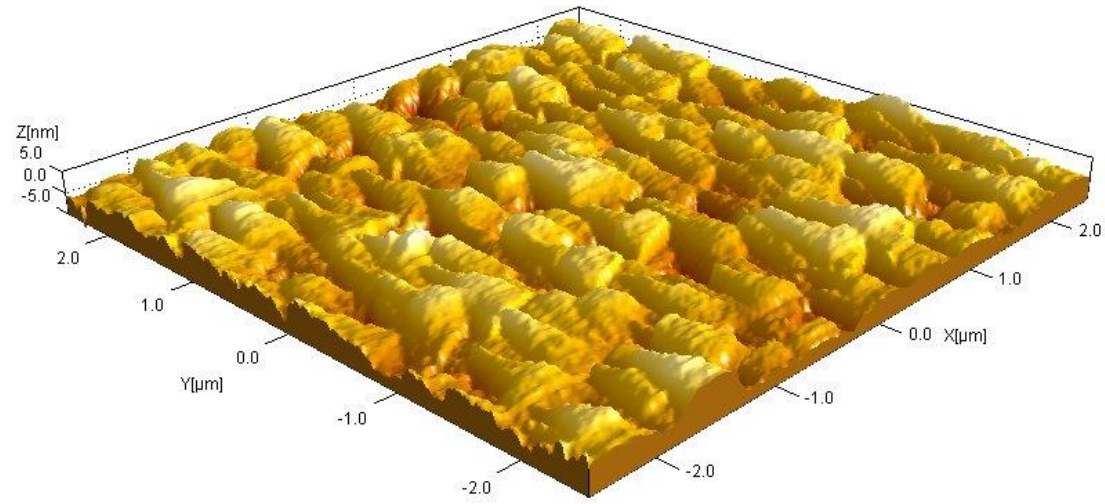

Figure 49. 3D image of the surface roughness sample 5. a-Si:H (T=100ºC and t=5 min)

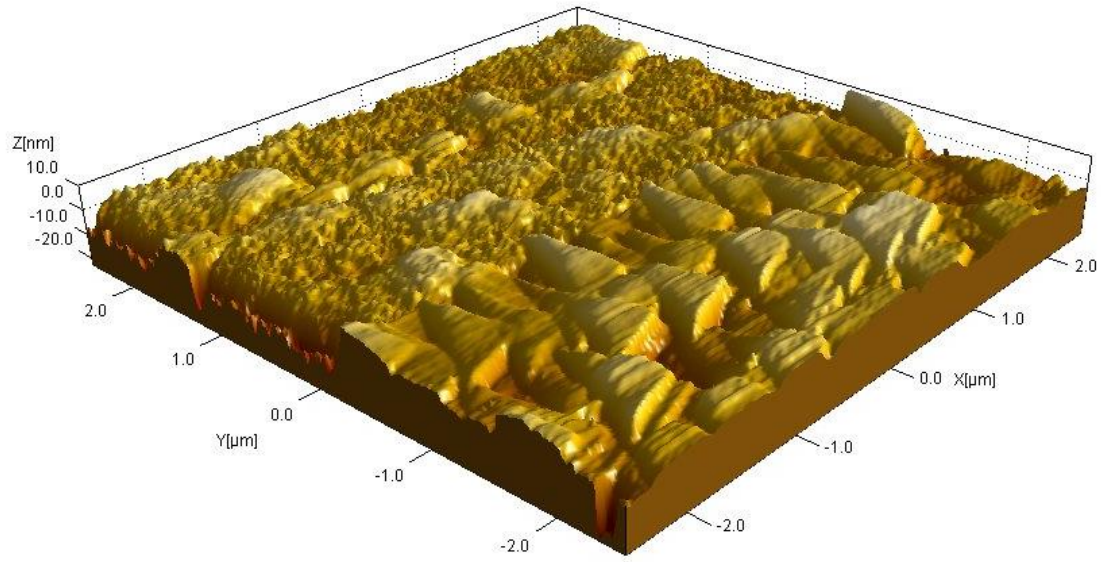

Figure 50. 3D image of the surface roughness sample 6. a-Si:H (T=150ºC and t=5 min)

The surface scan of sample 6. a-Si:H was not fully resolved, in the 3D image it can be notice that the scan gets blurry in the middle of the measurement, most probably due to particle pickup by the AFM cantilever. A possible explanation is that this occurred because the measurement was done one month after the deposition and some atmospheric dust got attached to the sample during handling.

With the AFM technique, it can also be seen that the amorphous silicon structure does not vary with time, and crystalline formations in the form of triangular shapes are observed. Figures 51 and 52 show the surface of the amorphous silicon coated over the silicon samples.

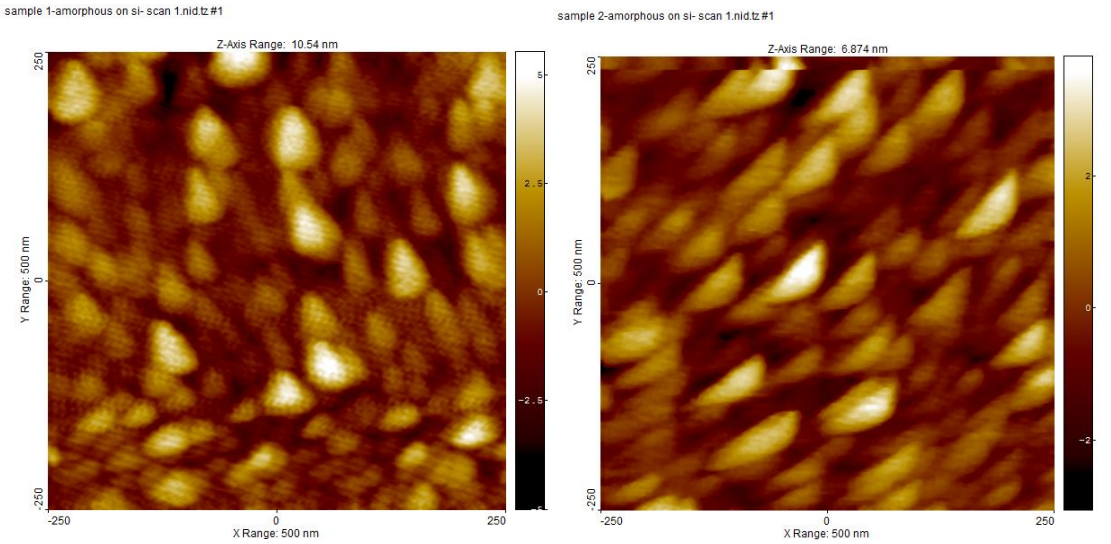

(a) (b)

Figure 51. Microstructure of the amorphous silicon samples coated over silicon at 100ºC (a) 10 mins (b) 15 mins

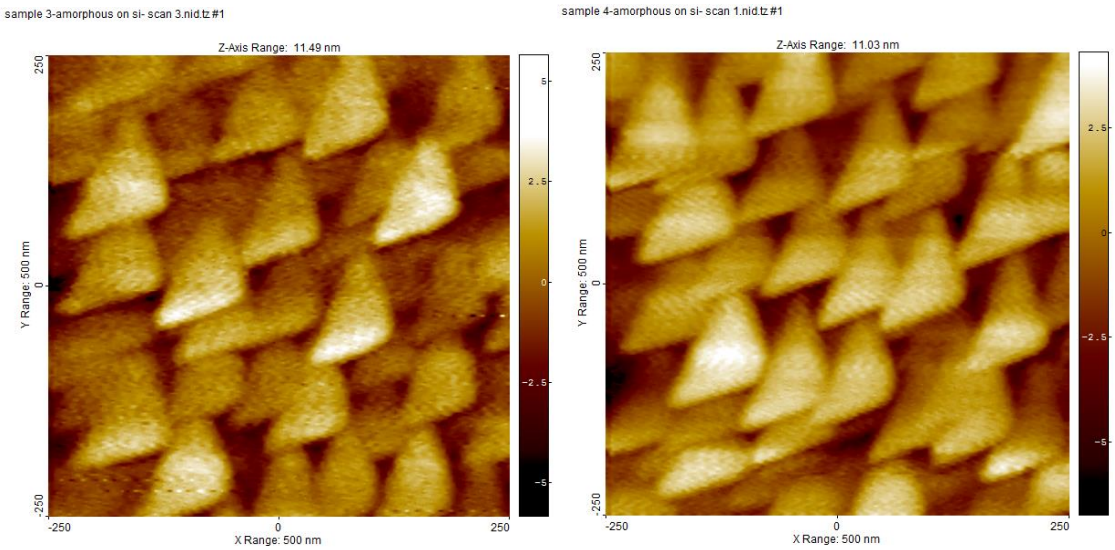

(a) (b)

Figure 52. Microstructure of the amorphous silicon samples coated over silicon at 150ºC (a) 10 mins (b) 15 mins

It can be seen that there is almost no difference between the samples made with the same deposition temperature but different deposition time. The only appreciable difference is the size of grain between the samples made at 100 ºC and 150 ºC, in this case the grain formed at 150 ºC is larger than the one formed at 100 ºC. This also proves what it's been said before, for the same deposition time, the structural order is higher.

A measurement of a larger area (3 µm) was made over the sample 4. a-Si:H in order to see the uniformity of the microstructure of the sample. From Figure 53 it can be seen that some amorphous silicon clusters can form at specific areas.

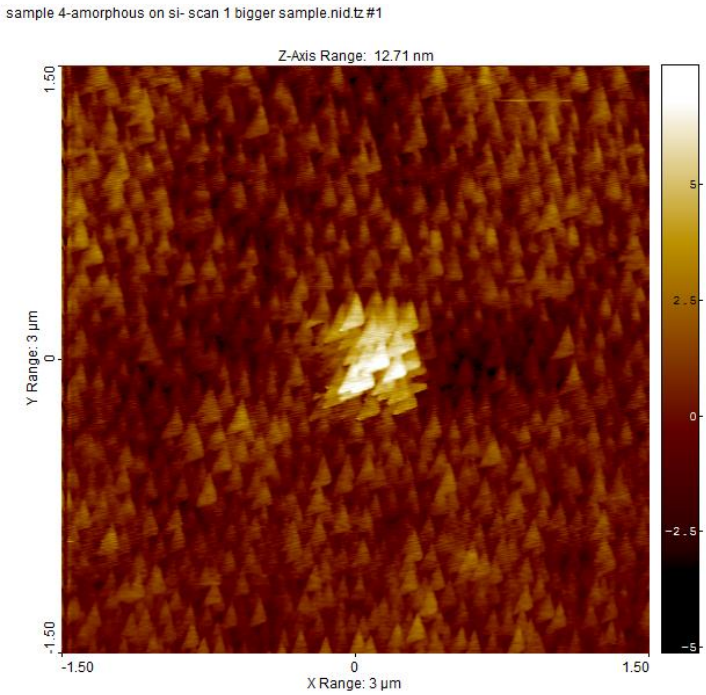

Figure 53. Microstructure of the amorphous silicon coated over silicon of sample 4. a-Si:H

2. Measurement of the hydrogen concentration

Once the infrared measurements of every substrate were done, the transmission of each sample was plotted, they are shown in Figure 54. The green curve represents the sample of pure silicon with an unpurged chamber where the absorption of the carbon dioxide can be appreciated. Carbon dioxide presents bending mode at the frequency of 650 cm^{-1}, asymmetric mode at 2340 cm^{-1}, and also present symmetric at 1330 cm^{-1} but

this mode does not produce any changes in the transmission because the infrared does not make any changes in the dipolar moment. It also generates interferences at the frequency between 3550-3750 cm^{-1} but the amorphous silicon does not have any appreciable absorption at this frequency so it was not of any particular concern [64]. For the graphic to be clearer the wavelengths represented are only from of 380 to 2500 cm-1 as there were no response in the rest of frequencies.

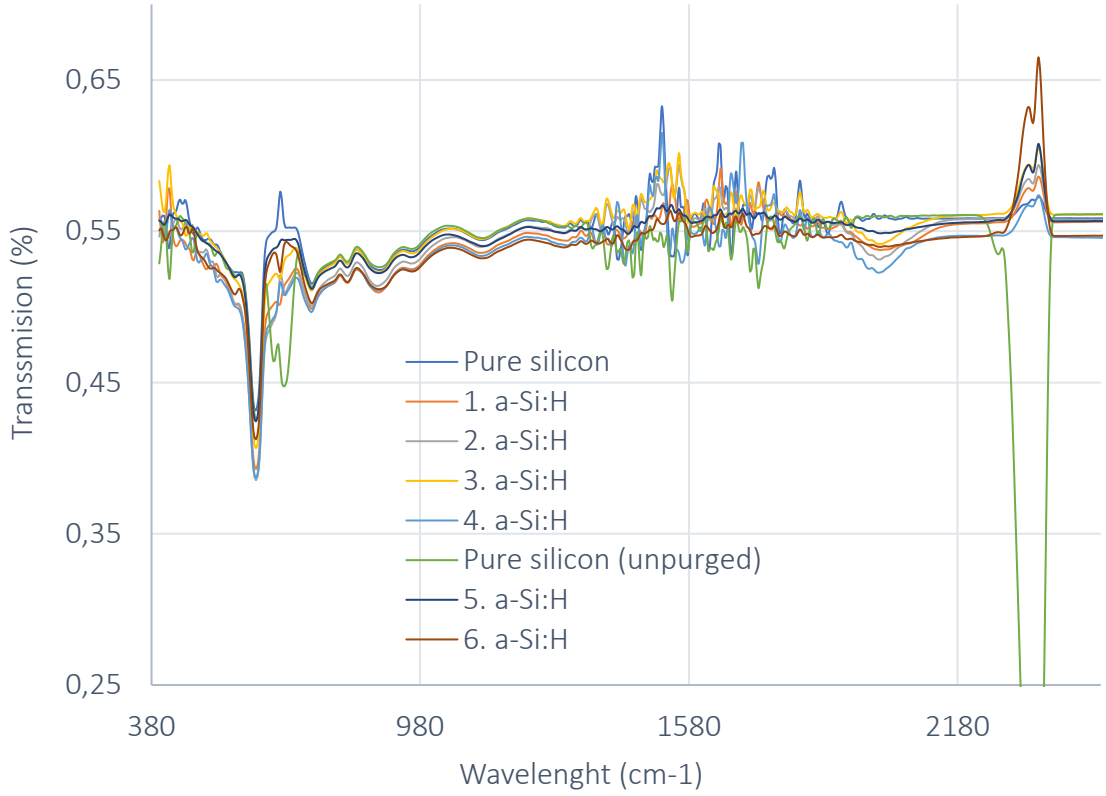

Figure 54. Wavelength vs Transmission

In order to convert the transmission signal into the absorption coefficients it has been used the Brodsky method [66], [67], we approximate the interference free transmission with:

$$T_{film} = \frac{(1-R)^2 * e^{-\alpha d}}{(1-R^2 * e^{-2\alpha d})}$$

Equation 10

Where:

- T_{film} is the transmission of the film (cm^{-1})

- R is an empirically determined interference multiple reflection loss
- α is the absorption coefficient (cm^{-1})
- d is the thickness of the amorphous silicon layer (cm).

R is transformed by setting T_{film}=To=0,54 and α=0, and the equation becomes:

$$T_{film} = \frac{4T_o^2 * e^{-\alpha d}}{(1+T_o)^2 - (1-T_o)^2 * e^{-2\alpha d}}$$

Equation 11

Where To the theoretical transmission of the silicon substrate and has a value of To=0,54 cm^{-1}. Now it can be solved for different values of α of the measured transmission. Equation 11 is only valid for a freely supported film.

The absorbance coefficient has been evaluated for the wavelength infrared spectra from 570 to 720 cm^{-1} using the Brodsky method. From literature it was known that crystalline silicon absorbs infrared at 615 cm^{-1}, which peak is also observed in Figure 55. This absorbance frequency peak can potentially present a deconvolution problem and unless the sample and the silicon reference are perfectly matched it would interfere with the hydrogenated amorphous silicon peak measurements [67].

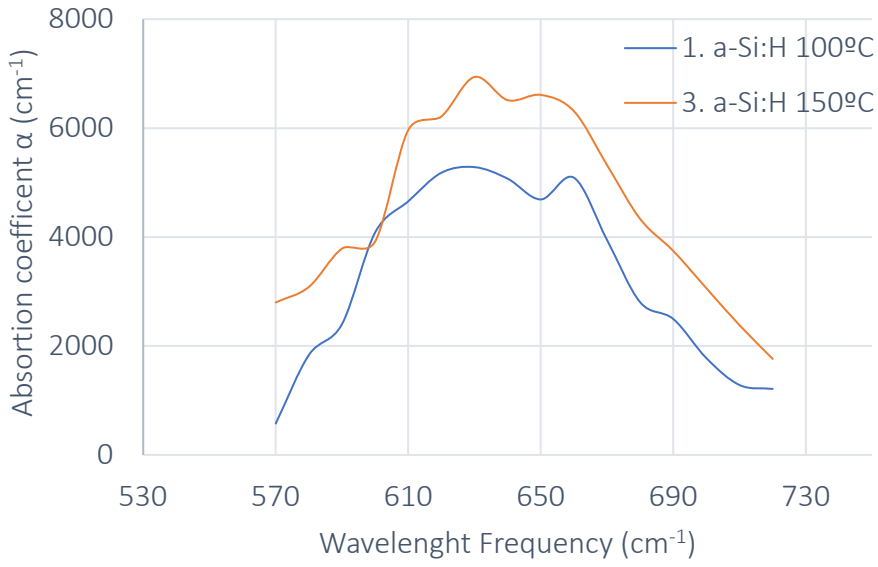

Figure 55. Infrared absorption spectra of a-Si:H films deposited at 100 and 150 ºC and 10 minutes in the wagging–rocking mode region.

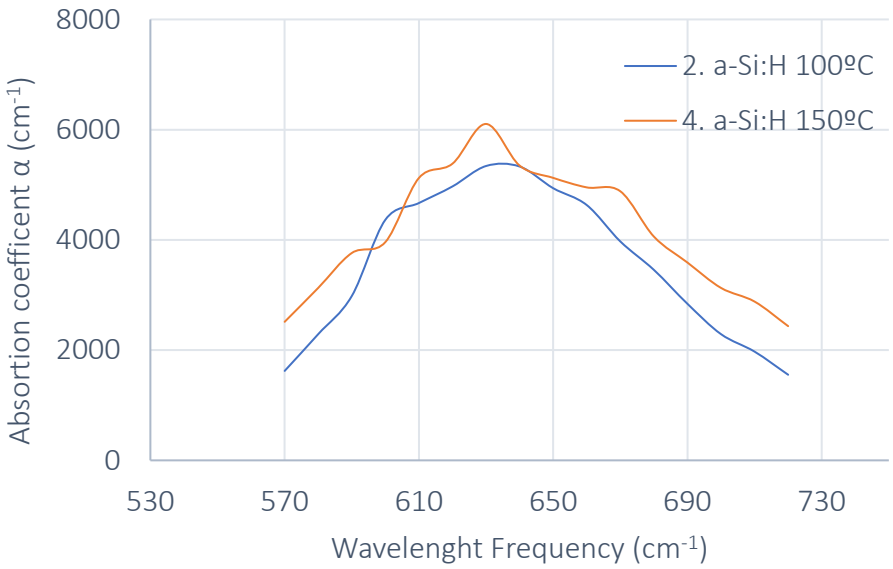

Figure 56. Infrared absorption spectra of a-Si:H films deposited at 100 and 150 ºC in the wagging–rocking mode region at 15 mins

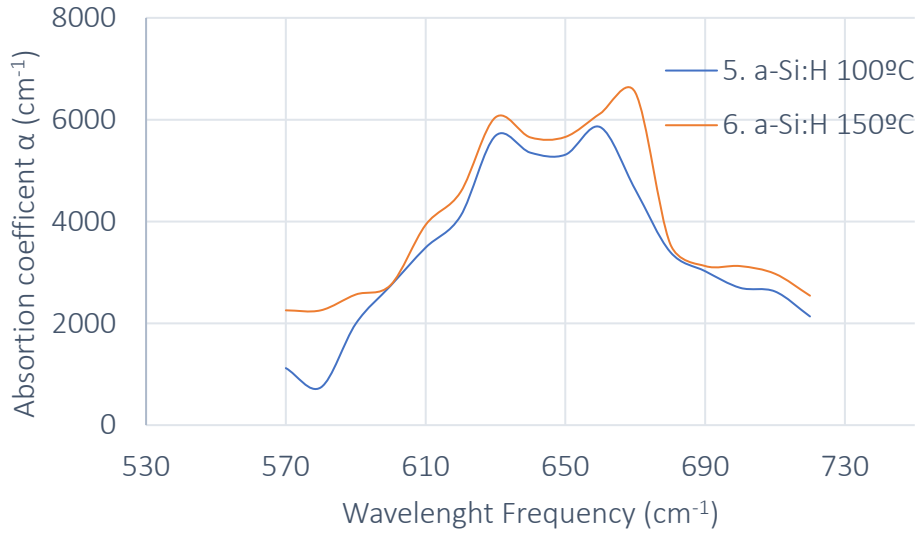

Figure 57. Infrared absorption spectra of a-Si:H films deposited at 100 and 150 ºC in the wagging–rocking mode region at 5 mins

In Figure 55, 56 and 57 the absorption coefficient vs. frequency are shown, where it can be observed that the absorption coefficient in the region of 570-720 cm^{-1} increases when increasing the process temperature. From different literature it is known that the concentration of total hydrogen in the films depends on the absorption concentration [68], [69] , but there are no studies that correlates the amount of bonded hydrogen to the absorption [70] . In the graphs (5, 10 and 15 min deposition time) it can be observed that the experiments behave the same way as the papers describe, where in all the cases

the absorption coefficient increases with the temperature. It is known that an increase of the temperature during the deposition of the film leads to a decrease in the content of hydrogen due to the decreased of the clustered hydrogen, and also to a variation in the silicon-hydrogen vibrational modes in the amorphous silicon thin films.

The next mode found in the literature review [68] is the bending and scissoring mode in 840, 850 and 880 cm^{-1}. In this experiment none of these peaks have been found in the FTIR measurements, these peaks are associated with the dihydrides (SiH_2) scissoring mode and the polysilanes ($(SiH_2)_n$) which are usually undesired in good quality coatings.

The study of the hydrogen bonding configuration has led to a new peak, it is located at 2000 cm^{-1}, this peak corresponds to the isolated monohydrides (SiH) in the bulk, they are created by the saturation of the dangling bonds during the deposition of the film. From literature review [68] it is known that there must be another peak around 2100 cm^{-1}, this peak corresponds to the polyhydride silicon or the clustered monohydride groups on the inner surface of microvoids. In the experiments carried out in the laboratory this peak in not seen, this means that the bonds formed between the silicon and the hydrogen are monohydrids, so it means that the layers obtained are of high quality and have good potential for future thin solar cells.

The other method used to see the amount of hydrogenation that the coatings had was the measurement of the contact angle. In this case the results were not conclusive. In Table 5 it can be seen the value of the different contact angles for pure silicon and the four first samples made over silicon. Once we knew this method was not conclusive we did not perform it in the three last samples deposited over silicon.

Sample nº	Left angle	Right angle
1. a-Si:H	122,6	132,6
2. a-Si:H	122,7	114,9
3. a-Si:H	126,1	123,4
4. a-Si:H	117,3	129,6
8. Si	142,1	140,7

Table 5. Contact angles measured for different samples

As it can be seen, the measurement does not conclude the amount of hydrogenation in the coating, the only appreciable difference between the samples is between the pure silicon and the amorphous silicon coating. As it expected the contact angles on the water drop is larger in the double side polished silicon than in the amorphous silicon, the dangling bonds of the unpassivated pure silicon have attracted more water than the hydrogenated amorphous silicon. In Figure 58 and 59 the different pictures of the water drop and the contact angles of each sample can be seen.

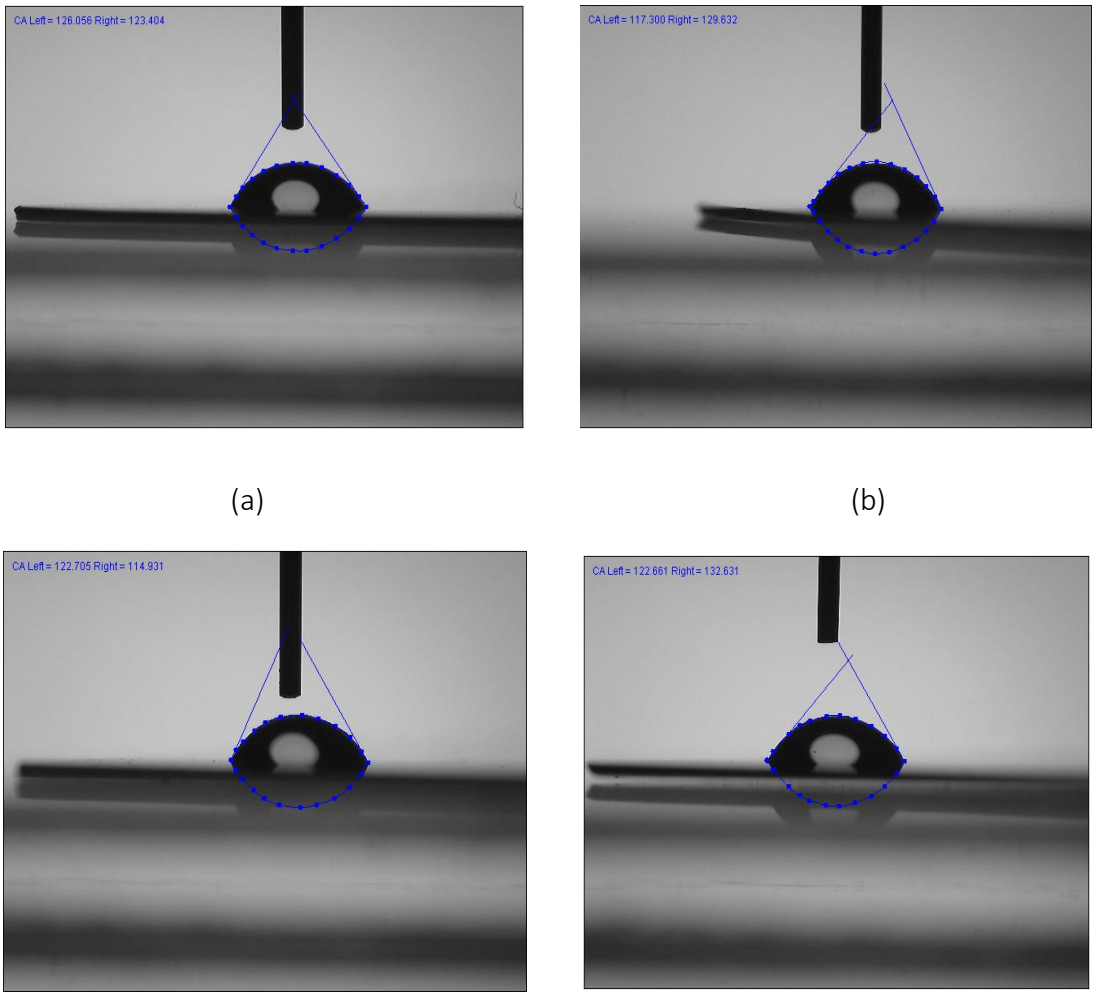

Figure 58. Contact angle for the samples made a 100 ºC (a) 1. a-Si:H (b) 2. a-Si:H (c) 3. a-Si:H (d) 4. a-Si:H

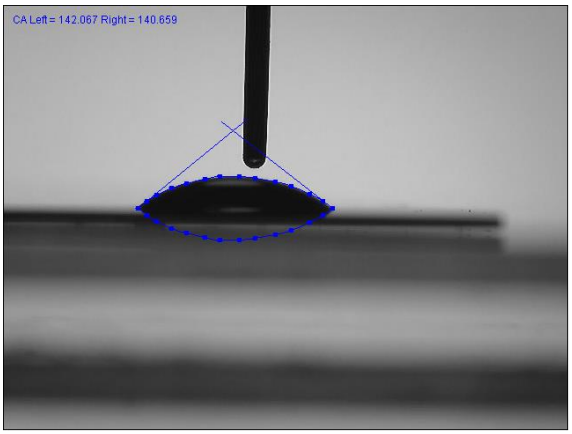

Figure 59. Contact angle of the double polished silicon

CHAPTER 5. CONCLUSIONS AND FURTHER WORK

Amorphous silicon thin films were produced by PECVD at different temperatures and deposition times in order to study the effect of these parameters on the thickness, crystallinity and the hydrogenation. A complement of techniques was used to measure the produced films, including transmission FTIR, Spectroscopic ellipsometry, Contact angle measurement and atomic force microscopy.

It can be concluded that an increase in the deposition time or deposition temperature leads to a thicker a-Si:H coating. From the measurements of the ellipsometry, it was also concluded that the index refraction is higher for the samples made at longer times for the same deposition temperature. The results obtained about the band gap were not conclusive and the samples reacted differently. This is probably because the values of amplitude reduction ratio (ψ) and phase difference (Δ) were not well fitted with the models used. So, in order to obtain better fittings in the ellipsometry, different models can be tried in the future over the silicon samples.

From the measurement of the FTIR, it was found the different vibrational molecules modes, these indicate the presence of hydrogen in the coating. At higher deposition temperatures the absorbance coefficient is higher, this means that the total amount of hydrogen in the film is lower than the films fabricated at lower temperatures. It was also shown that with a well determined parameter set and temporally controlled processing, good quality films which are free from dihydrides and their complexes can be produced. This paves the way for the production of highly efficient fully functioning thin film solar cells with potentially limited light induced degradation.

The contact angle measurements concluded that this method is not a good for the measurement of the content of hydrogen in the film.

Last, the AFM proved that the deposition time does not affect the microstructure of the samples made at the same temperature. But comparing the samples made at different temperature it was seen that the samples made at higher temperatures have a larger size of grain.

Grazing Incidence X-ray diffraction (GIXRD) can be used to study the crystallinity of layers so it can be used in following projects to measure the microcrystallinity of the silicon samples.

Measurement of the photoluminescence and electron life time at different light exposure times can be done over the sampleto determine the applicability of the coatings for efficient photovoltaics.

In order to produce a functioning cell, the deposition process will need to be repeated with the introduction of dopant gases such as Diborane (B_2H_6) and Phosphine (PH_3). This would produce an effective P/N junction that yields a working thin film PV cell with controllable microcrystallnity.

References

References

[1] J. Carabe and J. Gandia, "Thin-film-silicon solar cells," *Opto-Electronics Review,* vol. 12, *(1),* pp. 1-6, 2004.

[2] R. A. Millikan, "A direct photoelectric determination of Planck's" h"," *Physical Review,* vol. 7, *(3),* pp. 355, 1916.

[3] (). *Band Gap [oline]* *http://chemical-quantum-images.blogspot.com.mt/2013/04/band-gaps.html* *[Last visited: 09/05/2018]*.

[4] (). *Direct and Indirect Band Gap* *https://www.doitpoms.ac.uk/tlplib/semiconductors/direct.php* *[Las visited 27/05/2018]*.

[5] (). *Minority carrier lifetime* *https://www.tf.unikiel.de/matwis/amat/semi_en/kap_2/backbone/r2_2_3.html* *]Last isited 22/5/2018]*.

[6] S. Rein, "Lifetime spectroscopy: a method of defect characterization in silicon for photovoltaic applications. 2005," *Berlin: Springer,* vol. 489, pp. 188, .

[7] B. Van Zeghbroeck, "Principles of semiconductor devices," *Colarado University,* 2004.

[8] V. K. Khanna, "Carrier lifetimes and recombination–generation mechanisms in semiconductor device physics," *European Journal of Physics,* vol. 25, *(2),* pp. 221, 2004.

[9] K. Fukutani *et al*, "Band gap tuning of a-Si:H from 1.55 eV to 2.10 eV by intentionally promoting structural relaxation," *Journal of Non-Crystalline Solids,* vol. 227-230, pp. 63-67, 1998. . DOI: https://doi.org/10.1016/S0022-3093(98)00022-2.

[10] (). *P-N Barrier High [online]* *http://slideplayer.com/slide/4784313/#* *[Las visited: 09/05/2018]*.

[11] D. Carlson and C. Wronski, "Topics in Applied Physics: Amorphous Semiconductors: Amorphous Silicon Solar Cells (1985)," .

[12] (). *Parts and material of a solar panel* *https://www.cleanenergyauthority.com/solar-energy-resources/components-of-a-residential-solar-electric-system* *[Last visited 30/6/2018]*.

[13] (). *Czochralski Crystal growth* *http://www.galaxywafer.com/galaxy/technology/crystal-growth/* *[Last visited 12/4/2018]*.

[14] G. Fisher, M. R. Seacrist and R. W. Standley, "Silicon crystal growth and wafer technologies," *Proc IEEE,* vol. 100, *(Special Centennial Issue),* pp. 1454-1474, 2012.

[15] R. W. Miles, "Photovoltaic solar cells: Choice of materials and production methods," *Vacuum,* vol. 80, *(10),* pp. 1090-1097, 2006. . DOI: https://doi.org/10.1016/j.vacuum.2006.01.006.

[16] A. Gordijn, *Microcrystalline Silicon for Thin-Film Solar Cells.* Utrecht University, 2005.

[17] G. Conibeer, "Third-generation photovoltaics," *Materials Today,* vol. 10, *(11),* pp. 42-50, 2007. . DOI: https://doi.org/10.1016/S1369-7021(07)70278-X.

[18] D. König *et al*, "Hot carrier solar cells: Principles, materials and design," *Physica E: Low-Dimensional Systems and Nanostructures,* vol. 42, *(10),* pp. 2862-2866, 2010. . DOI: https://doi.org/10.1016/j.physe.2009.12.032.

[19] J. - Yan and B. R. - Saunders, "- Third-generation solar cells: a review and comparison of polymer:fullerene, hybrid polymer and perovskite solar cells," - *RSC Adv., (- 82),* pp. - 43286, .

[20] A. C. Mayer *et al*, "Polymer-based solar cells," *Materials Today,* vol. 10, *(11),* pp. 28-33, 2007. . DOI: https://doi.org/10.1016/S1369-7021(07)70276-6.

[21] Z. He *et al*, "Single-junction polymer solar cells with high efficiency and photovoltage," *Nature Photonics,* vol. 9, *(3),* pp. 174, 2015.

[22] A. Martí and A. Luque, *Next Generation Photovoltaics: High Efficiency through Full Spectrum Utilization.* CRC Press, 2003.

[23] N. V. Yastrebova, "High-efficiency multi-junction solar cells: Current status and future potential," *Solar Energy,* 2007.

[24] M. Stuckelberger *et al*, "Review: Progress in solar cells from hydrogenated amorphous silicon," *Renewable and Sustainable Energy Reviews,* vol. 76, pp. 1497-1523, 2017. . DOI: https://doi.org/10.1016/j.rser.2016.11.190.

[25] M. A. Green, *Third Generation Photovoltaics: Advanced Solar Energy Conversion.* Springer Science & Business Media, 2006*12*.

[26] F. Dimroth *et al*, "Four-junction wafer-bonded concentrator solar cells," *IEEE Journal of Photovoltaics,* vol. 6, *(1),* pp. 343-349, 2016.

[27] C. Shin *et al*, "Optimization of intrinsic hydrogenated amorphous silicon deposited by very high-frequency plasma-enhanced chemical vapor deposition using the relationship between Urbach energy and silane depletion fraction for solar cell application," *Thin Solid Films,* vol. 547, pp. 256-262, 2013. . DOI: https://doi.org/10.1016/j.tsf.2013.01.023.

[28] S. O. Kasap, *Principles of Electronic Materials and Devices.* McGraw-Hill New York, 2006*2*.

[29] A. G. Aberle, "Thin-film solar cells," *Thin Solid Films,* vol. 517, *(17),* pp. 4706-4710, 2009. . DOI: https://doi.org/10.1016/j.tsf.2009.03.056.

[30] S. Wagner, D. E. Carlson and H. M. Branz, "Amorphous and microcrystalline silicon solar cells," *Proceedings of the Electrochemical Society (Editado Por VK Kapur, RD McConnell, D.Carlson, GP Ceasar Y 266 Bibliografía A.Rohatgi),* vol. 99, pp. 219, 1999.

[31] B. Strahm *et al*, "Plasma silane concentration as a determining factor for the transition from amorphous to microcrystalline silicon in SiH4/H2 discharges," *Plasma Sources Sci. Technol.,* vol. 16, *(1),* pp. 80, 2006.

[32] R. W. Collins *et al*, "Evolution of microstructure and phase in amorphous, protocrystalline, and microcrystalline silicon studied by real time spectroscopic ellipsometry," *Solar Energy Materials and Solar Cells,* vol. 78, *(1),* pp. 143-180, 2003. . DOI: https://doi.org/10.1016/S0927-0248(02)00436-1.

[33] Sculati-Meillaud, Fanny, Shah, Arvind. Dir., "Microcrystalline Silicon Solar Cells theory, Diagnosis and Stability." , Université de Neuchâtel, 2006.

[34] (). *Silicon based multijunction devices [Online] https://www.helmholtz-berlin.de/projects/pvcomb/forschen/pof-research-activities/lit11_en.html [Last visited: 09/05/2018]*.

[35] A. Kołodziej, "Staebler-Wronski effect in amorphous silicon and its alloys," *Opto-Electronics Review,* vol. 12, *(1),* pp. 21-32, 2004.

[36] M. Du and S. B. Zhang, "Topological defects and the Staebler-Wronski effect in hydrogenated amorphous silicon," *Appl. Phys. Lett.,* vol. 87, *(19),* 2005.

[37] Q. H. Fan *et al*, "High efficiency silicon–germanium thin film solar cells using graded absorber layer," *Solar Energy Materials and Solar Cells,* vol. 94, *(7),* pp. 1300-1302, 2010. . DOI: https://doi.org/10.1016/j.solmat.2010.03.006.

[38] T. Mishima *et al*, "Development status of high-efficiency HIT solar cells," *Solar Energy Materials and Solar Cells,* vol. 95, *(1),* pp. 18-21, 2011. . DOI: https://doi.org/10.1016/j.solmat.2010.04.030.

[39] A. ur Rehman and S. H. Lee, "Advancements in n-type base crystalline silicon solar cells and their emergence in the photovoltaic industry," *ScientificWorldJournal,* vol. 2013, pp. 470347, Dec 29, 2013.

[40] M. Taguchi *et al*, "24.7% record efficiency HIT solar cell on thin silicon wafer," *IEEE Journal of Photovoltaics,* vol. 4, *(1),* pp. 96-99, 2014.

[41] A. C. Jones and M. L. Hitchman, "Overview of chemical vapour deposition," *Chemical Vapour Deposition: Precursors, Processes and Applications,* pp. 1-36, 2008.

[42] J. N. Pring and W. Fielding, "CLXXI.—The preparation at high temperatures of some refractory metals from their chlorides," *Journal of the Chemical Society, Transactions,* vol. 95, pp. 1497-1506, 1909.

[43] R. Hölbling, "Über die Herstellung und einige Eigenschaften von reinem metallischen Silicium," *Angewandte Chemie,* vol. 40, *(23),* pp. 655-659, 1927.

[44] W. G. Van Sark, "Methods of deposition of hydrogenated amorphous silicon for device applications," in *Handbook of Thin Films*Anonymous Elsevier, 2002, pp. 1-102.

[45] R. d'Agostino *et al*, *Advanced Plasma Technology.* John Wiley & Sons, 2008.

[46] J. Perrin, "J. Perrin, O. Leroy, and MC Bordage, Contrib. Plasma Phys. 36, 3 (1996)." *Contrib.Plasma Phys.,* vol. 36, pp. 3, 1996.

[47] E. Austin and F. Lampe, "Rate constants for the reactions of hydrogen atoms with some silanes and germanes," *J. Phys. Chem.,* vol. 81, *(12),* pp. 1134-1138, 1977.

[48] T. Pollock *et al*, "Photochemistry of silicon compounds. IV. Mercury photosensitization of disilane," *J. Am. Chem. Soc.,* vol. 95, *(4),* pp. 1017-1024, 1973.

[49] N. Itabashi *et al*, "Diffusion coefficient and reaction rate constant of the SiH3 radical in silane plasma," *Japanese Journal of Applied Physics,* vol. 28, *(2A),* pp. L325, 1989.

[50] A. Hickman, "Approximate scaling formula for ion–ion mutual neutralization rates," *J. Chem. Phys.,* vol. 70, *(11),* pp. 4872-4878, 1979.

[51] S. Xiao, S. Xu and K. Ostrikov, "Low-temperature plasma processing for Si photovoltaics," *Materials Science and Engineering: R: Reports,* vol. 78, pp. 1-29, 2014.

[52] H. Fujiwara, *Spectroscopic Ellipsometry: Principles and Applications.* John Wiley & Sons, 2007.

[53] T. Tsuru, "Ellipsometry," in *Compendium of Surface and Interface Analysis*Anonymous Springer, 2018, pp. 155-164.

[54] W. Perkins, "Fourier transform-infrared spectroscopy: Part l. Instrumentation," *J. Chem. Educ.,* vol. 63, *(1),* pp. A5, 1986.

[55] V. Saptari, *Fourier Transform Spectroscopy Instrumentation Engineering.* SPIE Optical Engineering Press, 2003.

[56] F. Lazzarino *et al*, "Ultra-low k dielectric and plasma damage control for advanced technology nodes (10-nm and below)," 2013.

[57] (). *FTIF Instrumentation [Online]* *file:///C:/Users/lidia/Downloads/FTIR_Instrumentation_short-1.pdf [Last visited: 10/05/2018]*.

[58] C. Della Volpe *et al*, "An experimental procedure to obtain the equilibrium contact angle from the Wilhelmy method," *Oil & Gas Science and Technology,* vol. 56, *(1),* pp. 9-22, 2001.

[59] R. Förch, H. Schönherr and A. T. A. Jenkins, *Surface Design: Applications in Bioscience and Nanotechnology.* John Wiley & Sons, 2009.

[60] F. M. Fowkes, *Contact Angle, Wettability, and Adhesion.* ACS Publications, 1964.

[61] F. Hejda, P. Solar and J. Kousal, "Surface free energy determination by contact angle measurements–a comparison of various approaches," in *Wds,* 2010, pp. 25-30.

[62] E. Canetta and A. K. Adya, "Nano-imaging and its applications to biomedicine," in *International Conference on Image Analysis and Processing,* 2011, pp. 423-432.

[63] N. Korner *et al*, "Hydrogen plasma chemical cleaning of metallic substrates and silicon wafers," *Surface and Coatings Technology,* vol. 76-77, pp. 731-737, 1995. . DOI: https://doi.org/10.1016/0257-8972(95)02503-0.

[64] (). *NIST Data Base, National Istitute of Standars and Technology [Online] https://webbook.nist.gov/cgi/cbook.cgi?ID=C124389&Type=IR-SPEC&Index=1#IR-SPEC [Last visited: 14/05/2018]*.

[65] Y. Abdulraheem *et al*, "Optical bandgap of ultra-thin amorphous silicon films deposited on crystalline silicon by PECVD," *AIP Advances,* vol. 4, *(5),* pp. 057122, 2014.

[66] M. Brodsky, M. Cardona and J. Cuomo, "Infrared and Raman spectra of the silicon-hydrogen bonds in amorphous silicon prepared by glow discharge and sputtering," *Physical Review B,* vol. 16, *(8),* pp. 3556, 1977.

[67] A. Langford, M. Fleet and A. Mahan, "Correction for multiple reflections in infrared spectra of amorphous silicon," *Solar Cells,* vol. 27, *(1-4),* pp. 373-383, 1989.

[68] P. Danesh *et al*, "Hydrogen bonding and structural order in hydrogenated amorphous silicon prepared with hydrogen-diluted silane," *J. Phys. D,* vol. 37, *(2),* pp. 249, 2003.

[69] M. Wu *et al*, "Hydrogen bonding in hydrogenated amorphous silicon thin films prepared at different precursor gas temperatures with undiluted silane," *Science China Technological Sciences,* vol. 54, *(9),* pp. 2310, 2011.

[70] A. Langford *et al*, "Infrared absorption strength and hydrogen content of hydrogenated amorphous silicon," *Physical Review B,* vol. 45, *(23),* pp. 13367, 1992.

Appendix A

In this appendix a summary of all the photos of the samples are shown. As well as the graphs obtained in the ellipsometry for the samples coated over silicon, of the reflection phase difference (Δ), amplitude reduction ratio (ψ), and the refraction index (n) of the samples that have not included in chapter 4.

- Sample 1. a-Si:H

Amplitude reduction ratio (ψ) vs Wavelength

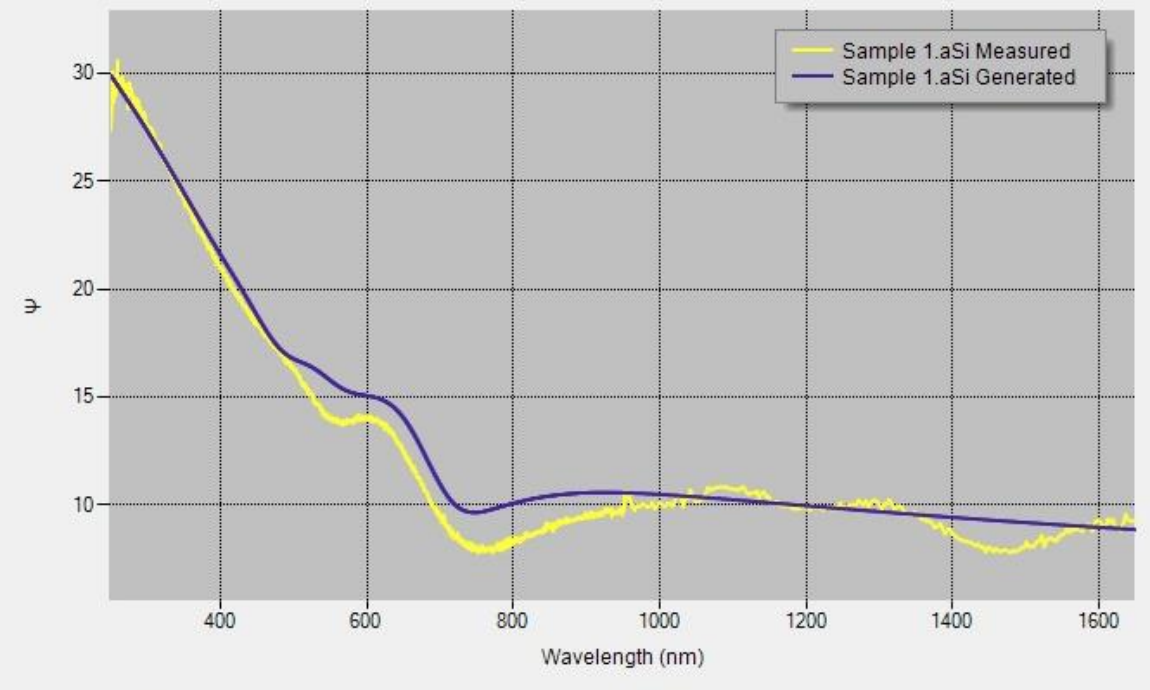

Phase difference (Δ) vs Wavelength

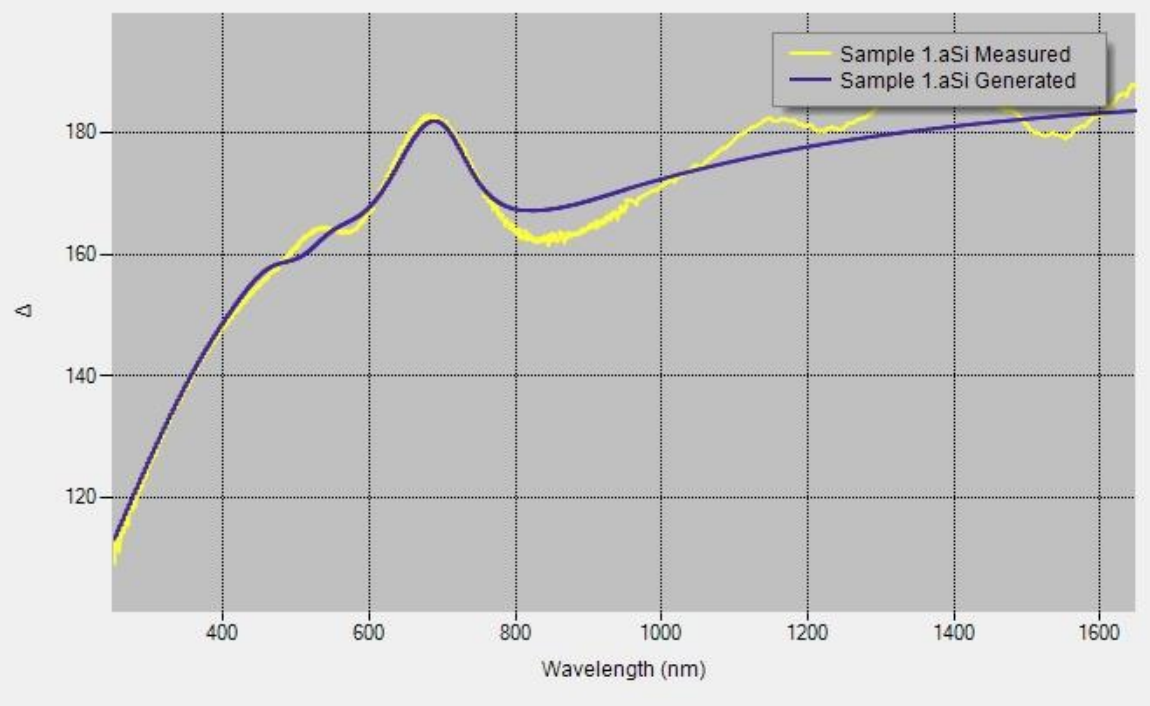

- Sample 2. a-Si:H

Amplitude reduction ratio (ψ) vs Wavelength

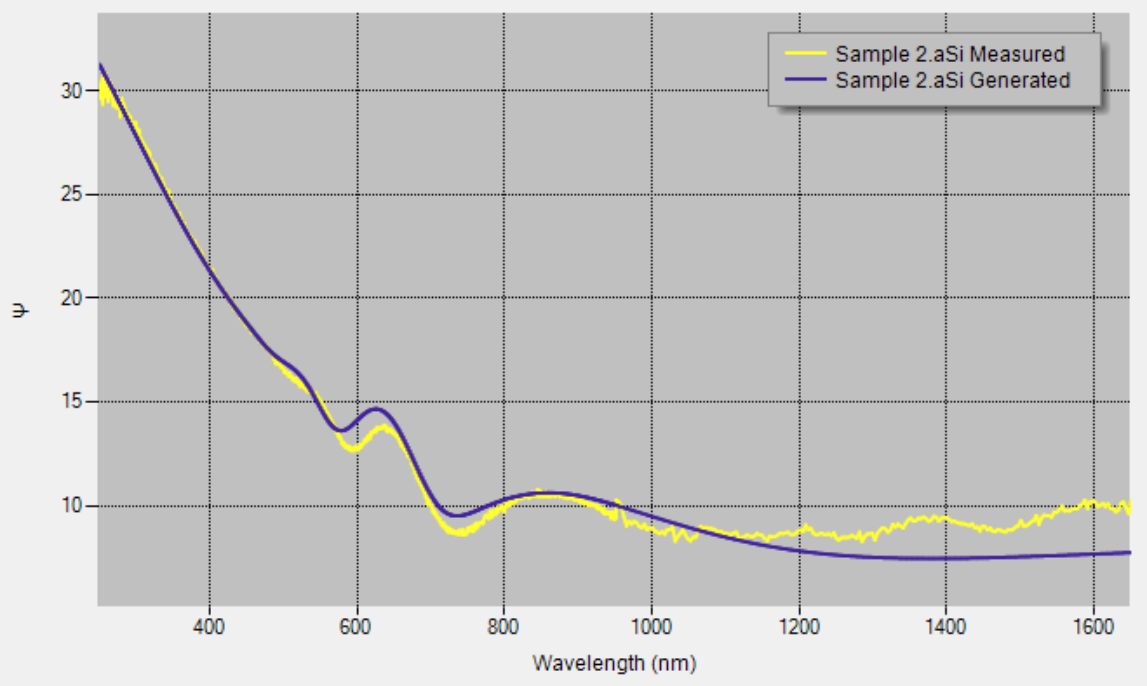

Phase difference (Δ) vs Wavelength

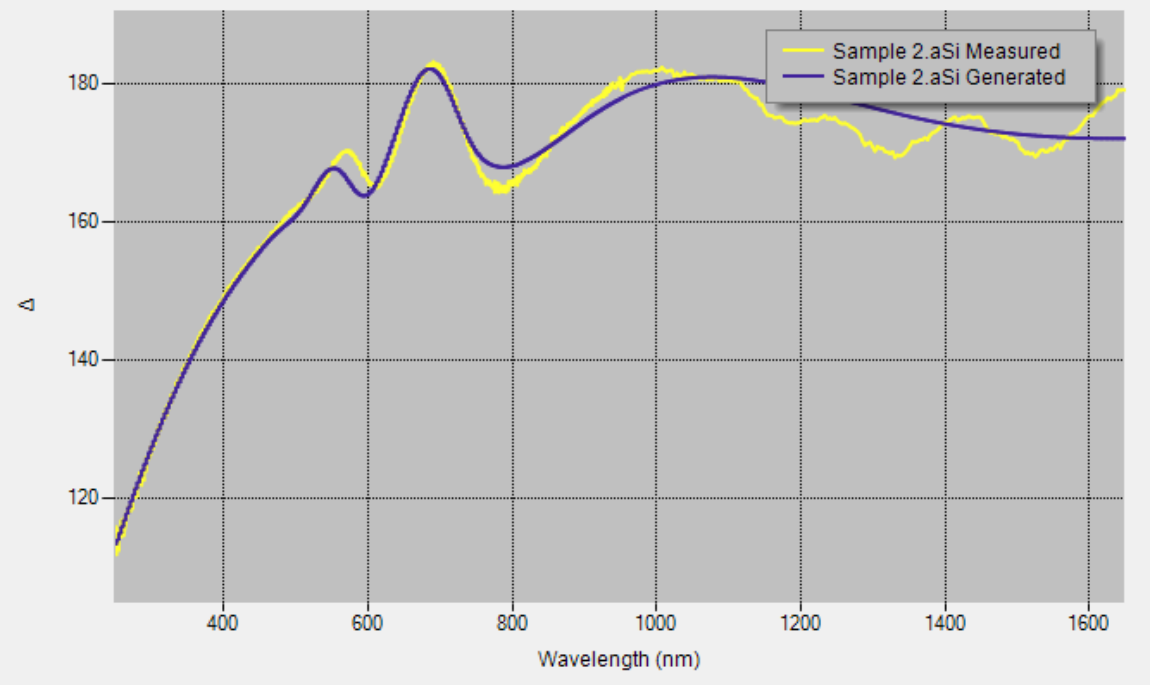

- Sample 3. a-Si:H

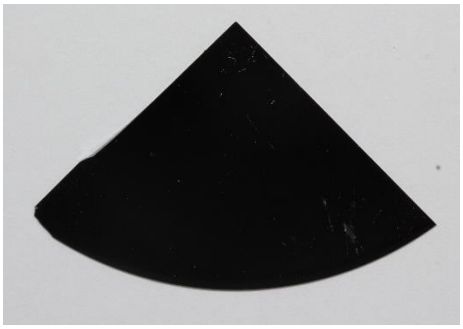

Amplitude reduction ratio (ψ) vs Wavelength

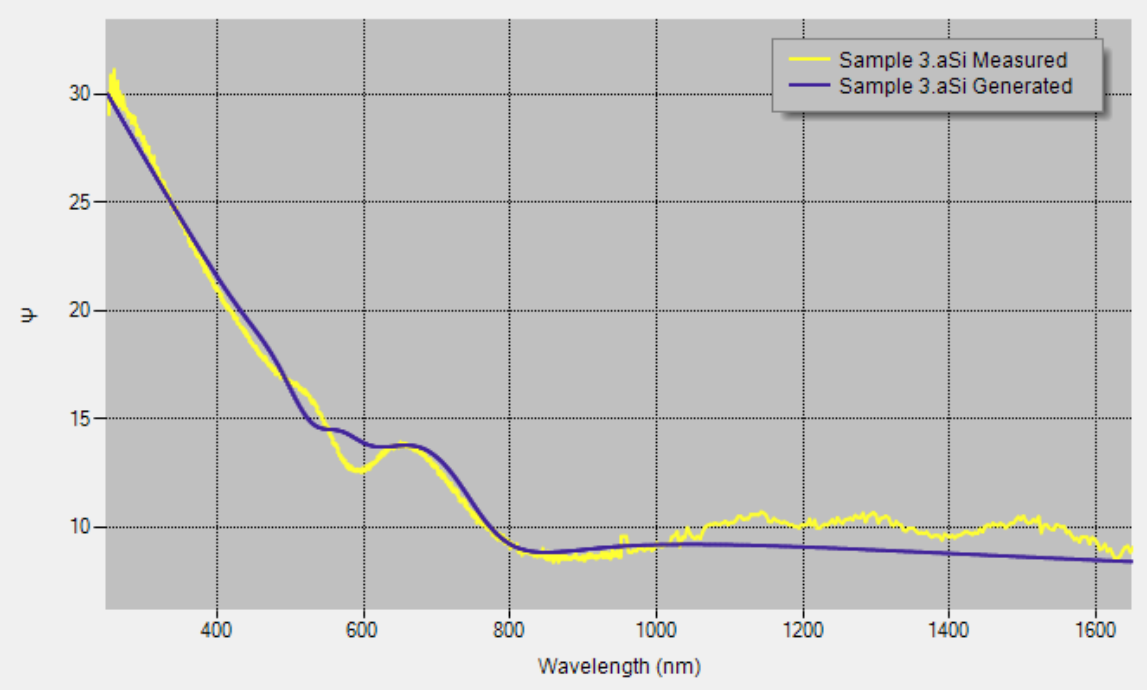

Phase difference (Δ) vs Wavelength

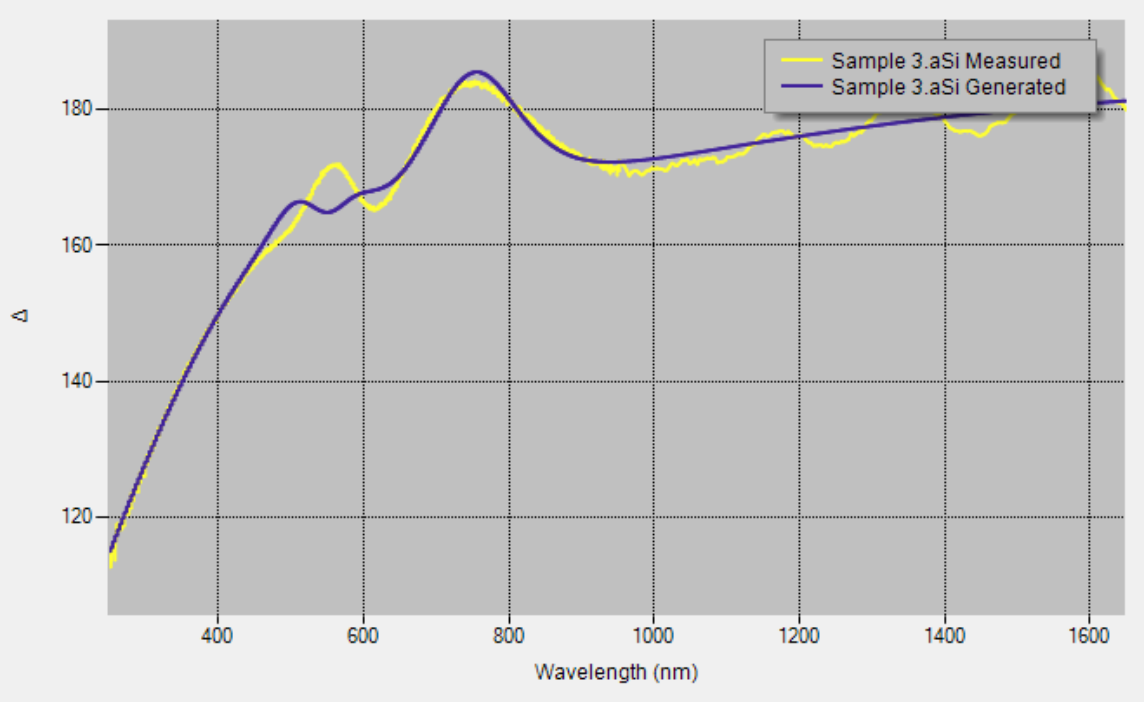

Refraction index (n) vs Wavelength

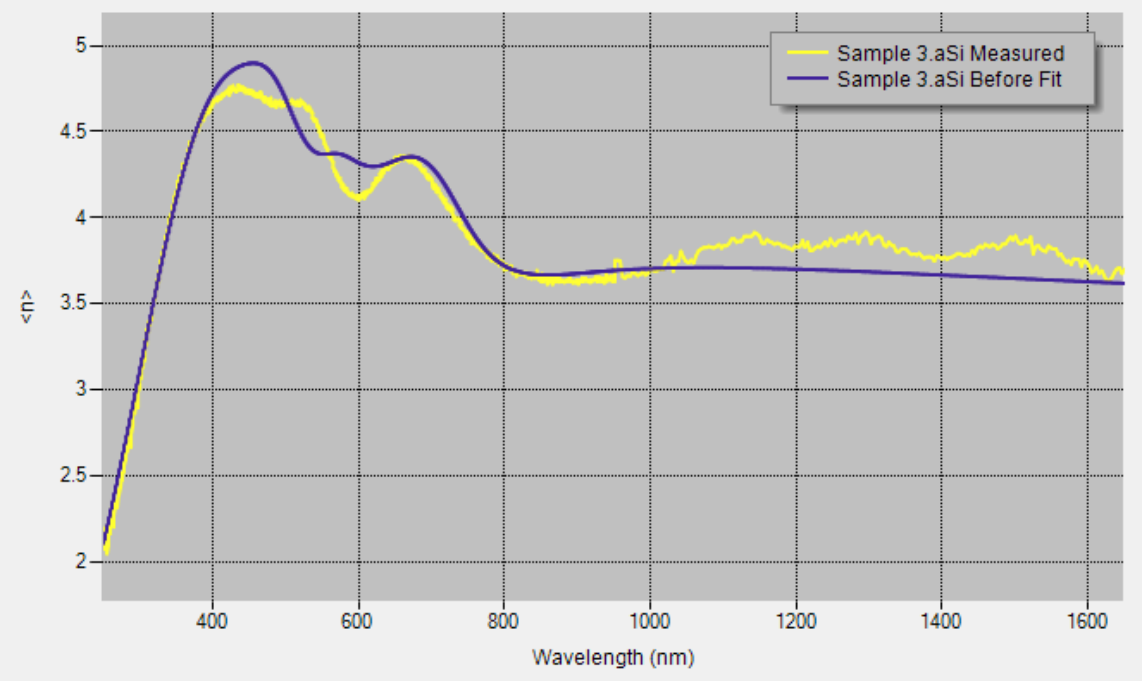

- Sample 4. a-Si:H

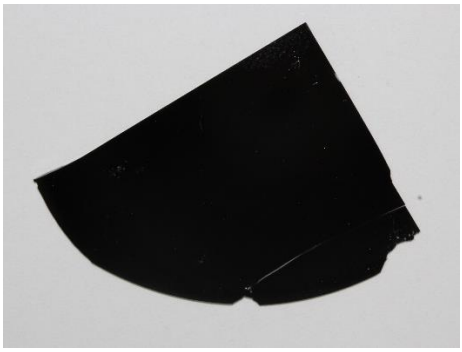

Amplitude reduction ratio (ψ) vs Wavelength

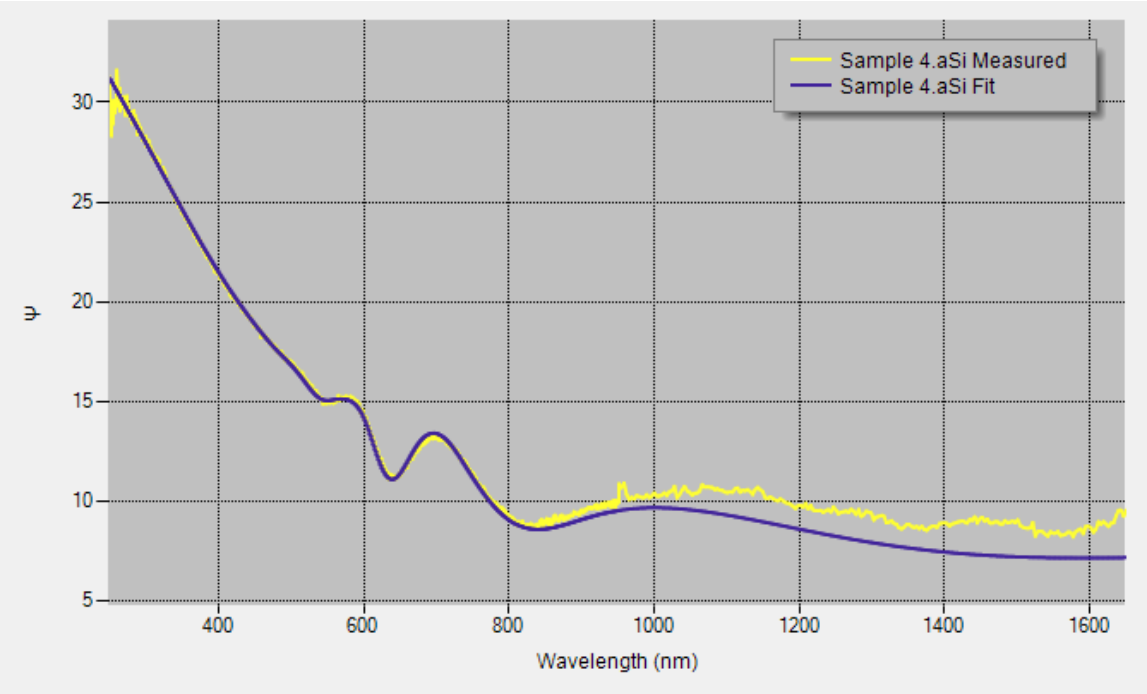

Phase difference (Δ) vs Wavelength

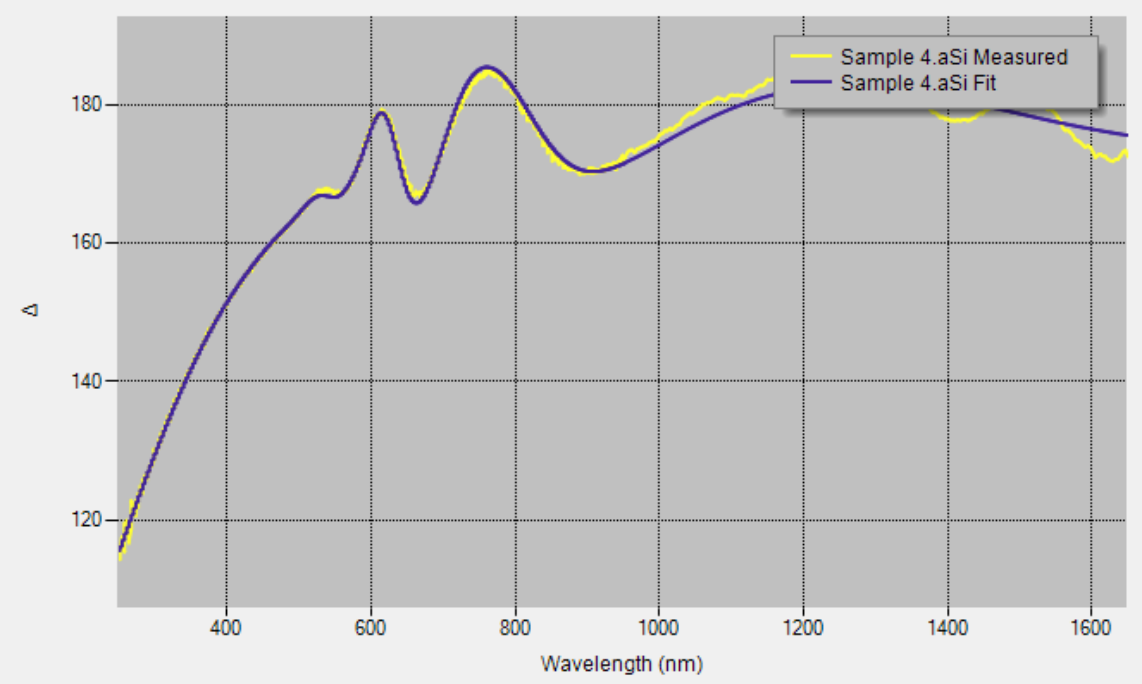

Refraction index (n) vs Wavelength

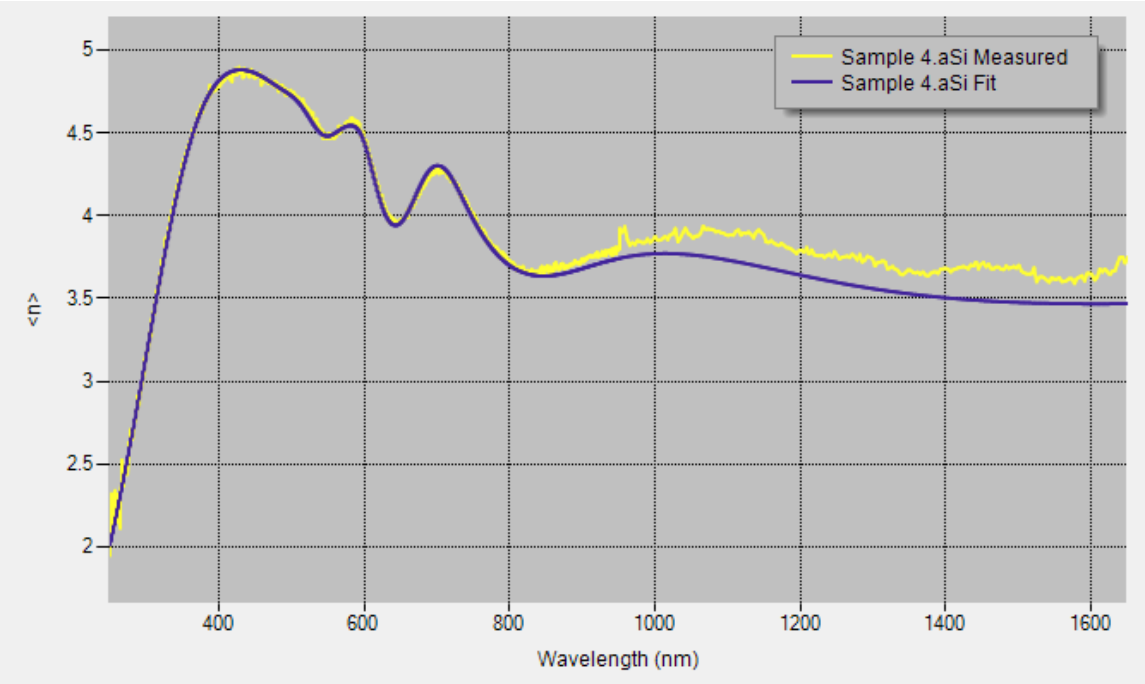

- Sample 5. a-Si:H

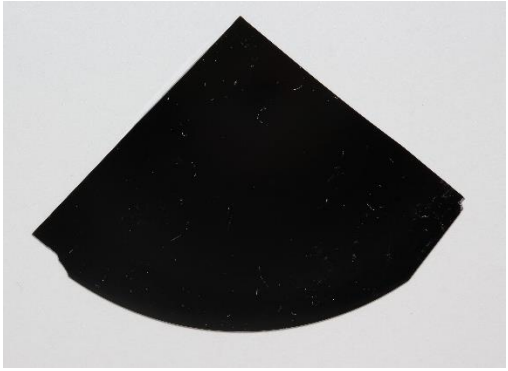

Amplitude reduction ratio (ψ) vs Wavelength

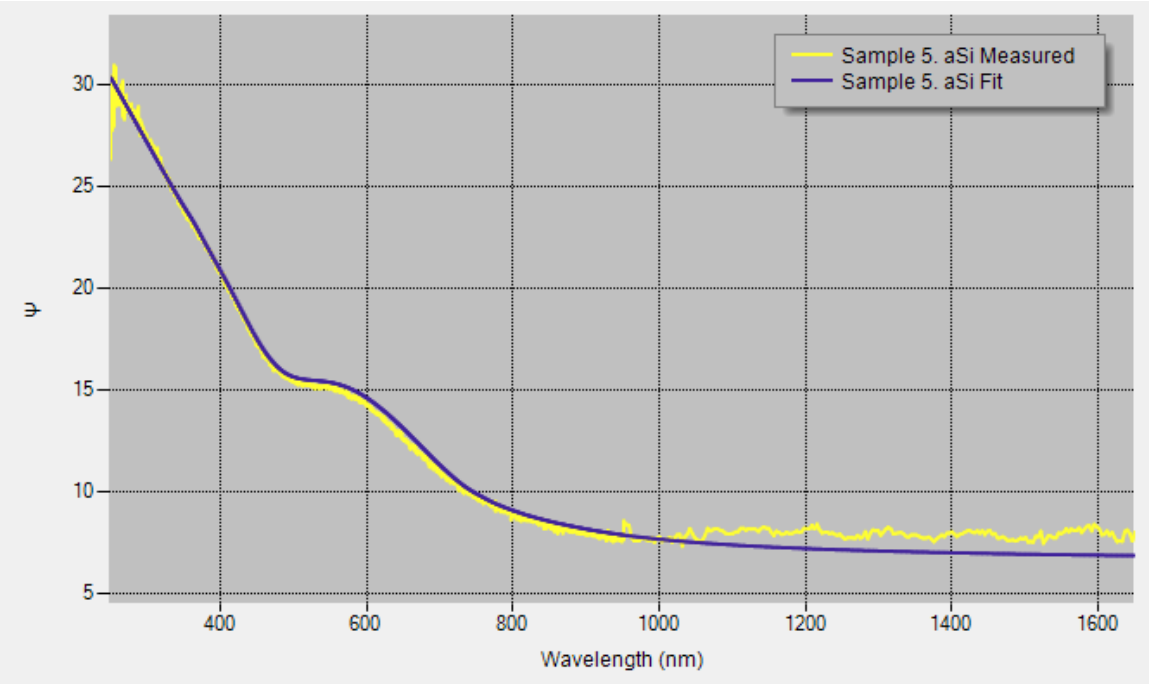

Phase difference (Δ) vs Wavelength

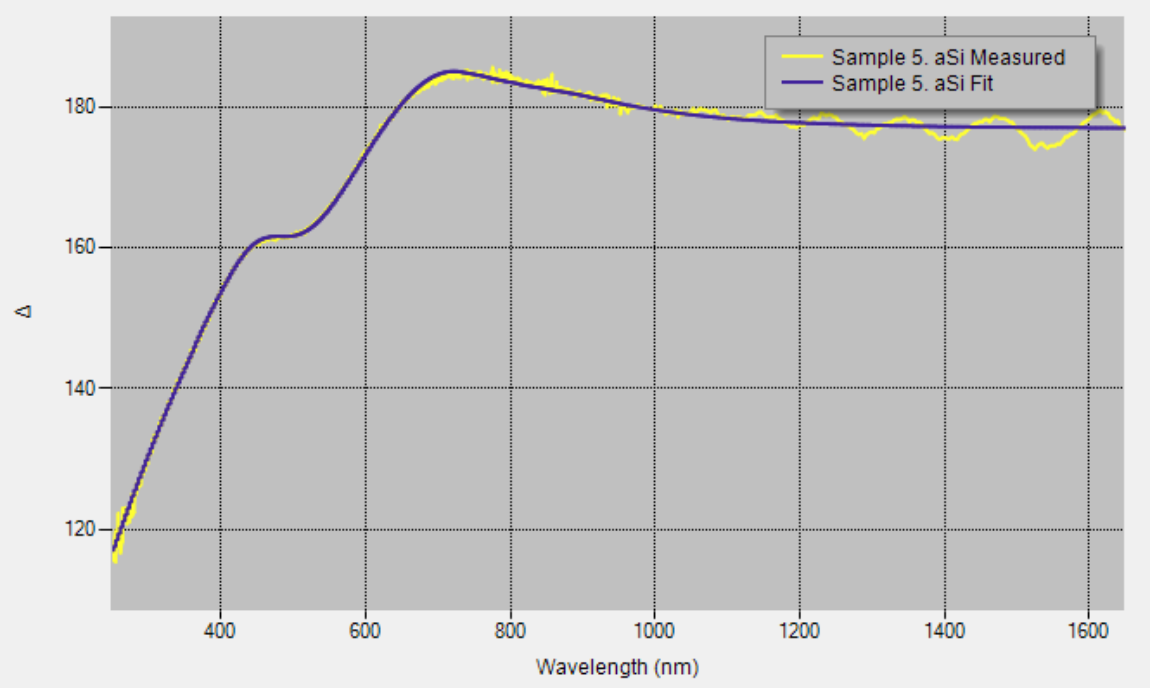

Refraction index (n) vs Wavelength

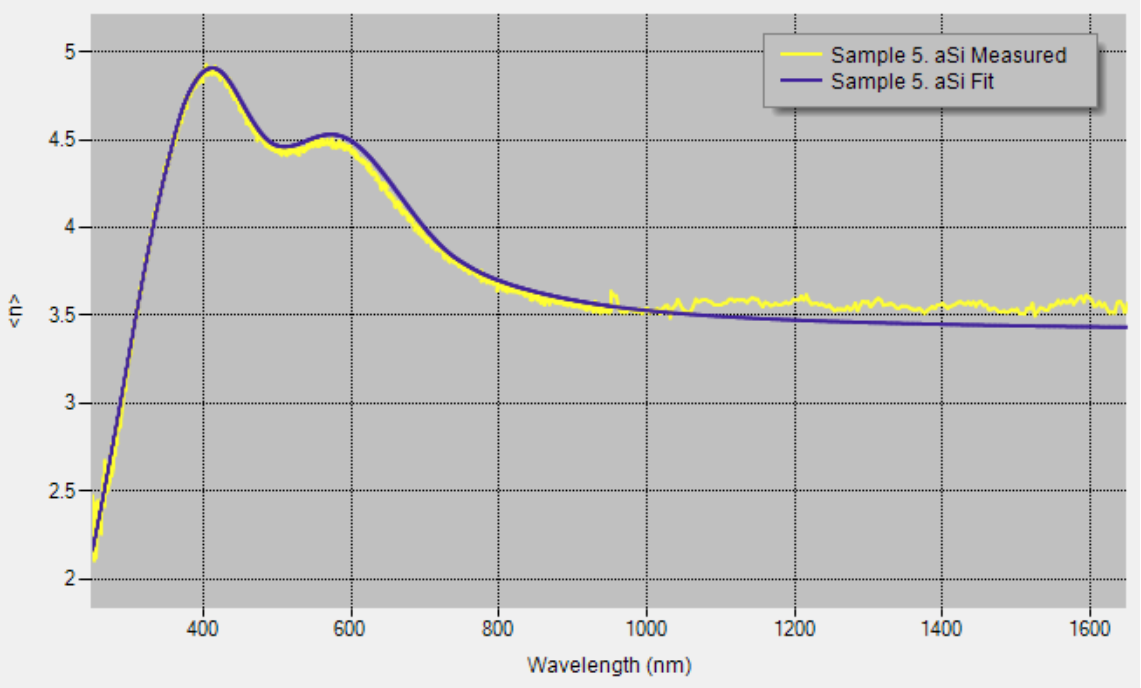

- Sample 6. a-Si:H

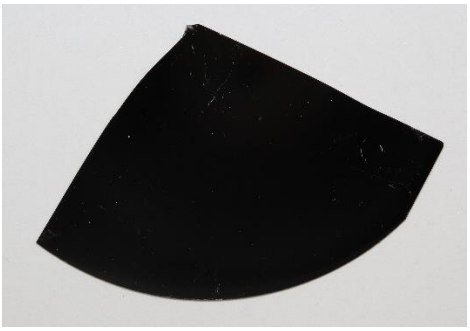

Amplitude reduction ratio (ψ) vs Wavelength

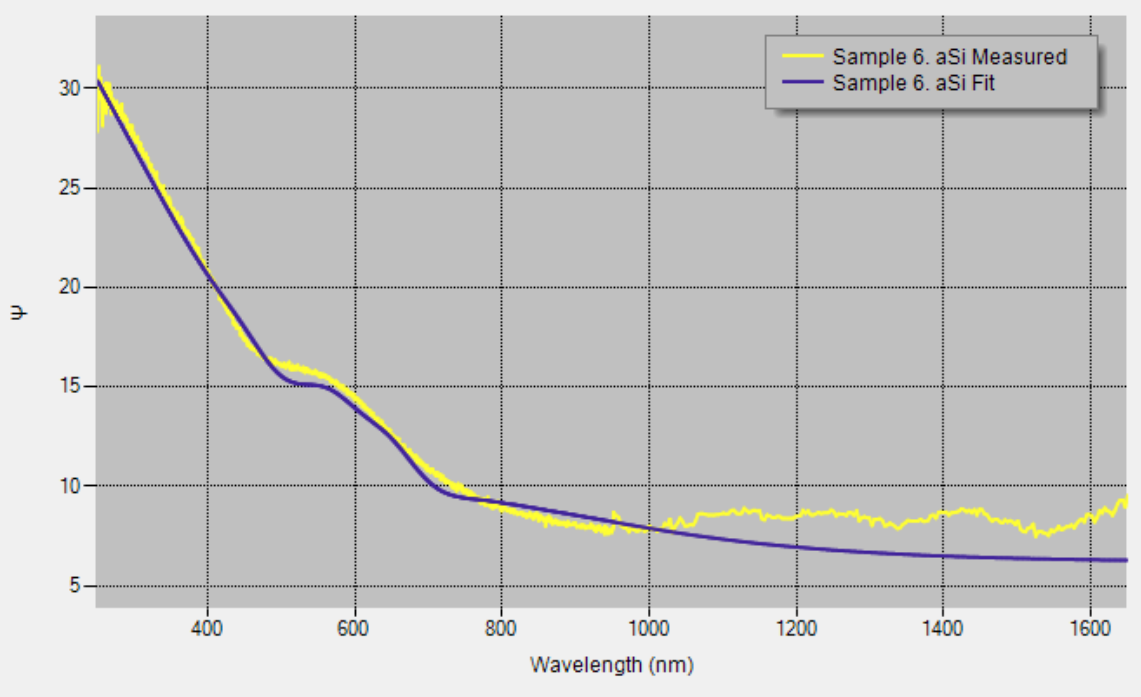

Phase difference (Δ) vs Wavelength

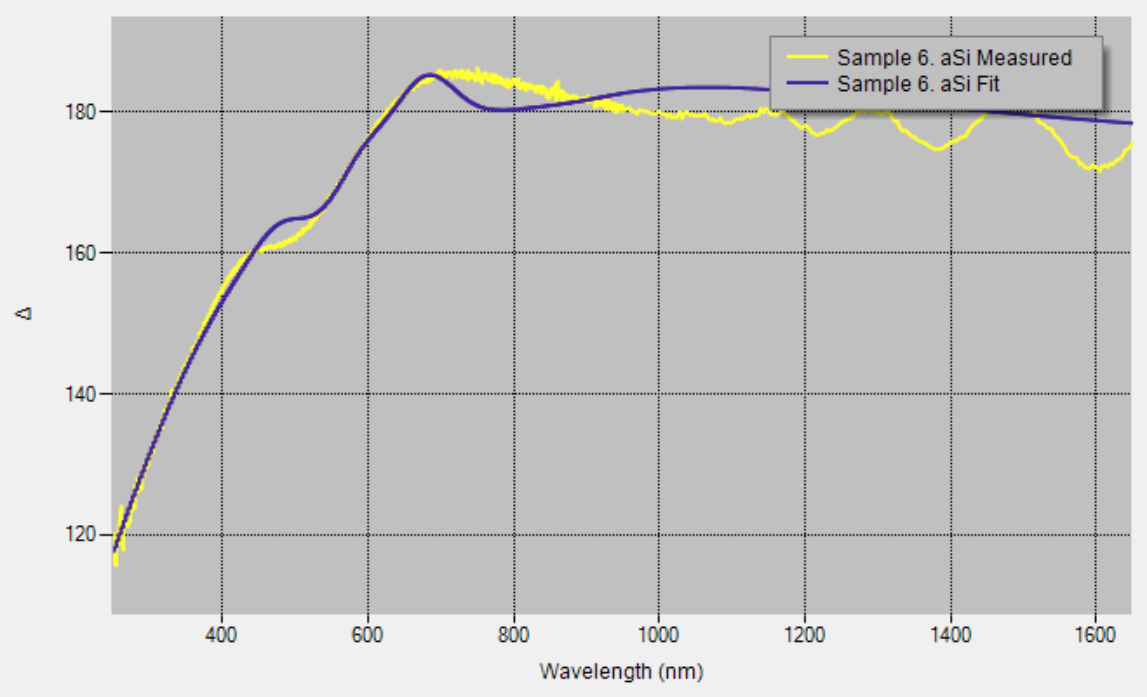

Refraction index (n) vs Wavelength

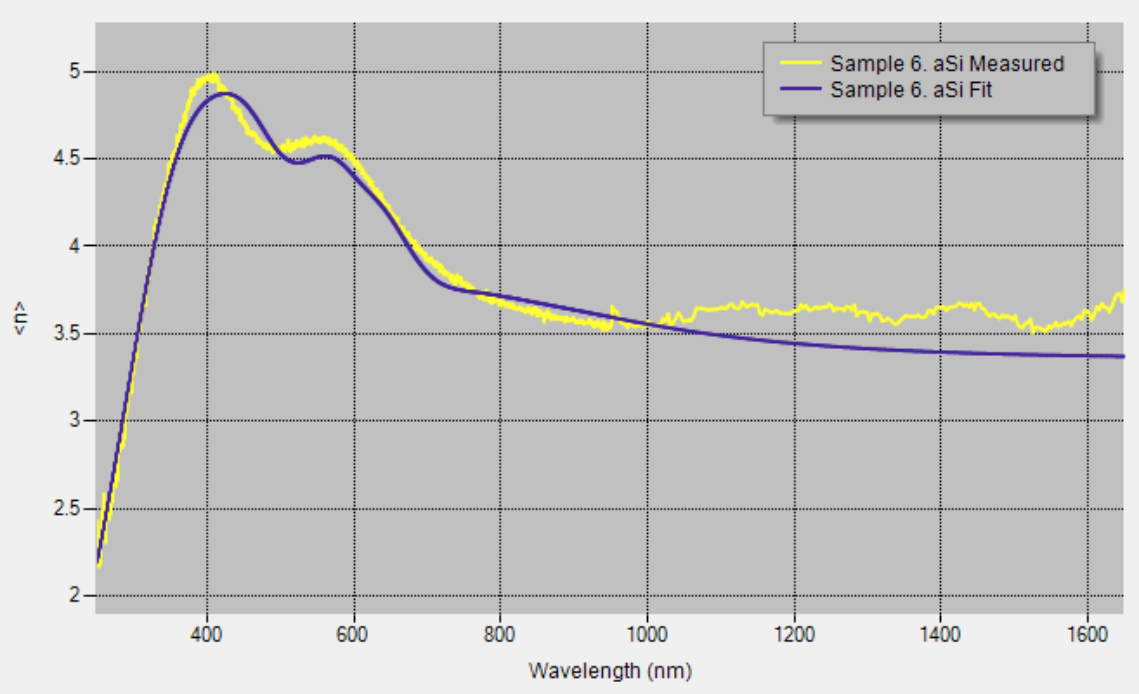

- Sample 7. a-Si:H

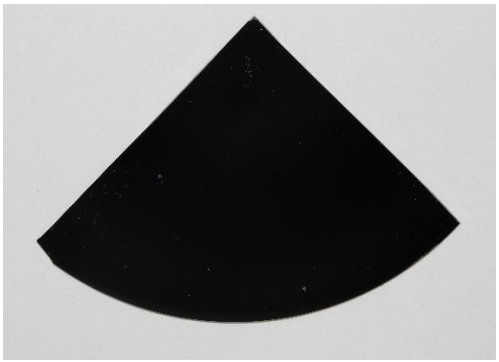

Amplitude reduction ratio (ψ) vs Wavelength

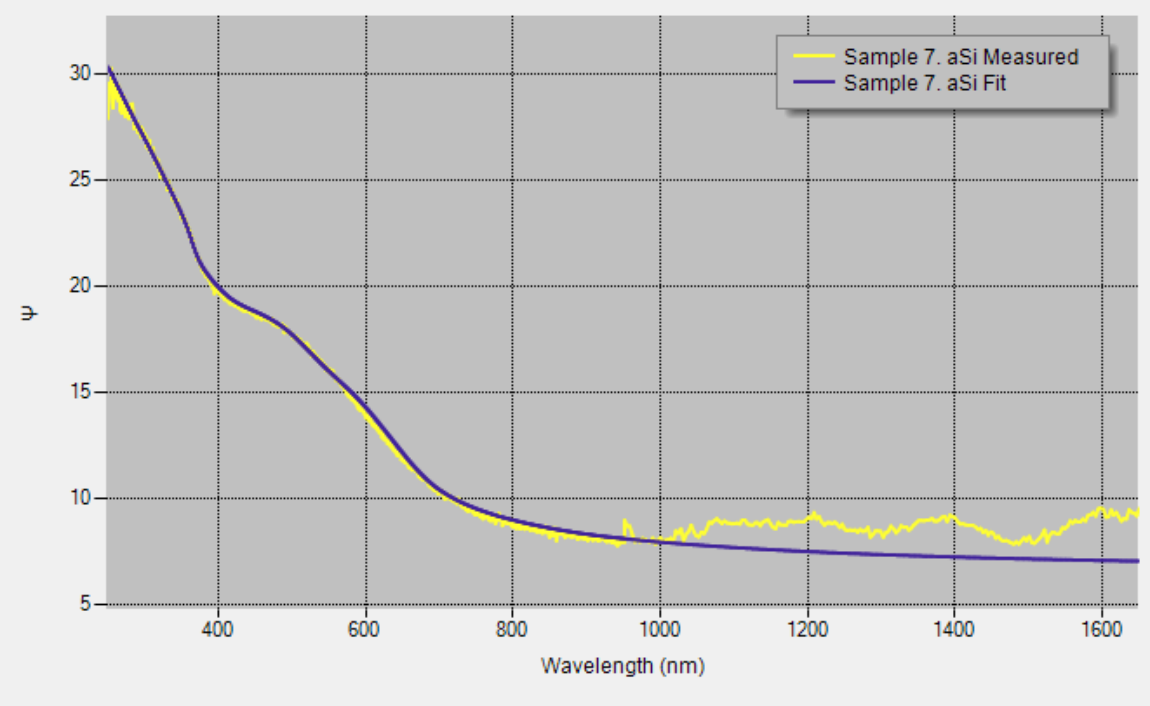

Phase difference (Δ) vs Wavelength

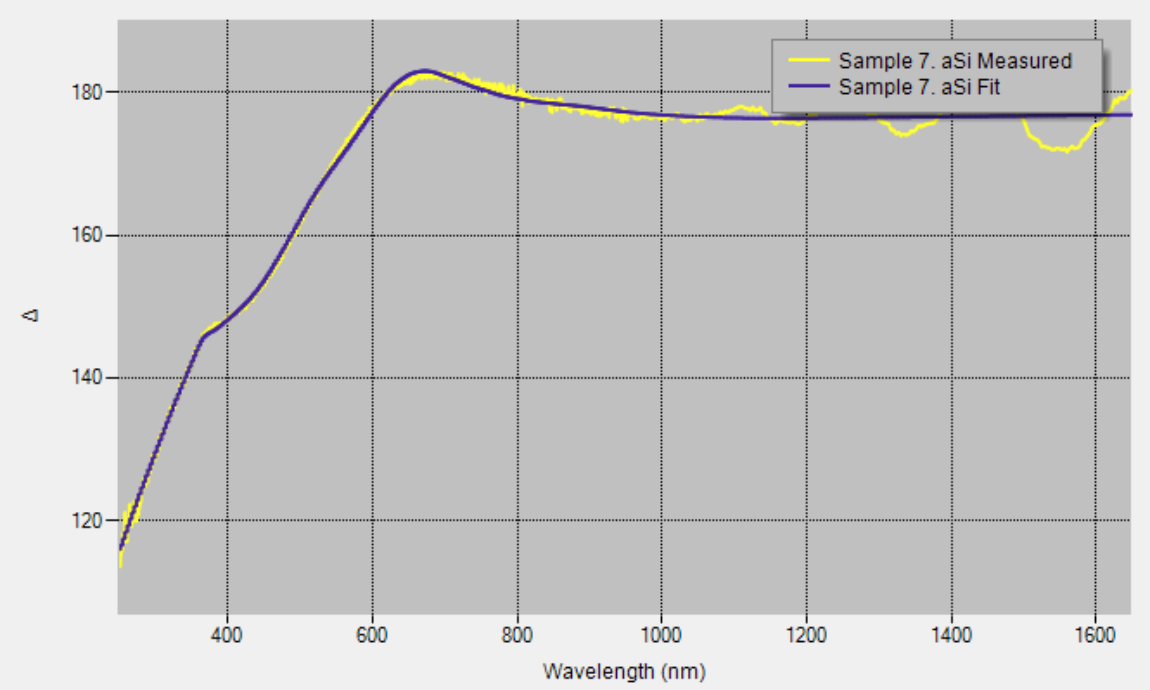
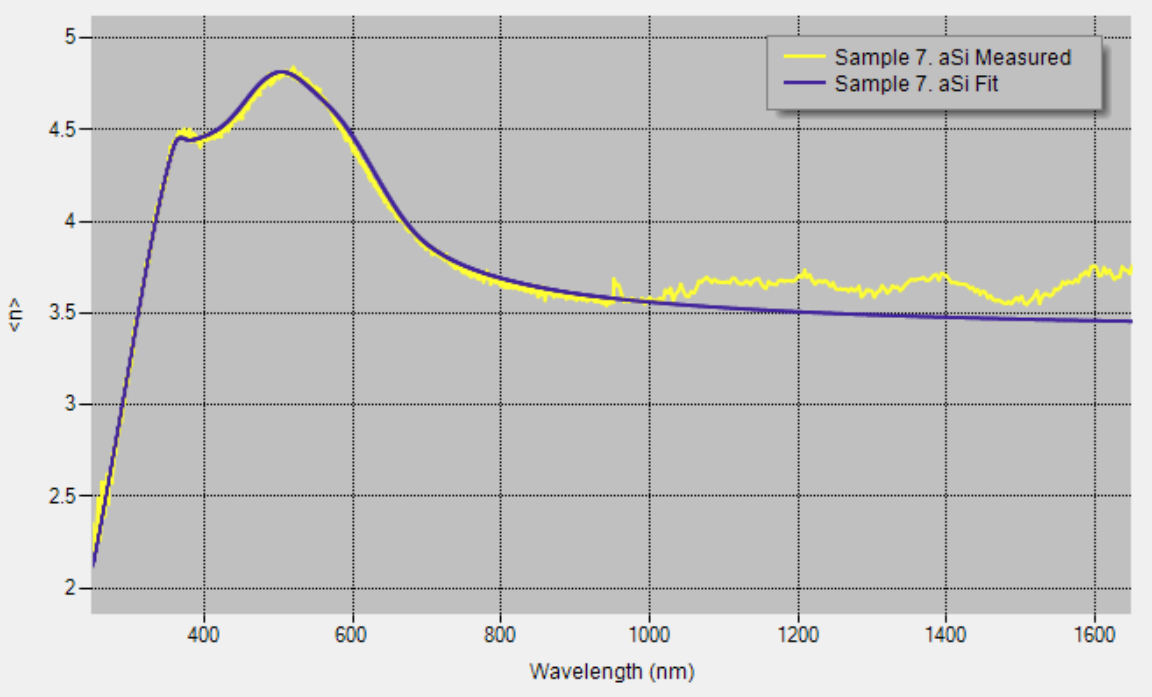
Refraction index (n) vs Wavelength